Crystallographic, Electronic, and Phononic Properties of $SrTiO_3$-$CaTiO_3$ Superlattices Versus Layer Thickness

---

A

Thesis

Presented to

the faculty of the School of Engineering and Applied Science

University of Virginia

---

in partial fulfillment

of the requirements for the degree

Doctor of Philosophy

by

Eric Robert Hoglund

December 2020

Author:
Eric R. Hoglund

Supervisor:
Professor James M. Howe

Thesis committee:
Professor Jon Ihlefeld
Professor William Soffa
Professor Petra Reinke
Professor Keivan Esfarjani
Professor Brent Fultz

Abstract

The rich phase-space of perovskite oxides offers a plethora of properties with technological importance that can be further tuned by combining multiple structures into a superlattice. This tunability has been attributed in some cases to coupling and competition of electronic and phononic structure between the layers of the superlattice. Perovskite oxide superlattices for example have exhibited thermal conductivity lower than solid solution values and exotic phases with non-transient negative capacitance. These properties suggest an evolution in the structure of the constituent layers away from their monolithic counterparts. In this thesis, it was found that crystal and electron structures in the layers of a symmetric $SrTiO_3$-$CaTiO_3$ superlattice converged from their distinct monolithic constituents to a similar and unique structure as the number of unit-cells in the layers was reduced from twenty-seven to one. The converged structure in the smaller-period superlattices displayed qualities reminiscent of the interface structure in the larger-period superlattices. It was also found that the vibrational response of the superlattices changed with the number of unit-cells in the layers, and the response was not consistent with theoretical predictions using the dipole scattering approximation and dipole-active phonon values for $SrTiO_3$, $CaTiO_3$, and $NdGaO_3$ from the literature. Therefore, the vibrational response of the superlattices was unique compared to the monolithic phases. These results demonstrate that superlattices can acquire unique structures and properties that are governed by interfaces as their sizes decrease below certain values and further, that these phenomena need to be quantified at the nanoscale to obtain a complete understanding of their behavior.

Table of Contents

Table of Figures

Table of Tables

Table of Abbreviations

ABF	Annular bright field	**NGO**	$NdGaO_3$
ADF	Annular dark field	**NR**	Non-relativistic
BF	Bright filed	**OR**	Ordered reflection
BZ	Brillouin zones	**PACBED**	Position averaged convergent-beam electron diffraction
CBED	Convergent-beam electron diffraction	**pc**	Pseudo cubic
CN	Coordination number	**Ph**	Phonon
COM	Center-of-mass	**q-EELS**	Momentum resolved electron energy loss spectroscopy
CTO	$CaTiO_3$	**q-slit**	Momentum selecting slit aperture
DCS	Differential cross-section	**SADP**	Selected area diffraction pattern
DDCS	Double differential cross-section	**SAED**	Selected area electron diffraction
DDF	Displaced dark-field	**SCTO**	$Sr_{0.5}Ca_{0.5}TiO_3$
DPC	Differential phase contrast	**SL**	Superlattice
EA	Entrance aperture	**SLR**	Superlattice reflection
EELS	Electron energy-loss spectroscopy	**SOLZ**	Second-order Laue Zone
ELNES	Energy-loss near-edge fine structure	**SPh**	Surface phonon
ELNES	Electron energy-loss near-edge fine structure	**STO**	$SrTiO_3$
ELS	Energy-loss spectrum	**SVD**	Singular value decomposition
FOLZ	First-order Laue Zone	**TE**	Transverse electric
HAADF	High-angle annular darkfield	**TM**	Transverse magnetic
HOLZ	Higher-order Laue Zone	**XANES**	X-ray absorption near-edge fine-structure
HRTEM	High-resolution TEM	**XRD**	X-ray diffraction
iCOM	Integrated center-of-mass	**ZLP**	Zero-loss peak
iDPC	Integrated differential phase contrast	**ZLP**	Zero-loss peak
IPh	Interface phonon	**ZOLZ**	Zero-order Laue Zone
NBED	Nano-beam electron diffraction		

Table of Variables

a	Lattice parameter	$\mathbf{q}_\perp$	Perpendicular momentum transfer
$\mathbf{B}$	Magnetic field	q_c	Critical momentum
b	Impact parameter	q_{EA}	Momentum selected by the entrance aperture
c	Speed of light	q_{EA}	Entrance aperture acceptance angle
C	Spring constant	$\mathbf{r}$	Position
$\mathbf{D}$	Electric displacement	r^-	Anion radius
E	Energy (loss)	$\mathbf{r}_{\vert\vert}$	Direction parallel to an interface
$\mathbf{E}$	Electric field	r^+	Cation radius
e	elementary charge	$\mathbf{r}_g$	Lattice position
E_0	Incident electron energy	$\mathbf{R}_j$	Scattering center
E_f	Final energy of incident electron	$\mathbf{r}_k$	Basis position
E_z	Electric field along z	S	Stopping power (dipole sections) Shape factor (diffraction sections
E_α	Energy of state α	S_{period,TiO_2}	Shape factor for scattering from the TiO_2 layers in superlattice period
$\mathbf{F}$	Force	S_{SL}	Shape factor for a superlattice
F	Structure factor	t	Goldschmidt tolerance factor (in bonding section) Time (in dipole and EELS sections)
F_{AO}	Structure factor for the AO sublattice in a superlattice	T	Relativistic kinetic energy
f_{begr}	Begrenzungs energy loss function	$\mathbf{u}$	Displacement
f_{bulk}	Bulk energy loss function	$\mathbf{v}$	Velocity
f_{el}	Elastic atomic form factor for electrons	$V(\mathbf{r}')$	Scattering potential
f_{in}	Inelastic atomic form factor for electrons	v_p	Phase velocity
f_{int}	Interface energy loss function	W	Work
f_j	Generalized oscillator strength	$\mathbf{w}$	Relative displacement

F_{SL}	Structure factor for a superlattice	Z	Valence number (dipole scattering sections) Atomic number (core-loss sections)
$F_{SL,i}$	Structure factor for sublattice i in a superlattice	α	Semi-convergence angle Initial electronic state (in core-loss sections) Propagation constant (in dipole sections)
$G_{\alpha\beta}$	Generalized oscillator strength	β	Relativistic velocity of an electron (in dipole sections)Final electronic state (in core-loss sections)
$\boldsymbol{H}$	Magnetic induction	Γ	Inelastic differential scattering cross-section
H	Hamiltonian (in Core-loss section)	γ	Damping constant
H'	Perturbed Hamiltonian	γ_{vac}	Lorentz contraction factor
H_0	Unperturbed Hamiltonian	ε	Permittivity
I	Intensity	ε'	Real part of the ε_r
I_{COM}	Center-of-mass intensity	ε''	Imaginary part of the ε_r
I_{DPC}	Differential phase contrast intensity	ε_0	Permittivity of free space
I_{iCOM}	Integrated center-of-mass intensity	ε_∞	High frequency permittivity
I_{iDPC}	Integrated differential phase contrast intensity	ε_r	Relative permittivity
$\boldsymbol{J}$	Current density	ε_s	Static permittivity
$\boldsymbol{k}$	Final wavevector	μ	Susceptibility
k	Final wavevector	μ_0	Susceptibility of free space
k_0	Free space wave vector	ρ	Ionic radius ratio (in bonding section) Free charge (in dipole and EELS sections)
k_c	Free space wave vector of light	σ	Scattering cross-section
M	Mass	σ_i	Inelastic scattering cross-section
m_a	Anion mass	χ	Susceptibility
m_c	Cation mass	ψ	Wave function
m_e	Electron mass	ψ_{el}	Elastically scattered wave

$N(E)$	Unoccupied density of states	ψ_H	Wave function's inhomogeneous component
n_e	Valence electron density	ψ_I	Wave function's homogeneous component
n_i	Number density of oscillator *i*	ψ_{SL}	Elastically scattered wave from a superlattice
N_i	Number of unit-cells	$\boldsymbol{\psi}_{src}(\mathbf{r}, t)$	Source function
N_{period}	Number of periods in a superlattice	ω	Frequency
$\boldsymbol{P}$	Polarization	Ω	Vibrational pole's solid angle
$\boldsymbol{p}$	Dipole moment	ω_0	Natural frequency
$\boldsymbol{q}$	Momentum (transfer)	ω_{LO}	Longitudinal optic phonon frequency
$\boldsymbol{q}_{\|\|}$	Momentum parallel to an interface	ω_p	Plasma frequency
$q_{\|\|}^{Ph}$	Bulk phonon dispersion	ω_{TO}	Transverse optic phonon frequency
$q_{\|\|}^{SPh}$	Surface (interface) phonon dispersion		

Acknowledgements

I would like to start by thanking Professor Jim Howe for being an all-around great guy and advisor. His advice has been invaluable throughout my PhD career. His flexibility has allowed me to seek after many research projects including the research in this thesis. It has also allowed for me to pursue involvements in academic societies allowing me to learn from and network with other people in my field. You have been a great mentor and have shaped who I am as a researcher.

Next, I would like to thank my PhD committee for agreeing to advise me in my dissertation research. Some of you have given me a lot of your thoughtful time and discussion.

Helge Heinrich, thank you for working on the TEM with me for the past five years. You have taught me quite a few tricks through the years and it has been lots of fun.

I have a few collaborators that I would like to thank. Jordan Hachtel was a great host at Oak Ridge National Lab where we acquired most of the EELS in this thesis. Patrick Hopkins introduced me to the superlattices in this thesis and many new material systems through side projects. R. Ramesh provided the superlattices in this research and has committed to provide future samples. Thomas Beechem at Sandia National Lab has acquired UV-Raman data (not in this thesis) and has been a great developer of this project.

My PhD was supported financially through co-advisement from Prof. Mool Gupta, Prof. Jerrold Floro, and Sean Agnew. Thank you all for both the support of my dissertation work and the research projects that you have included me in.

Lastly, I would like to thank my rather large and growing family. My parents Ken Hoglund, Dorene McCune, John McCune, and Penny Hoglund always emphasized the importance of education and pushed me (rather relentlessly) to consider an advanced education. They were correct, research is extremely rewarding and enjoyable. My wife Jordan Hoglund made the trek to Virginia with me from North Carolina. She has been supportive of my academic position and made the time in Virginia enjoyable. Life is a whole lot more fun with you around. We also now have a child Harper Hoglund who is a bubble of joy. Lastly, I would like to thank my dogs…you would be surprised how much stress is relieved at the end of the day when you come home to someone who has nothing on their mind other than wanting to play and pounce on you.

Introduction

Superlattices provide a means to create materials with tunable properties. Motivating examples include non-linear dielectric properties in $BaTiO_3$-$SrTiO_3$ superlattices (Kim et al., 2002), changes in optical activity of AlN-GaN superlattices, and thermal conductivity in symmetric $SrTiO_3$-$CaTiO_3$ superlattices (Ravichandran et al., 2014). In the latter case of $SrTiO_3$-$CaTiO_3$ symmetric superlattices, it was found that when the superlattice layer was made of 4-10 unit-cells the thermal conductivity was lower than the alloy $Sr_{0.5}Ca_{0.5}TiO_3$. With a further decrease in the number of unit-cells the thermal conductivity increased. These changes in thermal conductivity were attributed to the crossover from coherent to incoherent phonon propagation. Similarly, in AlN-GaN superlattices optical phonon modes were observed to shift with the number of unit-cells in a superlattice layer, but they also observed new phonon modes that were unique to the superlattice and not attributed to AlN or GaN. Other superlattices such as $PbTiO_3$-$SrTiO_3$ show transitions in their crystal structure and even exhibit exotic topological phases as the number of unit-cells per layer changes (Hong et al., 2017). These examples beg the question, "what happens to the structure of the constituent materials when the number of unit-cells and interfaces are similar, or when the dimensions shrink to what is effectively a single ordered phase"?

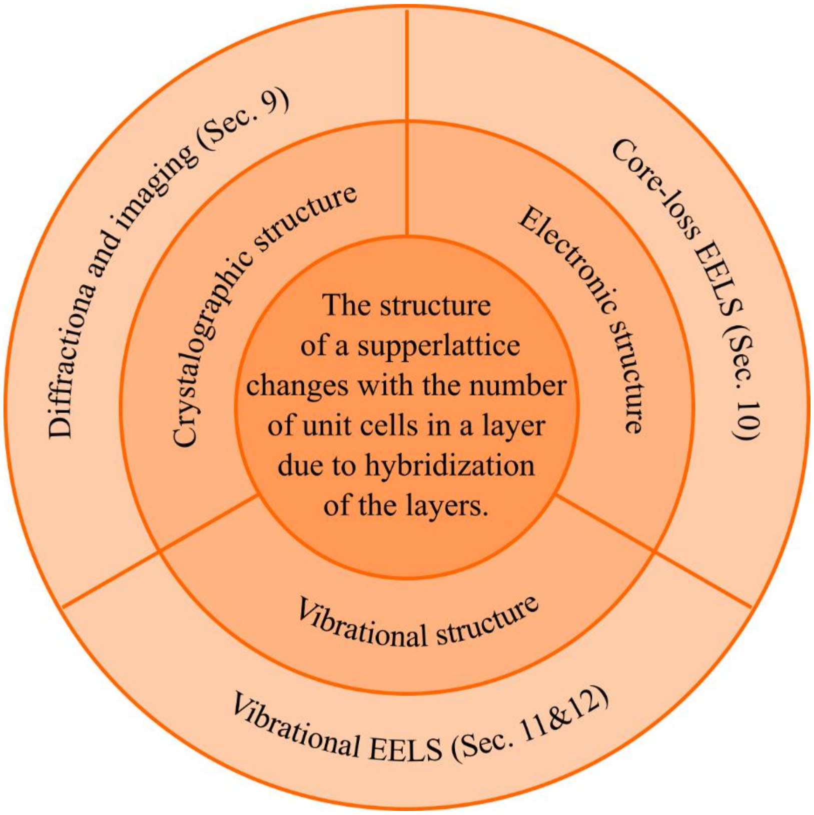

Through this thesis it will be demonstrated that the crystal, electronic, and vibrational structures of the layers comprising a $SrTiO_3$-$CaTiO_3$ symmetric superlattice evolve to similar structures as the number of unit-cells in a layer decrease. The converged structure in the smaller-period superlattices displayed qualities reminiscent of the interface structure in the large-period superlattice. In the one unit-cell limit, an entirely new structure consisting of anti-parallel cation displacements and a long-range modulation in magnitude of the anti-parallel displacements emerges. This thesis proceeds by first introducing relevant background related to perovskites (Section 1) and phonons (Section 2) followed by experimental and theoretical background about diffraction (Section 3), imaging in a scanning transmission electron microscope (Section 4) inelastic scattering (Section 5), and an electron acting as an electromagnetic wave (Section 6). Section 7 describes the samples provided by Prof. R. Ramesh from the University of California, Berkeley. The remaining Sections are resultant of this dissertation work, which begins in Section 8 with a derivation of diffraction from a superlattice that contains a continuous backbone throughout the entirety of the superlattice, such as the TiO_6 octahedra in the $SrTiO_3$-$CaTiO_3$ superlattice examined here. This aids in the interpretation of diffraction data acquired from the superlattices presented in Section 9. Section 9 demonstrates the evolution in crystal structure and lattice orientation as the number of unit-cells in a layer decrease. From a large period (27 unit-cell per layer) to a smaller period (<4 unit-cell per layer) it was observed that the crystal transitions from the distinct monolithic phases to similar phases resembling the interface structure of larger period superlattices. Section 10 then shows using core-loss electron energy-loss spectroscopy, that the convergence in crystal structure is also present in the electron structure. The remaining sections deal with the vibrational spectra of the superlattices. Section 11 presents simulations of expected vibrational spectra using data for the monolithic phases. Section 12 then presents vibrational electron energy-loss spectra that do not resemble the theoretical predictions of Section 11, but do show variation in the vibrational response of Ti- and O-sublattices as the number of unit-cells in a layer is varied. Lastly, the main findings of this thesis are summarized in the conclusions section.

1 Perovskite Oxides

The rich phase space of perovskite oxides serves as the genesis for their robust and varied technological importance. The displacive phase transformations that create the rich phase-space are a result of changes in bonding and phonon character. In this Section the general structure, bonding, and phonon character of perovskite oxides are discussed. Subsequent subsections further discuss bonding, TiO_6 octahedral tilting, the specific phases of $SrTiO_3$ (STO), $CaTiO_3$ (CTO), and $Sr_{0.5}Ca_{0.5}TiO_3$ (SCTO), and a background on perovskite oxide superlattices (SL).

Perovskite oxides are a class of materials containing A- and B-cation sublattices and an O-anion sublattice. The idealized perovskite oxide is simple cubic with a basis of corner sharing A atoms, three face centered O atoms, and body centered B atoms. When the ionic radius of the A and O atoms are similar, they form a face centered cubic arrangement with the Ti atom occupying the octahedral interstitial site.

The site occupancies relate to the predominantly ionic bonding that occurs in this class of materials. The ionic bonding phenomenologically can also describe structural distortions that occur in perovskites leading to phases of lower symmetry. The ionic nature of cation-anion bonding does not however describe all physical distortions that occur, and the mixed covalent-ionic nature of the bonds need be considered. The relation between bonding and the structure of perovskite oxides will be the topic of Section 1.1. The bonding discussed in Section 1.1 can be probed using energy-loss spectroscopy (EELS) by characterizing the energy-loss near-edge fine structure (ELNES). Background on O-K and Ti-$L_{2,3}$ near-edge fine structures, which are pertinent to this investigation, will also be introduced to prepare the reader for the variations observed in ELNES of STO-CTO SLs presented in Section 10.

Phase transformations in perovskites are often induced by softening of either, or both, ferrodistortive and anti-ferrodistortive phonon modes (i.e., vibrations that rotate BO_6 octahedra) and ferroelectric phonon modes (i.e., phonons inducing relative displacements of cations within the lattice). For example, the large dielectric constant of tetragonal $BaTiO_3$ derives from Ti displacements that form due to phonon softening at the Γ-point (Aikawa & Fujii, 2011). Similar phase transformations separate the superconducting behavior of $YBa_2Cu_3O_{7-\delta}$, and insulating STO (Bhalla et al., 2000). Control of phases and phase transformations in oxide perovskites is therefore critical to this material class. The phonon modes associated with octahedral rotations that are observed in STO and CTO will be discussed further in Section 1.2.

Additional phases, and hence functionality, can emerge when two different perovskites are coupled in a superlattice or cation ordering occur (Ramesh & Schlom, 2019; Rondinelli & Fennie, 2012). The additional phases emerge owing to the local minima that form across the energy landscape as differing phonon modes competitively soften. At the limit of a superlattice composed of alternating materials consisting of a single unit-cell, these effects may even magnify and open the possibility for the observation of exotic perovskite phases and emergent phenomena. The existence of nanometer length-scale lattices that can emerge then provide for unique properties. For example, emergence of microscopic skyrmion lattices in $PbTiO_3$-STO superlattices manifest unique (and tunable) dielectric, piezoelectric, and optical properties (Das et al., 2019; J. Park et al., 2020; Ajay K. Yadav et al., 2019). Similarly, characteristic electronic properties emerge in twisted bi-layer 2D materials as a result of Moire fringes (Chatterjee et al., 2020; Ohta et al., 2012; Robinson et al., 2013; Yankowitz et al., 2012). The creation of artificial superlattices therefore provides an architecture to control macroscopic responses of a material. Naturally ordering and synthetic perovskite oxide superlattices will be discussed further in Section 1.3.

In the following Section and subsections, relevant background for bonding and octahedral rotation in perovskite oxides is introduced. Background for STO, CTO, and SCTO is then presented, since STO and CTO are the endmembers comprising the SL and SCTO has the same macroscopic concentration as the symmetric superlattices. The relation between phonon modes, cation displacements, and octahedral rotations will be connected throughout these discussions. An introduction to Glazer's notation will be introduced when discussing octahedral rotations, which allows for the relation of lower symmetry structures to the idealized high symmetry $Pm\bar{3}m$ perovskite structure. These topics lay the foundation for the understanding of phase transformations in perovskite oxides, how to experimentally characterize the transformations in a transmission electron microscope (TEM), and what phases might be expected *a priori*.

1.1 Bonding in Perovskite Oxides

Bonding in perovskites plays a key role in their structural stability and the diversity in constituting elements and phase space. In this section the bonding in perovskite oxides is described in the context of structural stability, phase transformations, and electronic structure. These are important concepts for later analysis of the structure and bonding in STO-CTO superlattices using diffraction, imagining, and ELNES.

The energy of a perovskite oxide is predominantly described by the Coulombic interaction between anions and cations, which is embodied in the Madelung constant. Therefore, the coordination number (CN) of ions can be determined by the ionic radius ratio (ρ=r$^+$/r$^-$, with $r^{\pm}$ as the ion radius) rules proposed by Pauling in 1929 (Pauling, 1929). The ion ratio rules are outlined in Table 1.1 and the ratios relevant to STO and CTO are provided in
Table 1.2.

Table 1.1. Pauling's radius ratio rules.

ρ=r$^+$/r$^-$	**CN**	**Type**
ρ<0.155	2	Linear
0.155<ρ<0.225	3	Triangular
0.225<ρ<0.414	4	Tetrahedral
0.414<ρ<0.732	6	Octahedral
0.732<ρ<1.000	8	Cubic
ρ=1	12	Close packed

Table 1.2. Ionic radii for elements in STO and CTO, pertinent ionic ratios, and predicted Pauling coordination numbers.

$\boldsymbol{I}$	$\boldsymbol{r_i^{\pm}}$	$\boldsymbol{r_i^{+}/r_O^{-}}$	**Pauling CN**	**Actual CN**
Sr	132	1.048	12	12
Ca	114	0.905	8	8
Ti	74.5	0.591	6	6
O	126	-	-	

Pauling's ionic ratio rules predicts a coordinated number of six for Ti atoms in STO and CTO. This is in fact the correct coordination and predicts the formation of undistorted TiO_6 octahedra. The coordination of A-sites is predicted as 8 and 12 for CTO and STO, respectively. At room temperature and pressure, STO adheres to the idealized simple cubic lattice and the Sr atom has a CN of 12. CTO on the other hand has a coordination of 8 because of systematic rotation of TiO_6 octahedra (Buttner & Maslen, 1992; Knight, 2011; Koopmans et al., 1983). The predictions from Pauling's ionic ratio rules are therefore accurate in predicting the local coordination of the cations in perovskite oxides.

A similar rule was proposed by Goldschmidt to predict the structure of perovskite oxides. A tolerance factor (t) is defined as the ratio of ideal A-O and B-O bond length, like Pauling's ionic radius ratio, where

$$t = \frac{r_A + r_O}{\sqrt{2}(r_B + r_O)}$$

The structural predictions related to the tolerance factor are shown in Table 1.3. The prediction of the Goldschmidt tolerance factor correctly predicts the crystal structure for both CTO and STO.

Table 1.3. Goldschmidt tolerance factor ranges for predicted structures, and examples.

t	**Structure**	**Examples**
>1	Hexagonal or Tetragonal	$BaTiO_3$ (t=1.062)
0.9<t<1	Cubic	$SrTiO_3$ (t=0.910)
0.71<t<0.9	Orthorhombic or Rhombohedral	$CaTiO_3$ (t=0.846)
t<0.71	Others	$FeTiO_3$ (t=0.666)

Distortions of the TiO_6 octahedra and displaced Ti atoms leads to different A-site and Ti-site coordination with changing temperature. These displacements and rotations are tied to the bonding in the material and result in softened phonon modes, which will be discussed in Section 1.2. The specific transformations for STO, CTO, and SCTO are discussed in Section 1.4. Although bonding in ABO_3 oxides can be described using ionic bonding, this is a rather naive approach and neglects the appreciable covalent nature of bonding between cations and anions (Carl W., 1963). Increased Ti-O covalency for example partly explains the displacement of Ti atoms in $BaTiO_3$ (Carl W., 1963; Megaw, 1952).

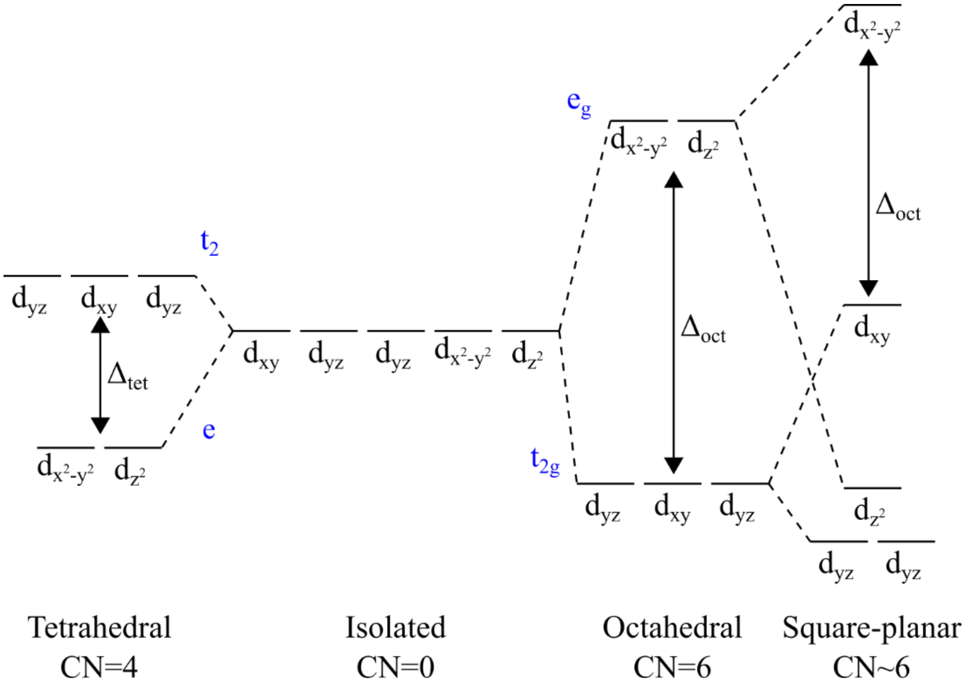

Figure 1.1. Crystal field splitting of *d*-orbitals because of local coordination number (CN) and symmetry.

The electron orbitals of atoms split because of the local environment, coordination, and symmetry, as shown in Figure 1.1 for common site symmetries. In molecular orbital theory the splitting is known as crystal field splitting. For example, when an atom is in octahedral site its *d*-orbitals split into a higher energy e_g band with four states and a lower energy t_{2g} band with six states. This is a result of the symmetry and directionality of the bonds with the higher energy band having bonds directed at corners of the octahedra. The splitting of the bands is associated with an energy, Δ_{oct}. If the octahedra is tetragonally distorted, then e_g $d_{x^2-y^2}$ and d_{z^2} no longer have equal bond lengths and are no longer degenerate. Likewise, the d_{xy} orbitals are no longer degenerate with d_{xz} and d_{yz}. This splitting occurs for the *d*-orbitals in the B-site of perovskites (Carl W., 1963). Splitting also occurs in the *s*- and *p*-orbitals of oxygen and is tied to local Sr-O and Ti-O bonding and symmetry. In perovskite oxides it is expected that the bonding is different within the different phases. As previously mentioned, the Ti atoms are in an octahedral site for both CTO and STO, therefore it is expected that the crystal field effects and splitting of Ti *d*-orbitals is identical. The oxygen environment is however different in STO and CTO, so the crystal filed splitting is expected to be different for oxygen. The manifestation of these bonding differences in ELNES is discussed in Section 5.1.

In this subsection, the bonding in perovskite oxides was discussed. The site-specific stability of constituent ions and their effect on electronic structure were established. ELNES and the crystallographic-electronic structure relations here will be useful in the analysis of ELNES spectra of STO-CTO superlattices in Section 10.

1.2 Octahedral Tilting in Perovskites

In perovskites systematic displacement of atoms results in phase transformations, which can be described by distortions of the idealized high-symmetry structure. The displacements are a result of altered bonding (as described in Section 1.1) and unstable phonons (known as soft phonons). In this Section, displacements that occur in perovskites, their relation to phonons, and how to characterize them in a (S)TEM are discussed.

The lower-symmetry lattice of a distorted perovskite is conventionally projected to the idealized high-symmetry (*aristotype*) $Pm\bar{3}m$ space group, easing visualization and description of different phases. The projection onto the *aristotype* lattice is also often referred to as the pseudo-cubic (pc) unit-cell, since the *aristotype* for perovskites is a simple cubic lattice. The simplification and back projection of crystals with lower symmetry also allows for systematic phase identification of space group by indexing ordered reflections (ORs) in diffraction data (Glazer, 1972, 1975; David I. Woodward & Reaney, 2005; P. M. Woodward, 1997a, 1997b).

In 1972 Glazer proposed a system for classifying the rigid rotation of TiO_6 octahedral about the three pc axes (i.e. $\langle 100 \rangle_{pc}$ directions), and this notation has been adopted by the field (Glazer, 1972, 1975). The relative magnitude of the tilt angle about one of the pc axes is indicated by the letters *a*, *b*, and/or *c*. For examples, the sequence *aaa* indicates equivalent tilt angles about all three pc axes, the sequence *aac* indicates equivalent tilt angles around the $[100]_{pc}$ and $[010]_{pc}$ axes, and the sequence *abc* indicates different tilt angle about all three pc axes. Superscripts are used to describe the sense of TiO_6 octahedra tilting along the axis relative to its neighbors. The superscript 0, –, and + represent no tilting, out-of-phase tilting, and in-phase tilting. For example, $a^0a^0c^-$ has two axes without tilt (as shown in Figure 1.2d) and one with out-of-phase tilting (as shown in Figure 1.2e). Another example, $a^-a^-c^+$, has two out-of-phase tilts with equal magnitude (as shown in Figure 1.2g) and one in-phase tilt (as shown in Figure 1.2h). In-phase and out-of-phase octahedral tilts are a result of softened antiferrodistortive phonon modes at wavevector $\boldsymbol{q} = \left(\frac{1}{2}\frac{1}{2}0\right)$ (M_3^+) and $\boldsymbol{q} = \left(\frac{1}{2}\frac{1}{2}\frac{1}{2}\right)$ $(R_4^+$ or $R_{25})$ brillouin zones (BZ), respectively[1] (Campbell et al., 2006; Glazer, 1975; Howard & Stokes, 1998). A third softening mode responsible for antiparallel cation displacements occurs at $\boldsymbol{q} = \left(\frac{1}{2}00\right)$ (X_5^+). When a combination of in- and out-of-phase tilts are present, A-site cations are displaced. The

---

[1] R_4^+ is appropriate when the origin is an A-site whereas R_{25} is chosen when the center of the TiO_6 octahedra is the origin.

displacement of cations from octahedral displacements is known as improper ferroelectricity. This is observed in the $a^-a^-c^+$ tilt system (for which CTO is a part of), as shown in Figure 1.2h.

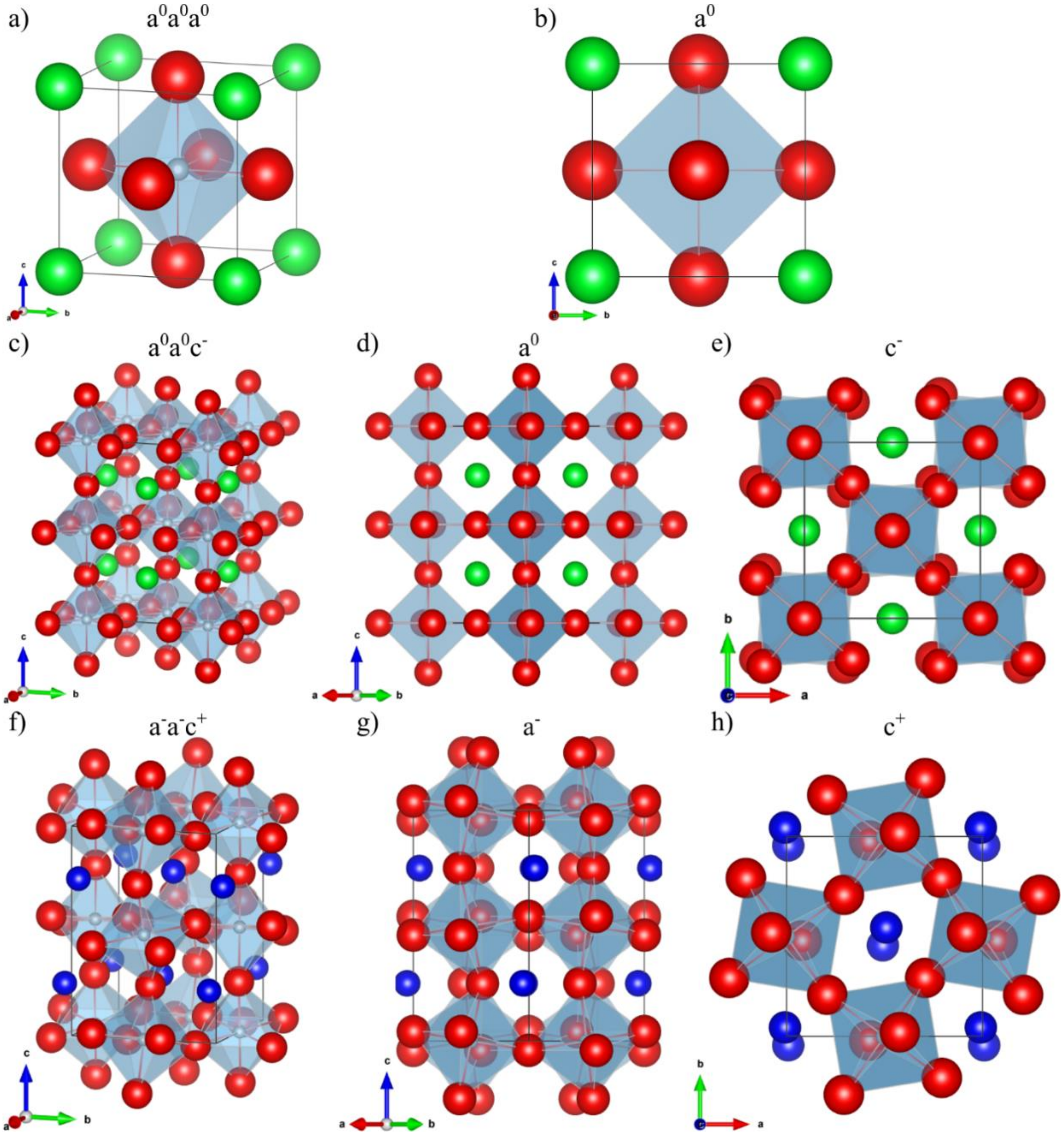

Figure 1.2. Model perovskite structures for $Pm\bar{3}m$ (a-b), I4/mcm (c-e), and Pbnm (f-h) space groups. The tilt pattern for each space group are listed in (a), (c), and (f). (d) and (g) are viewed along $[100]_{pc}$ showing the a^0 and a^- tilts present in I4/mcm and Pbnm space groups, respectively. (e) and (h) are viewed along $[001]_{pc}$ showing the c^- and c^+ tilts present in I4/mcm and Pbnm space groups, respectively. Cation displacements are observed in (h), which result from the mixed tilt pattern $a^-a^-c^+$ in Pbnm. The three phases presented were chosen because they illustrate the various octahedral rotations discussed and because $Pm\bar{3}m$ and I4/mcm are the stable phases of STO, and $Pm\bar{3}m$, I4/mcm, and Pbnm are the stable phases of CTO. The red, gray, and green (or blue) atoms represent O, Ti, and A sites, respectively.

From the combination of *a*, *b*, *c*, 0, +, and –, Glazer identified 23 unique tilt systems and associated each with a space group (Glazer, 1972, 1975; P. M. Woodward, 1997a), as shown in

Table 1.4. Multiple pc unit-cells are required to capture the tilt patterns, most of which are double perovskites (i.e. 2x2x2). Interestingly, all tilt systems that contain two out-of-phase tilt axes with identical magnitude have unit-cells that are rotated 45° with respect to the pc axes. This is because two out-of-phase tilts can be described as a single out-of-phase tilt along a $\langle 110 \rangle_{pc}$ axis. Within the 23 tilt systems, 16 unique space groups are present. Howard and Stokes corrected the 16 unique space groups to 18 and using group-theoretical methods further reduced the number of allowed tilt systems from 18 to 15 (Howard & Stokes, 1998). They also noted that a geometrical distortion of the TiO_6 was required for tilt systems 4-7.

Table 1.4. 23 Glazer tilt systems proposed by Glazer (Glazer, 1972) and corrected by Woodward (P. M. Woodward, 1997a).

#	**Tilt system**	**Relative to pc dimensions**	**Relative pc parameters**	**Space group**
Three-tilt systems				
1	$a^+b^+c^+$	$2 \times 2 \times 2$	$a \neq b \neq c$	Immm (No. 71)
2	$a^+b^+b^+$		$a \neq b = c$	Immm (No. 71)
3	$a^+a^+a^+$		$a = b = c$	Im$\bar{3}$ (No. 204)
4	$a^+b^+c^-$		$a \neq b \neq c$	Pmmn (No 59-2)
5	$a^+a^+c^-$		$a = b \neq c$	P4$_2$/nmc (No. 137-2)
6	$a^+b^+b^-$		$a \neq b = c$	Pmmn (No 59-2)
7	$a^+a^+a^-$		$a = b = c$	P4$_2$/nmc (No. 137-2)
8	$a^+b^-c^-$		$a \neq b \neq c, \alpha \neq 90^o$	P2$_1$/m (No. 11-2)
9	$a^+a^-c^-$		$a = b \neq c, \alpha \neq 90^o$	P2$_1$/m (No. 11-2)
10	$a^+b^-b^-$	$2 \times \sqrt{2} \times \sqrt{2}$	$a \neq b \neq c,$	Pnma (No. 62)
11	$a^+a^-a^-$		$a \neq b \neq c,$	Pnma (No. 62)
12	$a^-b^-c^-$	$2 \times 2 \times 2$	$a \neq b \neq c, \alpha \neq \beta \neq \gamma \neq 90^o$	F1 (No. 2)
13	$a^-b^-b^-$	$2 \times \sqrt{2} \times \sqrt{2}$	$a \neq b \neq c, \alpha \neq \beta \neq \gamma \neq 90^o$	I2/a (No. 15-3)
14	$a^-a^-a^-$	$2 \times 2 \times 2$	$a = b = c, \alpha = \beta = \gamma \neq 90^o$	R3c (No. 167-2)
Two-tilt systems				
15	$a^0b^+c^+$	$2 \times 2 \times 2$	$a < b \neq c$	Immm (No. 71)
16	$a^0b^+b^+$		$a < b = c$	I4/mmm (No. 139)
17	$a^0b^+c^-$		$a < b \neq c$	Cmcm (No. 63)
18	$a^0b^+b^-$		$a < b = c$	Cmcm (No. 63)
19	$a^0b^-c^-$		$a < b \neq c, \alpha \neq 90^o$	I2/m (No. 12-3)
20	$a^0b^-b^-$	$2 \times \sqrt{2} \times \sqrt{2}$	$a < b = c, \alpha \neq 90^o$	Imma (No. 74)
One-tilt systems				
21	$a^0a^0c^+$	$2 \times 2 \times 2$	$a = b < c$	P4/mbm (No. 127)
22	$a^0a^0c^-$		$a = b < c$	I4/mcm (No. 140)
Zero-tilt systems				
23	$a^0a^0a^0$	$1 \times 1 \times 1$	$a = b = c$	Pm$\bar{3}$m (No. 221)

Diffraction techniques can characterize the space group of a perovskite. As phonon modes soften, and new BZs are formed, ORs appear in the diffraction patterns. In general diffraction techniques, x-rays are less sensitive to distortions in the oxygen sublattice, making electron and neutron diffraction preferable. In 1975 Glazer outlined the condition for ORs based on the in-phase and out-of-phase tilts. This was then reviewed by Woodward and Reaney and included multiple examples of space group determination using selected area electron diffraction (SAED) (David I. Woodward & Reaney, 2005). The complete set of rules are listed in Table 1.5, but in general in-phase tilts create ORs appearing at ½(ooe), out-of-phase tilts create ½(ooo) ORs, where "o" and "e" represent odd and even miller indices. The displacements of cations from the combination of in-phase and out-of-phase tilts create ½(eeo) ORs and are named concert reflections. Woodward and Reaney also tabulated the reflections present in pc and non-pc zone axes, for non-distorted tilt system with unequal + and – tilts, using the conditions listed in Table 1.5, this is reproduced in Table 1.6 for completeness.

Table 1.5. Rules for allowed and absent ORs that result from octahedral tilting.

Allowed reflections produced from in- and out-of-phase tilts		
1	a^-	½(ooo)$_{h\neq k}$
2	b^-	½(ooo)$_{h\neq l}$
3	c^-	½(ooo)$_{k\neq l}$
4	a^+	½(eoo)$_{h\neq k}$
5	b^+	½(oeo)$_{h\neq l}$
6	c^+	½(oeo)$_{k\neq l}$
Allowed concert reflections		
7	a^+	½(oee) no ½(h00)
8	b^+	½(eoe) no ½(0k0)
9	c^+	½(eeo) no ½(00l)
10	Two in-phase tilts	All 7-9
11	a^+	½(eoo)
12	b^+	½(oeo)
13	c^+	½(oeo)
14	Two in-phase tilts	All 11-13
Absences in concert reflections viewed parallel to an out-of-phase tilt axis		
15	$a^0b^-c^+$	$k\neq 0$
16	$a^-a^-c^+$	$h-k\neq 0$ or $h+k\neq 0$ (depending on the sense of a^- tilts)
17	$a^+a^+c^-$	$h\neq\pm k$
Absences in ½{eoo} reflections in a mixed tilt system		
18	$a^0b^-c^+$	$h\neq\pm k$
19	$a^-a^-c^+$	$h\neq\pm k$

Table 1.6. List of ORs present in pc and non-pc zone axes. Reproduced from (David I. Woodward & Reaney, 2005).

pc zone axis	**$a^0b^-c^+$**	**$a^-b^-c^+$**	**$a^-a^-c^+$**	**$a^+a^+c^-$**
[100]	½(eeo)	½(eeo)	½(eeo)	½(eeo)+½(eoe)+½(eoo)
[010]	-	½(eeo)	½(eeo)	½(eeo)+½(oee)+½(oeo)
[001]	½(ooe)	½(ooe)	½(ooe)	½(ooe)

$[110]$	½(ooo)+½(ooe)+½(eeo)	½(ooo)+½(ooe)+½(eeo)	½(ooo)	½(ooe)
$[1\bar{1}0]$	½(ooo)+½(ooe)+½(eeo)	½(ooo)+½(ooe)+½(eeo)	½(eeo)	½(ooe)
$[101]$	½(ooo)	½(ooo)	½(ooo)	½(ooo)+½(oeo)+½(eoe)

An initial comparison of $\langle 100\rangle_{pc}$ zone axes indicates that tilt systems $a^-b^-c^+$ and $a^-a^-c^+$ are indistinguishable, and $a^0b^-c^+$ is distinguishable only by the lack of ORs in one of the pc zone axes. Of the four missed tilt systems $a^+a^+c^-$ sticks out because it contains two ½{eeo} OR variants in two of the pc axes, and cumulatively all ½{eeo} and ½{ooe} ORs between the three pc axes. ½(ooo)+½(ooe)+½(eeo) ORs are expected to occur in both $a^0b^-c^+$ and $a^-b^-c^+$ making them readily distinguishable from $a^-a^-c^+$ and $a^+a^+c^-$. Distinguishing between $a^-a^-c^+$ and $a^+a^+c^-$ only requires one orientation from $\langle 101\rangle_{pc}$, since $a^-a^-c^+$ does not contain ½{ooe} reflections. To distinguish between the three three-tilt systems only a $[110]$ or $[1\bar{1}0]$ ZA is required, which is experimentally easy if the orientation of the c-axis is known.

This section thus far has discussed the existence of octahedral tilt systems and how to distinguish between them. This addresses the relative magnitude of tilt angle but does not provide for quantifiable tilt angles. The tilt angles can be quantified through SAED if kinematic conditions are appropriate. The intensity for out-of-phase ORs (i.e. ½{ooo}) is given as

$$\begin{aligned} I \propto [&(ki^l - li^k)\alpha \\ &\pm(-li^h + hi^l)\beta \\ &\pm(hi^k - ki^h)\gamma]^2 \end{aligned} \tag{1.1a}$$

and the intensity for in-phase ORs (i.e. ½{eoo}) is given as

$$I \propto (ki^l - li^k)^2\alpha^2, \text{ for } a^+ \tag{1.1b}$$

$$I \propto (-li^h + hi^l)^2\beta^2, \text{ for } b^+ \tag{1.1c}$$

$$I \propto (hi^k - ki^h)^2\gamma^2, \text{ for } c^+ \tag{1.1d}$$

(Glazer, 1975; David I. Woodward & Reaney, 2005). Quantification using the intensity of diffraction peaks must be used with caution since it requires kinematic conditions. Kinematic conditions are only valid when the first Born approximation is valid, which requires a weakly scattering potential. This is not always valid for perovskites which contain heavier A- or B-site atoms. In addition, the validity of kinematic theory depends on the distance of the Bragg condition form the Ewald sphere (referred to as the deviation parameter, s) in conjunction with sample thickness. An alternative approach is to measure the tilt angles directly through imaging. In a scanning TEM (STEM) it is possible to map heavy A- and B-site atomic columns with high-angle annular dark-field (HAADF) imaging while simultaneously mapping lighter oxygen columns with bright-field (BF), annular BF (ABF), or differential phase contrast (DPC). This for examples has been used to map the coupling of octahedral tilt across interfaces by quantifying the gradient of tilt angles (Aso et al., 2013; Biegalski et al., 2015; He et al., 2015).

In this subsection the general basis for phase transformations that result from rotating TiO_6 octahedra was reviewed. This included the introduction of Glazer notation and a diffraction-based methodology to determine the types of octahedral tilts present and their relation to softening phonon modes. Using the outlined characterization method, it will be shown in Section 9 that as the number of unit-cells in a superlattice period decreases, changes in orientation and structure of the lattice are observed.

1.3 Perovskite Oxide Superlattice and Chemical Ordering

The creation of artificial superlattices provides a means to selectively chemically order a material. Competing octahedral distortions and cation displacements, both a response of softening phonons, occur between the layers and at interfaces of superlattices. A brief introduction will be provided in this subsection. In the one small-period limit, the distinction between a superlattice and an ordered crystal becomes ambiguous, thus providing the capability to create perovskites with layered chemical ordering and octahedral ordering. For this reason, relevant studies on chemical ordering in perovskites are introduced. This background is relevant because the samples being studied herein are STO-CTO superlattices with one to twenty-seven unit-cells per superlattice layer.

Chemical ordering in perovskites will inherently change the space group much like octahedral tilting. Ordering can occur on either the A- or B- sublattices such that the crystal basis is $AA'B_2O_6$ or $A_2BB'O_6$, respectively. Herein only 1:1 ordering will be discussed, because all evaluated SLs are stochiometric. Three types of 1:1 cation ordering exist: i) rocksalt, ii) columnar, and iii) layered (King & Woodward, 2010; Young & Rondinelli, 2013). Rock salt is most common for B-site ordering and layered is most common for A-site ordering. A-site layered structures are typically stabilized by vacancies and/or second order Jahn-Teller distortions (a distortion resulting from nearly degenerate electronic states). Stabilization of A-site ordered structures due to octahedral tilting has also been discussed and found energetically favorable, one of which is $(Sr,Ca)Zr_2O_6$ (Mulder et al., 2013; Young & Rondinelli, 2013). Layered ordering is often accompanied by oriented dipoles, which can result in ferroelectricity. The unique properties arising from layered ordering is of interest to nanoscale design because materials can be artificially ordered in short-period superlattices with various growth techniques, allowing for tunability in constituent elements and therefore variable properties. The topic of superlattices will be discussed later in this section, but first an extension of the crystallography resultant from octahedral ordering in perovskites to include chemical ordering should be discussed, in addition to expression in diffraction data.

Of the 23 Glazer tilt systems only four remove the crystallographic equivalency of A-sites, thus stabilizing A-site ordering (J. H. Park et al., 1998; P. M. Woodward, 1997b). These are $a^+a^+a^+$, $a^+a^+c^-$, $a^0b^+b^+$, and $a^0b^+b^-$. The $a^+a^+a^+$ is a common system most of which are rock salt or columnar. An example of $a^+a^+c^-$ is $CaFeTi_2O_6$, which is columnar (Leinenweber & Parise, 1995). In general, layered ordering does not naturally occur in stochiometric perovskites containing two A-sites, rather anion or cation vacancies are present, or more than two A-sites are required. To describe perovskites with layered ordering Kishida et al. extended the Glazer's notation to include a capital letter for the pc axis that ordering occurs along (Kishida et al., 2009). For example, ordering occurring along the c-axis of $a^-a^-c^+$ is denoted $a^-a^-C^+$. From the 16 unique tilt systems 22 chemically and rotationally ordered tilt systems were derived which reduces to 16 unique space groups. Reflection conditions and the observed ORs along pc and non-pc axes are found within their paper. This establishes a methodology to determine the space group of lower-symmetry perovskites from simultaneous chemical and octahedral ordering.

The creation of artificial SLs provides a means to tune the softening of phonon modes and therefore the macroscopic response of a material. Examples of $ATiO_3$ SLs include lower thermal conductivity in symmetric STO-CTO SLs (i.e., macroscopically $Sr_{0.5}Ca_{0.5}TO_3$ and the samples in this study) than in a $Sr_{0.5}Ca_{0.5}TO$ alloy (Ravichandran et al., 2014), non-linear dielectric properties in $BaTiO_3$-STO (Kim et al., 2002), and improper ferroelectricity and the emergence of axially polarized vortices and skyrmions in $PbTiO_3$-STO (Bousquet et al., 2008; Damodaran et al., 2017; Das et al., 2019; Hong et al., 2017; Lu et al., 2018; Nguyen et al., 2018; Tang et al., 2017; A. K. Yadav et al., 2016). As the number of unit-cells in a layer of a SL is decreased, the material transitions from a system dominated by layers separated by interfaces to a system containing nearly as many interfaces as unit-cells in a layer. In the limit of a one unit-cell repeat, the distinction between a layer and an interface becomes ambiguous, and the system can be considered as a single phase with artificial layer ordering on the A-site sublattice. Examples of one unit-cell superlattices are found in references (Bousquet et al., 2008; Kim et al., 2002; Middey et al., 2018; Tabata & Kawai, 1997; Tabata et al., 1994). The artificial order enables access to possibly non-equilibrium crystal structures in systems that prefer solid solutions or non-layered ordering. This artificial ordering thus enables a way to leverage interfacial phenomena and/or non-equilibrium chemically ordered structures. Examples of macroscopic manifestation of interfacial phenomena are observed in three layer SL (Lee et al., 2005; Tokura, 2007; Warusawithana et al., 2003; Zubko et al., 2011).

In this subsection, chemical ordering in perovskite oxides was briefly introduced. The extension of Glazer notation to include layered ordering was discussed which allows for space group determination of perovskites containing layered chemical ordering and octahedral ordering via the tables in reference (Kishida et al., 2009). The small unit-cell limit of superlattices is equivalent to an artificially ordered lattice. The physical relevance of such superlattices was discussed. This Section is relevant to this study because the samples are STO-CTO superlattices with the number of unit-cells in a period ranging from one to 27. In addition, phase transformations and orientation changes are observed when the number of unit-cells in a layer decreased using SAED, shown in Section 9, which requires proper understanding of the diffraction data in chemically and octahedrally ordered perovskites.

1.4 Phases in $SrTiO_3$, $CaTiO_3$, and $(Sr_{0.5},Ca_{0.5})TiO_3$

Phase transformations resulting from octahedral tilting in $ATiO_3$ perovskites was introduced in Section 1.2. It is pertinent to discuss the phase transformations of the monolithic constituents, STO and CTO, to provide perspective and comparison to phases observed in the SLs in this research. In this subsection, phases of STO and CTO are discussed. Similarly, phases of SCTO, which contains the same macroscopic composition of symmetric STO-CTO SLs, are discussed.

STO is a prototypical perovskite oxide with a $Pm\bar{3}m$ space group at ambient conditions. At ~105K STO TiO_6 octahedra rotate from the softening of the $R'_{15}(F_{1g})$ anti-ferrodistortive mode at ½(111) BZ edges, causing a transformation to a body-centered tetragonal lattice with I4/mcm symmetry (Aschauer & Spaldin, 2014; Ostapchuk et al., 2002). The I4/mcm space group corresponds to Glazer tilt system 22 $a^0a^0c^-$, representing a single antiphase TiO_6 tilt axis. The antiphase twisting of the octahedra results in a doubling of the unit-cell along $[001]_{pc}$ (Glazer, 1975), as shown in Figure 1.2c-e. The transformation matrix relating I4/mcm to the pc axes is,

$$T = \begin{bmatrix} -1 & 1 & 0 \\ 1 & 1 & 0 \\ 0 & 0 & 2 \end{bmatrix}$$

which rotates the a and b axes projecting them to $[\bar{1}10]_{pc}$ and $[110]_{pc}$, respectively, and doubles the c-axis. At ~37K the F_{1u} ferroelectric mode theoretically softens to form ferroelectric STO; however, hyper-Raman experiments at liquid-He temperatures have shown that complete softening of the ferroelectric mode is suppressed by coupling with the anti-ferrodistortive mode (zero-point motion) making STO an incipient ferroelectric (also named a quantum paraelectric) (K. A. Müller & Burkard, 1979; Fang, 2013; K. Alex Müller et al., 1991; Ostapchuk et al., 2002; Yamanaka et al., 2000; Kamarás et al., 1995). Transitioning through this “quantum critical point” has been the subject of many studies. One such way to transition to the ferroelectric regime is through doping with ^{18}O or Ca, which not only turns STO into a ferroelectric but also a superconductor (Bednorz & Müller, 1984; Itoh et al., 1999; Rischau et al., 2017; R. Wang & Itoh, 2001). Another method is through epitaxial strain (Haeni et al., 2004). Ferroelectric STO shares the same tetragonal unit-cell as I4/mcm, therefore monolithic STO only shows unit-cells with a maximum dimension of $\sqrt{2}a_{pc} \times \sqrt{2}a_{pc} \times 2a_{pc}$. This presents the phases of STO, one of the constituents of the superlattices.

In Pbnm CTO at room temperature and pressure, systematic tilting of TiO_6 octahedra with Glazer notation $a^-a^-c^+$ are present. The unit-cell shares the same projection into the pc unit-cell as I4/mcm STO, but with unequal dilation of the a and b axes. The octahedral rotations and change in space-group give rise to ordered reflections that appear at ½ of the *aristotype* unit-cell, as previously discussed in Section 1.2. In the $[010]_{pc}$ and $[100]_{pc}$ zone axis (ZA) selected-area diffraction patterns (SADPs) of Pbnm CTO, systematic tilting of TiO_6 octahedra produces ORs at ½{oee} (e.g. $½\{102\}_{pc}$). CTO I4/mcm symmetry occurs between ~1250 and ~1374 °C, like STO has below 105°C. Above ~1374 °C, CTO is cubic with a $Pm\bar{3}m$ space group. The sequence of phase transformations Pbnm→I4/mcm→$Pm\bar{3}m$ has a maximum unit-cell dimension of $\sqrt{2}a_{pc} \times \sqrt{2}a_{pc} \times 2a_{pc}$, similar to STO. A second orthorhombic phase with space group Cmcm has debatably been present in the temperature range ~1173-1227°C, however the most modern reports rule out this phase (Ali & Yashima, 2005; Guyot et al., 1993; Kennedy et al., 1999; Redfern, n.d.). With the presence of the Cmcm phase, the phase transformations can be described as the softening of an *R*-point phonon ($Pm\bar{3}m$ $a^0a^0a^0$ to I4/mcm $a^0a^0c^-$), then the softening of an *M*-point phonon[2] (I4/mcm $a^0a^0c^-$ to Cmcm $a^0b^+c^-$), then the softening of another *R*-point mode (Cmcm $a^0b^+c^-$ to Pnma $a^-b^+a^-$, which can also be set as Pbnm $a^-a^-c^+$) (Železný et al., 2002). Without the Cmcm intermediate a softening of coupled *R*- and *M*-point modes is thought to occur(Parlinski et al., 2001). The phase transitions in CTO share a similar sequence to that of

---

[2] It is worth noting that the BZ positions of the tetragonal and orthorhombic lattices can be back projected to the cubic unit-cell such that softening is described by their high-symmetry counterpart. See for example the relation of cubic to orthorhombic modes in Table II of reference (Železný et al., 2002).

STO with the softening of R- and M-point phonons, but at slightly elevated temperatures. This presents the phases of CTO, one of the constituents of the superlattices.

There is extensive debate in the literature about the room temperature phase of SCTO. Initial X-ray diffraction (XRD) and synchrotron experiments of SCTO reported a Cmcm space group that has a $2a_{pc} \times 2a_{pc} \times 2a_{pc}$ unit-cell (Ball et al., 1998). Distinguishing between Cmcm and Pnma space groups in perovskite oxides is rather difficult using X-ray based techniques. Observation of ORs and extinction rules along specific ZAs using SAED can distinguish between the two space groups, and this lead Howard et al. to the conclusion that SCTO was Pnma and not Cmcm (Howard et al., 2001). This was in agreement with the later SAED, convergent-beam electron diffraction (CBED), and neutron scattering experiments performed by Ranjan et al. (Mishra et al., 2006; Ranjan et al., 2001). In contrast, more recent work by Woodward et al. suggests a $P2_1/m$ space group (D I Woodward et al., 2006). Needless to say, the room temperature phase for SCTO is under debate. Regardless of the correct phase, SCTO does not exhibit any ferroelectric or anti-ferroelectric properties, however, at lower Ca concentrations ($x < 40$) anti-ferroelectricity is realized, making SCTO an incipient anti-ferroelectric (Anwar & Lalla, 2008; Mishra et al., 2006; Ranjan & Pandey, 2001a, 2001b; Ranjan et al., 2001; Ranson et al., 2005).

In this subsection the phases of STO, CTO, and SCTO were discussed. The space groups $Pm\bar{3}m$ and I4/mcm occur in both STO and CTO. The space group Pbnm and arguably Cmcm is observed in both CTO and SCTO. This provides a framework of phases present in the two end members and at the macroscopic composition of the superlattice.

2 Phonons

Phonons are responsible for material properties such as heat capacity, thermal conductivity, and optical conductivity in ionic solids. They are also responsible for the phase transformations in perovskites as discussed in Section 1.2. To understand the vibrational spectra presented in Section 12 and the simulated spectra in Section 11 an understanding of the dipole approximation (Section 5.2) and the connection between phonons and permittivity must be established. The connection between phonons and permittivity is made in Section 2.1 and the characterization of phonons using vibrational EELS is then presented in Section 2.2.

2.1 From Phonons to Permittivity

In this subsection the relation between phonons and a materials permittivity is introduced. This begins with a discussion of atomic polarization of an ion followed by the polarization of an ionic dipole. These treatments establish the basis for the Lorentz-Drude and factorized dielectric functions, which can be used to model EELS through the dipole formalism discussed in Sections 5.2 and 6, and characterize the vibrational response of materials. This will enable development of the theory used to simulate the vibrational EELS spectra expected for STO and CTO, and STO/CTO and vacuum/ATO interfaces, for later comparison with experimental vibrational EELS spectra of STO-CTO superlattices.

The ionic polarizability of an atom in an ionic material can be treated as an electronic shell with charge Ze and mass $M = Zm_e$ (where Z is the valence number, e is the elementary charge, and m_e is the mass of an electron) bound to the ion-core with a spring constant C. Newton's

Equation of motion describing displacement ($\boldsymbol{u}$) of the bound oscillator is therefore

$$M\frac{\partial^2 \boldsymbol{u}_{atom}}{dt^2} = -C\boldsymbol{u}_{atom} \qquad 2.1$$

Assuming the motion of the oscillator is time harmonic, then the natural frequency of atomic polarization is found from solving Equation 2.1;

$$\omega_0^2 = \frac{C}{M} \qquad 2.2$$

If a frictional and driving force are included the Equation of motion is,

$$M\frac{\partial^2 \boldsymbol{u}_{atom}}{dt^2} = -M\gamma\frac{\partial \boldsymbol{u}_{atom}}{dt} - M\omega_0^2\boldsymbol{u}_{atom} - \mathrm{Z}e\boldsymbol{E} \qquad 2.3$$

where γ is a damping constant (inverse lifetime) and $\boldsymbol{E}$ is an electric field. Combining Equations 2.2 and 2.3 the driven displacement of the polarized ion is,

$$\boldsymbol{u}_{atom} = -\frac{e\boldsymbol{E}}{m_e(\omega_0^2 - \omega^2 + i\omega\gamma)}$$

Polarization is defined as,

$$\boldsymbol{P_i} = n_i\boldsymbol{p}_i$$

where $\boldsymbol{p}_i = -Ze\boldsymbol{u}_i$ is the dipole moment, n_i is the number density of the oscillator i, and $n_e=Zn_i$ is the valence electron density contributed from the ion. Therefore, the atomic $\boldsymbol{P}$ induced by $\boldsymbol{E}$ is

$$\boldsymbol{P}_{atomic} = \frac{n_e e^2}{m_e}\frac{\boldsymbol{E}}{\omega_0^2 - \omega^2 + i\omega\gamma}$$

The total susceptibility of a material is defined as the polarization field induced relative to an electric field in vacuum,

$$\chi = \frac{\boldsymbol{P}}{\varepsilon_0\boldsymbol{E}} \qquad 2.4$$

Therefore, the susceptibility from only atomic polarizations is

$$\chi_{atomic} = \frac{n_e e^2}{\varepsilon_0 m_e}\frac{1}{\omega_0^2 - \omega^2 + i\omega\gamma} \qquad 2.5$$

Equation 2.5 is the Lorentz-Drude susceptibility and the pre-factor

$$\omega_p^2 = \frac{n_e e^2}{\varepsilon_0 m_e}$$

is the square of the plasma frequency. When the electrons are unbound (ω_0=0), like in a free-electron metal, Equation 2.5 reduces to the Drude susceptibility.

If we now, consider the relative displacement of a pair of electrostatically bound ions from equilibrium,

$$\boldsymbol{w} = \boldsymbol{u}_c - \boldsymbol{u}_a$$

whose charges are $\pm Ze$ and masses are m_c and m_a, then the $\boldsymbol{p}$ of the ion pair is

$$\boldsymbol{p}_{ionic} = Ze\boldsymbol{w}$$

The individual ion displacements are found again from Newton's Equation of motion, but since the ions are coupled the motion is best written in terms of $\boldsymbol{w}$;

$$M\frac{\partial^2 \boldsymbol{w}}{dt^2} = -C\boldsymbol{w}$$

where M is the reduced mass of the ions; $M^{-1} = m_c^{-1} + m_a^{-1}$. The solution has the same form as Equation 2.1 but the mass is now the reduced mass of the ion pair instead of an electron. Therefore, the vibration of ionic dipoles is much lower frequency than the vibration of the electronic vibrations of the individual ions. The relative displacement for a driven system is found by including both a damping and driving forces into the equation of motion, much like Equation 2.3;

$$\boldsymbol{w} = \frac{e\boldsymbol{E}}{M(\omega_0^2 - \omega^2 + i\omega\gamma)}$$

noting that $\boldsymbol{w}$ is positive while $\boldsymbol{u}_{atomic}$ was negative, and that we retain the reduced mass since the motion is still coupled. It follows that

$$\chi_{ionic} = \frac{n_e e^2}{M\varepsilon_0}\frac{1}{\omega_0^2 - \omega^2 + i\omega\gamma} \qquad 2.6$$

The pre-factor is like ω_p^2 but contains an effective mass. Other polarizations follow the same trend, and the pre-factor is defined as the general oscillator strength (f). Comparing f for ionic vibrations and electronic vibrations, the latter is expected to be much larger.

The electric displacement ($\boldsymbol{D}$) in a material,

$$\boldsymbol{D} = \varepsilon \boldsymbol{E} \qquad 2.7$$

where $\varepsilon = \varepsilon_0 \varepsilon_r$ is permittivity, ε_0 is the permittivity of free-space, and ε_r is relative permittivity, can be partitioned into the field that would naturally occur in vacuum and the field that occurs from induce polarizations;

$$\boldsymbol{D} = \varepsilon_0 \boldsymbol{E} + \boldsymbol{P} \qquad 2.8$$

Relating Equation 2.4, 2.7, and 2.8 provides the relation between ε_r and χ;

$$\varepsilon_r = 1 + \sum \chi_i \qquad 2.9a$$

ε_r is an imaginary function when damping is included in χ. ε' and ε" refer to the real and imaginary components of ε_r. Using the χ_i in Equations 2.5 and 2.6 the Lorentz-Drude permittivity is obtained;

$$\varepsilon_r = 1 + \sum_{j}^{atomic,ionic} \frac{f_j}{\omega_{0,j}^2 - \omega^2 + i\omega\gamma} \qquad 2.9b$$

where f_j is the generalized oscillator strength. We are typically not interested in the full range of frequencies so the summation of Equation 2.9 is broken into susceptibilities near the frequencies of interest and susceptibilities with too high of resonant frequencies resulting in an “out of phase” background;

$$\varepsilon_r = \varepsilon_\infty + \sum \chi_i$$

where ε_∞ is the high frequency permittivity related to the polarization and displacement of over driven oscillators. For example, if we are concerned with optical lattice vibrations then the electronic polarization ions will contribute to ε_∞ because $\omega_{0,atomic} \gg \omega_{ionic}$ and the Lorentz-Drude model, Equation 2.9b, becomes

$$\varepsilon_r = \varepsilon_\infty + \sum_{j}^{ionic} \frac{f_j}{\omega_{TO,j}^2 - \omega^2 + i\omega\gamma} \qquad 2.10$$

where the ω_{TO} is the natural resonance frequency of a transverse optic (TO) mode.

If we also consider the static limit of the Lorentz-Drude permittivity, where vibrations are under driven ($\varepsilon_s = \varepsilon_r(0)$), for one near resonant vibration we get

$$\varepsilon_s = \varepsilon_\infty + \frac{f}{\omega_{TO}^2} \qquad 2.11$$

Combining Equations 2.10 and 2.11 the ε_r is obtained as a function of measurables ε_r and ε_∞;

$$\varepsilon_r = \varepsilon_\infty + (\varepsilon_s - \varepsilon_\infty)\frac{\omega_{TO}^2}{\omega^2 - i\gamma\omega} \qquad 2.12$$

In a crystal, longitudinal modes exist in addition to transverse modes. Longitudinal optic (LO) modes exist when ε_r=0, therefore providing the Lyddane-Sachs-Teller relationship,

$$\omega_{LO}^2 = \frac{\varepsilon_s}{\varepsilon_\infty}\omega_{TO}^2 \qquad 2.13$$

which describes the relation between long wavelength LO and TO modes. Combining Equations 2.12 and 2.13 provides

$$\varepsilon_r = \varepsilon_\infty\left(1 + \frac{\omega_{LO}^2 - \omega_{TO}^2}{\omega_{TO}^2 - \omega^2 - i\gamma\omega}\right) \qquad 2.14$$

Figure 2.1(a) shows the real and imaginary component of the in-plane permittivity for hexagonal BN as described by Equation 2.14.

The real component of Equation 2.14 is negative when $\omega_{TO} < \omega < \omega_{LO}$, which defines a band of frequency that vibrations do not occur within the bulk of a material, as shown in Figure 2.1 for hexagonal BN. This band is known as a Reststrahlen band. The abbreviation Ph for phonon is used in Figure 2.1 and the following text. Surface vibrations or surface phonons (SPh) occur within the Reststrahlen band and will be considered in more detail in Section 6.1. Equations 2.11-2.13 have been generalized and result in a more general factorized form[3] of the Lyddane-Sachs-Teller relationship and dielectric function,

$$\frac{\varepsilon_s}{\varepsilon_\infty} = \prod \frac{\omega_{LO}^2}{\omega_{TO}^2} \qquad 2.15$$

$$\varepsilon_r = \varepsilon_\infty \prod \frac{\omega_{LO,j}^2 - \omega^2 - i\omega\gamma_{LO,j}}{\omega_{TO,j}^2 - \omega^2 - i\omega\gamma_{TO,j}} \qquad 2.16$$

respectively (Cochran & Cowley, 1962; Kurosawa, 1961; Sievers & Page, 1990). Thus, the singularities for the vibrational response in materials are defined within their ε_r as,

$$\Omega_j = \sqrt{\omega_j^2 \pm \frac{\gamma_j^2}{4}} \qquad 2.17$$

where Ω are the poles. $\Omega_{LO} = \omega_{LO}$ and $\Omega_{TO} = \omega_{TO}$ (i.e. the singularities in ε_r) when damping is zero (Sievers & Page, 1990). Therefore, techniques capable of characterizing ε_r, such as Fourier transform infrared spectroscopy (FTIR) or EELS, can identify the ω_{LO} and ω_{TO} modes in a material.

---

[3] This is valid for orthorhombic symmetry and higher. Generalization for lower symmetry is found in reference (Cochran & Cowley, 1962).

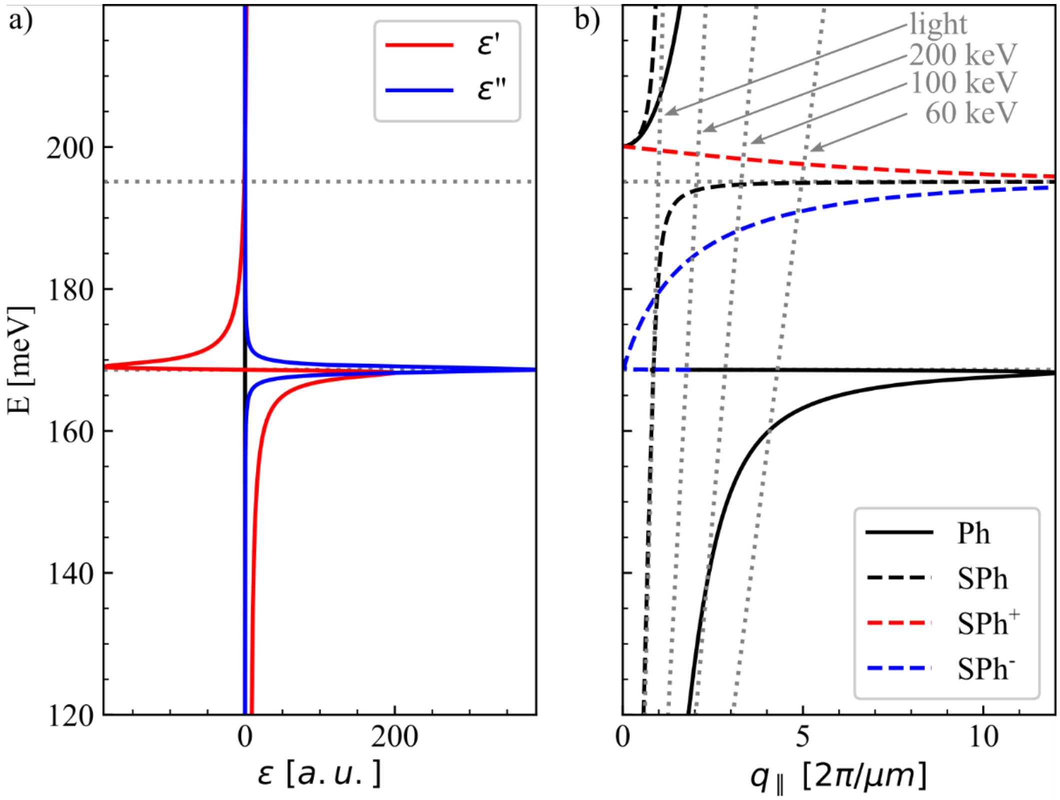

Figure 2.1. Lorentz-Drude in-plane permittivity (a) for hexagonal-BN with ω_{TO}=168.62, ω_{LO}=200.11, and γ=0.87 meV measured in reference (Caldwell et al., 2014). The dotted horizontal lines mark the LO and TO frequencies and between them ε''<0 is the Reststrahlen band. Note that ε'' remain finite when damping is included. The Ph dispersion outside the Reststrahlen band and SPh dispersion within are shown in (b). Coupled symmetric and asymmetric SPh are shown in (b) for a 200 nm film. The light and electron lines in (b) show what (S)Ph polariton modes will be excited and what modes are radiative, as discussed in Section 6.1.

This subsection established the connection between lattice vibrations and permittivity required for the EELS dipole approximation discussed in Section 5.2, which is used to describe vibrational EELS under specific conditions. This subsection therefore provides background for later vibrational EELS simulations and vibrational EELS experiments, shown in Sections 11 and 12, respectively.

2.2 Vibrational Electron Energy-Loss Spectroscopy

This subsection describes the current state of vibrational EELS in a (S)TEM. This is done to convey the relative infancy of the vibrational spectroscopy technique, which we will later provide further experimental data for, thus progressing the understanding of applications, capabilities, and gaps in current understanding.

With state-of-the-art monochromated STEM it is now possible to probe the vibrational response of materials with high spatial resolution using EELS (Egerton, 2014; Krivanek et al., 2014). This for example, allows for probing the localized surface phonon response in nanostructures such as nano-cubes (Maureen J Lagos et al., 2018; Maureen J. Lagos et al., 2017), nano-particles (Venkatraman, March, et al., 2018a), and nano-rods (Li et al., 2020; Qi et al., 2019). Vibrational EELS has also been used to map heterogeneity of oxygen coordination in aluminosilicate glasses (Liao et al., 2020) and the response from Si/SiO_2 interfaces (Venkatraman, March, et al., 2018b; Venkatraman, Rez, et al., 2018). Initial experiments showed that spatial resolution varied from hundreds of microns to nanometers depending on the region of momentum space collected (Dwyer et al., 2016). Extensive research has been performed to determine the scattering nature of vibrational EELS and has determined that two signals exist: i) delocalized scattering from dipoles, and ii) localized impact scattering.

Using impact scattering vibrational response with atomic-resolution is now capable enabling measurements such as the vibrational response of single Si substitutional atoms in graphene (F. S. Hage et al., 2020). Such high spatial resolution is achieved by circumventing the delocalized signal, which contributes lower signal at high $\boldsymbol{q}$, or by using a material that lacks vibrations with induced dipoles (F. S. Hage et al., 2019; Senga et al., 2019; Venkatraman et al., 2019). The $\boldsymbol{q}$ dependence also brought attention to the capability of vibrational EELS in a STEM to measure phonon dispersions from small volumes. Examples extend from differentiation of cubic and hexagonal BN (Fredrik S. Hage et al., 2018; Nicholls et al., 2019) to dispersion measurements from single SiC nano-rods (Li et al., 2020).

The delocalization of dipole scattering has its advantages. For example, the delocalization interaction of the probe with the electric field in a sample allows for phonon measurements when an electron probe is in the vacuum. This is known as an “aloof” geometry and lends itself to studying radiation sensitive materials, because the sample in minimally exposed to the high-energy electrons (Collins et al., 2020; Haiber & Crozier, 2018; Jokisaari et al., 2018; Radtke et al., 2019; Rez et al., 2016; Venkatraman, March, et al., 2018a; Vollmer et al., 2019).

Application of vibrational EELS in a STEM extends past measurement of nanostructures. Already mentioned examples include measurements from Si substitutions in graphene and oxygen coordination in aluminosilicate glasses (F. S. Hage et al., 2020; Liao et al., 2020). Other studies include isotopic label mapping (Hachtel et al., 2019) and measurement of hydrogen defects that are detrimental to the photocatalytic response of graphitic nitrides (Haiber & Crozier, 2018). The most explored application vibrational EELS is local thermometry (M. J. Lagos & Batson, 2018; Maureen J. Lagos & Batson, 2018; Yan et al., 2019). Such measurements involve ratioing energy-gain peaks (phonon transferring energy to the electron) with energy-loss peaks. Another method was recently proposed to extract specific heat and thermal conductivity by measuring the shape and full-width at half maximum of the zero-loss peak (ZLP) (Idrobo et al., 2019). This circles back to the earliest measurements in STEM-EELS of STO by Egovali et al. that showed collective phonon response of individual atomic columns could be measured by measuring deviations in the ZLP (Egoavil et al., 2014).

In this sub-Section the scattering mechanisms measured using vibrational EELS were discussed with regards to their spatial resolution and/or applicability to various material systems. Applications of vibrational method were discussed including measurement of optically relevant nanostructures, isotopic and hydrogen identification, and thermal measurements. This lays the foundation for our work to extend the capability and understanding of vibrational EELS and portrays the novelty of the technique.

3 Diffraction

In this section the basic premise of diffraction is introduced followed by a discussion of various electron diffraction techniques in a TEM.

The amplitude of an elastically scattered electron wave, ψ_{el}, in the first-Born approximation at position $\boldsymbol{r}$ from a scattering potential $V(\boldsymbol{r}')$ is given as

$$\psi_{el}(\boldsymbol{q},\boldsymbol{r}) = -\frac{m_e}{2\pi\hbar^2}\frac{e^{i\boldsymbol{k}\cdot\boldsymbol{r}}}{|\boldsymbol{r}|}\int V(\boldsymbol{r}')e^{-i\boldsymbol{q}\cdot\boldsymbol{r}'}d^3\boldsymbol{r}'$$

with electron mass m_e, final wavevector $\boldsymbol{k}$, incident wavevector $\boldsymbol{k}_0$, and $\boldsymbol{q} = \boldsymbol{k} - \boldsymbol{k}_0$ (Fultz & Howe, 2013). The intensity of the scattered wave is given as $I = \frac{|\psi^*_{el}(\boldsymbol{q})|^2}{|\boldsymbol{r}-\boldsymbol{r}'|^2}$. If we consider atomic scattering centers at positions $\boldsymbol{R}_j$ then $V(\boldsymbol{r}') = \sum_{\boldsymbol{R}_j} V_{at}(\boldsymbol{r}' - \boldsymbol{R}_j)$. Ignoring the $1/|\boldsymbol{r}_j|$ dependence and defining $\boldsymbol{r} = \boldsymbol{r}' - \boldsymbol{R}_j$ with $\boldsymbol{r}$ and $\boldsymbol{R}_j$ being independent then

$$\psi_{scatt}(\boldsymbol{q}) = \sum_{\boldsymbol{R}_j}\left(-\frac{m_e}{2\pi\hbar^2}\int V_{at,\boldsymbol{R}_j}(\boldsymbol{r})e^{-i\boldsymbol{q}\cdot\boldsymbol{r}}d^3\boldsymbol{r}\right)e^{i\boldsymbol{q}\cdot\boldsymbol{R}_j} \qquad 3.1$$

The parenthetical term is defined as the atomic form factor for electron scattering, $f_{el}(\boldsymbol{R}_j,\boldsymbol{q})$, such that Equation 3.1 is written

$$\psi_{scatt}(\boldsymbol{q}) = \sum_{\boldsymbol{R}_j}^{All\ atoms} f_i e^{-i\boldsymbol{q}\cdot\boldsymbol{R}_i} \qquad 3.2$$

In a periodic lattice an atom position is expressed as the sum of its basis position ($\boldsymbol{r}_g$) and the position of the lattice it resides in ($\boldsymbol{r}_k$).

$$\boldsymbol{R_j} = \boldsymbol{r}_g + \boldsymbol{r}_k \qquad 3.3$$

The scattering strength in f_{el} depends on the potential within a unit-cell, therefore $\boldsymbol{r}_g$ provides a periodicity to f_{el} so that Equation 3.3 can be expressed as a shape factor $S(\boldsymbol{q})$, which describes the interference from consecutive unit-cells, and structure factor $F(\boldsymbol{q})$, which describes the interference from the screened columbic potential within a unit-cell.

$$\psi_{scatt}(\boldsymbol{q}) = S(\boldsymbol{q})F(\boldsymbol{q}) \qquad 3.4a$$

$$S(\boldsymbol{q}) \equiv \sum_{r_g}^{N} e^{-i\boldsymbol{q}\cdot\boldsymbol{r_g}} \qquad 3.4b$$

$$F(\boldsymbol{q}) \equiv \sum_{\boldsymbol{r}_k}^{basis} f_{el}(\boldsymbol{r}_k) e^{-i\boldsymbol{q}\cdot\boldsymbol{r}_k} \tag{3.4c}$$

When $\boldsymbol{q}$ is a reciprocal lattice vector then the exponent of Equation 3.4c is zero and F is a maximum (likewise I), this is known as the Bragg condition or Laue condition. This is equivalent to the Ewald sphere intersecting a reciprocal lattice point, as shown in Figure 3.1. The curvature of the Ewald sphere and the three-dimensional nature of a reciprocal lattice results in zones of interSection known as Laue zones. The zero, first, second, and higher-order Laue zones (ZOLZ, FOLZ, SOLZ, HOLZ, respectively) are shown in Figure 3.1a.

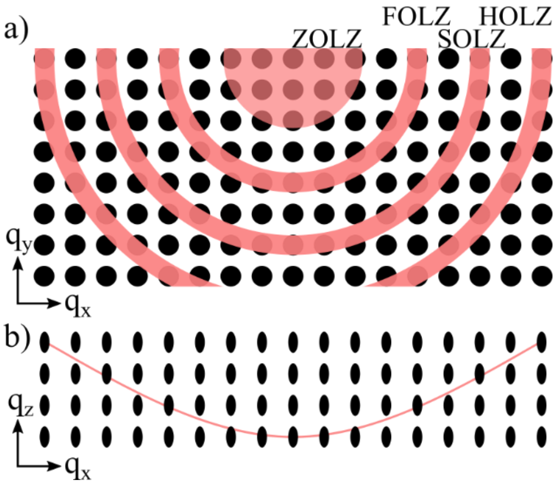

Figure 3.1. Ewald sphere intersection of a simple cubic reciprocal lattice viewed along the z- (a) and y-axis (b). The ZOLZ, FOLZ, SOLZ, HOLZ are shown in (a) as shaded regions. In (b) the Laue condition is relaxed such that the Bragg peaks are elliptical.

S does not depend on the content of the crystal but rather the number of unit-cells in the sample. The intensity can be found using a Taylor series expansion and trigonometric identities:

$$|S_i|^2 = \frac{\sin^2\left(\frac{1}{2}q_i a_i N_i\right)}{\sin^2\left(\frac{1}{2}q_i a_i\right)} \cong \frac{\sin^2\left(\frac{1}{2}q_i a_i N_i\right)}{\left(\frac{1}{2}q_i a_i\right)^2} \tag{3.5}$$

where *a* is the lattice parameter, *N* is the number of unit-cells, and the subscript *i* indicates the vector component. The denominator of Equation 3.5 acts as an envelope function rapidly decreasing the intensity of Bragg reflections away from the exact Bragg condition. At a Bragg condition Equation 3 provides $|S_i|^2 = N_i^2$ and the envelope function in 3.5 describes an exponential decay. The numerator of Equation 3.5 is sinusoidal resulting in satellite peaks appearing next to Bragg reflections, however in practice the envelope function makes the intensity of the satellite peaks weak compared with the central peak. Another result of the sinusoidal numerator is that the width of Bragg reflections scale as $(N_i a_i)^{-1}$. For example, in a thin TEM specimen the thickness of the foil is exceedingly small such that $N_z \ll N_{x,y}$ and the Bragg reflections expand along q_z into ellipsoidal rods, as shown in Figure 3.1b. The broadening of the Bragg reflections means that the Ewald sphere does not directly need to intersect a reciprocal lattice point for intensity to be observed, this is known as relaxation of the Laue condition. Laue zone relaxation enables intersection of reciprocal lattice planes along q_z, known as Laue zones. The ZOLZ only allows access to the two dimensionally projected symmetry of the crystal. By including other Laue zones information of the space group can be characterized in addition to the lattice constants.

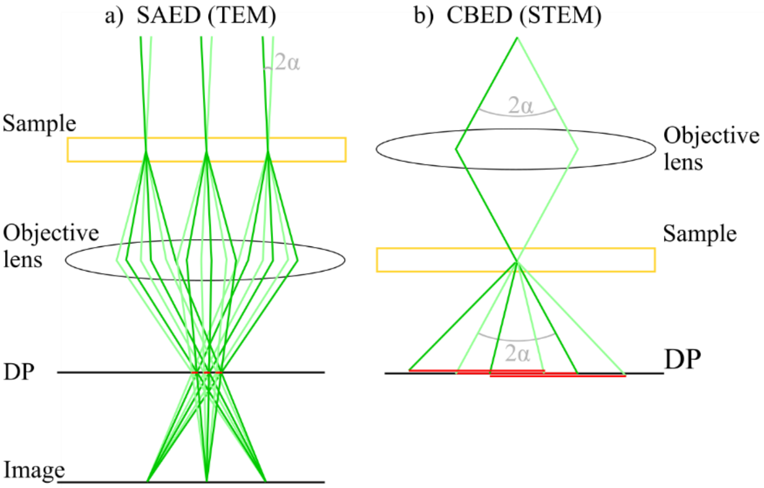

Figure 3.2. Ray diagrams for a broad TEM beam and a converged STEM probe. Larger semi-conversance angles (α) in CBED result in overlapping discs while nearly parallel illumination in TEM results in spots, as shown by red lines.

Electron diffraction in a TEM can be classified into three categories: i) SAED, ii) nano-beam electron diffraction (NBED), and iii) CBED. Schematics of SAED and CBED are shown in Figure 3.2. Each of the three techniques provides its own advantages and the provided information will be described in the following introductory text. The range of incident wavevectors used in the three techniques is the primary distinguishing quantity and is described by the semi-convergence angle (α). α is measured using the half-width at half-maximum of the forward scattered Bragg reflection. This ranges from near parallel illumination using SAED ($\alpha \approx 10^{-3}$ mrad) to a wide variation in wavevector using CBED ($\alpha > 10$ mrad), as shown in Figure 3.2. One obvious advantage of SAED is therefore its momentum resolution, however this comes at the cost of spatial resolution. CBED has the opposite resolutions and NBED has an intermediate value of spatial and momentum resolution. Various diffraction techniques will be used in Section 9 to understand the evolution in crystal structure as the number of unit-cells in a SL layer is reduced.

The most conventional form of diffraction in a TEM is SAED. SAED is operated in TEM mode with broad illumination containing electrons with (nearly) parallel initial wavevector. The broad nature of the electron beam and small α provides for diffraction from a large field of view. A selected-area aperture can be inserted into the first image plane formed after the objective lens to limit the real-space area from where electrons originate. This is effectively a real-space filter which controls electrons contributing to the SAED pattern (SADP). The smallest selected-area apertures in a TEM are typically ~150 nm. Therefore, SAED is not ideal for sampling from volumes that require high spatial resolution, but rather large fields of view and enables high momentum resolution.

As the convergence angle is increased, broadening the sharp diffraction peaks to discs, the electrons start converging to a smaller area in real space forming a probe. This probe can then be scanned and is the basis of STEM. NBED has a moderate convergence angle and probe size. For this reason, scanning-NBED (a 4D-STEM technique acquiring a NBED pattern at every pixel) is now used for strain mapping and phase identification. This 4D-STEM technique avoids real space artifacts such as drift, but leads to large data sets. A review of 4D-STEM can be found in the review article by Colin Ophus (Ophus, 2019). CBED atomic spatial resolution but extremely poor momentum resolution. In STEM the integrated intensity of the diffraction pattern is collected on an annular detector or on a round detector for annular DF (ADF) and BF, respectively, therefore not requiring high momentum resolution. Scanning-CBED can be performed much like scanning-NBED but the poor momentum resolution provides for less accuracy in $\boldsymbol{q}$ space measurements. There is a caveat that has been employed with the recent advancements of 4D-STEM. That is, by utilizing the HOLZ in a CBED pattern acquired at each pixel the lattice parameter and interplanar spacing perpendicular to the electron probe can be acquired at each pixel. For example, Nord et al. observed the octahedral ordering and interface coupling in a perovskite system consisting of $LaFeO_3$ between $La_{0.7}Sr_{0.3}MnO_3$ and $SrTiO_3$, by characterizing the intensity of an ordered Laue zone in $LaFeO_3$ (Nord et al., 2019).

In this subsection the basic theory of electron diffraction was presented. Various electron diffraction techniques, namely SAED, NBED, and CBED, were then presented. The three techniques allow for characterization of different length scales and will be utilized in the analysis of STO-CTO SLs.

4 High-angle Annular Dark-field and Differential Phase Contrast

In this section HAADF and DPC are described with enough background to understand the results presented in Section 9.1 and 9.2.

In STEM annular detectors collect the scattered signal at a range of momentum transfer. That is, the annular detector integrates the intensity of electrons scattered onto the annulus at each pixel of the rastered STEM image. STEM imaging with annular detectors uses incoherent scattering processes and the STEM image formed at all angles is an image of the scattering object convolved with the probe. The probe shape is affected by geometric aberrations that result from imperfect electromagnetic lenses and is one of the major limiting factors in the spatial resolution in a STEM. State-of-the-art STEMs are equipped with aberration correctors which can systematically correct multiple orders of geometric aberrations thus providing both symmetric and intense sub-angstrom probes.

The type of information transferred to the detector is determined by its inner and collection angle. A distinct advantage of STEM over TEM mode is that multiple annular detectors can be used simultaneously so that images with contrast from different physical origins can be compared. Four scattering regions are typically defined: 1) bright-field (BF) that only images with the forward scattered disc, 2) low-angle annular dark-field (LAADF), which has an inner collection angle slightly larger than the bright-field disc, 3) high-angle annular dark-field (HAADF), which has an inner collection angle of roughly three times the bright-field disc, and 4) medium-angle annular dark-field (MAADF), which has an intermediate collection angle (Nellist, 2019). The most common form of annular signal is HAADF. HAADF provides contrast proportional to atomic number, $I \propto Z^{1.7}$, and is often referred to as Z-contrast imaging (Crewe et al., 1970). LAADF and MAADF primarily show diffraction contrast with LAADF being highly sensitive to lattice defects and strain. BF signal is associated with phase contrast imaging that one sees in TEM and results from the overlap and interference effects of the non-diffracted and Bragg-diffracted beams. To eliminate the effects of phase contrast in BF signal an annular BF (ABF) detector can be used. ABF signal shows a reverse contrast of atomic columns seen in HAADF signal, in addition to lighter elements. For this reason, simultaneously acquired HAADF and ABF signals are often used for imaging light elements such as oxygen.

The STEM imaging methods above rely on annular detection. An alternative imaging method is acquiring 4D-STEM data sets and then forming images from user-defined scattering regions, as described in Section 3. With the user-selected regions, annularly integrated images can be formed equivalent to an annular detector. Another technique for imaging in STEM is using the change in center-of-mass (COM) of the BF disc that results from momentum transfer from the sample to the incident electron. The best annular resolution for the shifted COM is achieved using a pixelated detector, however the data transfer of these 4D-datasets can be limiting. Alternatively, segmented annular detectors are used to measure the relative change in COM allowing for smaller datasets. This imaging technique is known as differential phase contrast (DPC). The change in COM is directly proportional to the gradient of the samples electromagnetic potential ($\nabla\Phi$) and for a non-magnetic material is equal to the electric field (Close et al., 2015; Ishizuka et al., 2017; Lazić et al., 2016; K. Müller et al., 2014; Shibata et al., 2012; Yücelen et al., 2018).

$$\boldsymbol{I}^{COM}(\boldsymbol{r}) = \frac{1}{2\pi}\left(|\psi_0|^2 \otimes \nabla\Phi\right)(r) \qquad 4.1$$

The COM is the divergence of the integrated COM (iCOM)

$$\boldsymbol{I}^{COM} = \nabla \cdot \boldsymbol{I}^{iCOM} \qquad 4.2$$

allowing for Equation 4.1 to be integrated through a Fourier transform

$$\mathcal{F}\{\boldsymbol{I}^{iCOM}(\boldsymbol{r})\} = \frac{\boldsymbol{k} \cdot \mathcal{F}\{\boldsymbol{I}^{COM}(\boldsymbol{r})\}(\boldsymbol{k})}{2\pi i \boldsymbol{k}^2} \qquad 4.3$$

Combining Equations 4.1 and 4.3 we also find that the integrated signal is linearly proportional to the electromagnetic potential convolved with the probes function

$$\boldsymbol{I}^{iCOM}(\boldsymbol{r}) = \frac{1}{2\pi}(|\psi_0|^2 \otimes \Phi)(r)$$

Effectively what Equation 4.1 describes is the deflection of the BF disc's COM as the electron probe passes over the positive potential of an atomic nucleus and scatters onto the opposing detector. Using a quadrant detector the divergence in Equation 4.2 is broken into

$$I_x^{COM}(x,y) = \frac{\partial \Phi(x,y)}{dx}$$
$$I_y^{COM}(x,y) = \frac{\partial \Phi(x,y)}{dy}$$

with $I_i(x,y)$ being the difference in intensity of opposite detector segments. The integrated version of the COM using a segmented detector is referred to as integrated DPC (iDPC). With the linearity of iDPC with the electromagnetic potential, iDPC-STEM is now capable of imaging all elements of the periodic table including hydrogen (de Graaf et al., 2020). In this thesis work this extreme of sensitivity is not required but the high signal-to-noise and interpretability of iDPC signal allows for high-quality quantification of the oxygen sublattice in perovskites in relation to the cation sublattice. This technique will be used in Sections 9.1 and 9.2.

5 Inelastic Scattering

When an electron transitions through a specimen in a TEM it both elastically and inelastically scatters. Inelastic scattering in general is accompanied by an energy-loss of the incident electron from exciting the material. These excitations range from promoting an inner-shell electron to an unoccupied state (known as an inner-shell or core-loss excitation) to excitation of collective phenomena in a material (e.g. phonons, plasmons, exitons, etc.). The capability of EELS in a (S)TEM to locally analyze these excitation events provides a means to study local electronic and phononic properties and correlate these properties with the materials lattice or microstructure. To provide background for analysis of local electronic structure in SLs with different periods we will begin in Section 5.1 by discussing the underlying theory for excitation of inner-shell electrons. This will then be extended to cover electron energy-loss near-edge fine structure (ELNES) which provides information on local coordination and valence state. Features of Ti-$L_{2,3}$ and O-K core-loss edges will then be discussed as they pertain to both STO and CTO. Theory for collective excitations is more complex as it involves a many body system. In collective excitations characterized by a net dipole moment the theory for inelastic scattering can be simplified by using an effective dielectric formalism or dipole scattering. Dipole scattering will be discussed in Section 5.2 in the context of vibrational EELS.

5.1 Atomic Model for Core-loss Electron Energy-Loss Spectroscopy

To consider the inelastic scattering of an electron by an atom we need to consider the energy-loss of the incident electron from exciting inner-shell electrons in state α to unoccupied final state β and the change in momentum of the incident electron from $\hbar\boldsymbol{k}_0$ to $\hbar\boldsymbol{k}$. The Schrödinger Equation for this two-electron system is

$$H|\boldsymbol{k}_0, \alpha\rangle = (E_0 + E_\alpha)|\boldsymbol{k}_0, \alpha\rangle \qquad 5.1$$

where *H* is the Hamiltonian and E_0 and E_α are the energy of the incident and inner-shell electrons initial state, respectively. Inelastic scattering requires $|\boldsymbol{k}| \neq |\boldsymbol{k}_0|$ and $\alpha \neq \beta$. To begin we will start with two well separated non-interacting electrons then two interacting electrons (Fultz & Howe, 2013).

Beginning with two well separated electrons simplifies the systems total energy to an unperturbed Hamiltonian $H = H_0$ with H_0 given by

$$H_0 = -\frac{\hbar^2}{2m_e}(\nabla_1^2 + \nabla_2^2) + V(\boldsymbol{r}_2) \qquad 5.2$$

where ∇_i^2 is the Laplacian for the incident electron (i=1) and inner-shell electron (i=2) and $V(\boldsymbol{r}_2)$ is the potential associated with electron 2 at position $\boldsymbol{r}_2$. The first term is a linear combination of the incident and inner-shell electron kinetic energies, and the second term is the potential energy associated with the inner-shell electron interacting with other atomic electrons and the nuclei. Because the electrons are non-interacting the initial and final states are independent of the other electron and are expressed as products $|\boldsymbol{k}_0, \alpha\rangle = |\boldsymbol{k}_0\rangle|\alpha\rangle$ and $|\boldsymbol{k}, \beta\rangle = |\boldsymbol{k}\rangle|\beta\rangle$. $\nabla_1^2|\beta\rangle$, $\nabla_2^2|\boldsymbol{k}\rangle$, and $V(\boldsymbol{r}_2)|\boldsymbol{k}\rangle$ are constants resulting in independence of wavefunctions for the two electrons, thus describing no interaction and no transitions.

When the electrons are closer at a distance $\boldsymbol{r} = \boldsymbol{r}_1 - \boldsymbol{r}_2$, such that they interact, the two-electron system is described by a perturbation Hamiltonian

$$H' = \frac{e^2}{|\boldsymbol{R}|} + V(\boldsymbol{r}_1) \qquad 5.3$$

where $\boldsymbol{R} = \boldsymbol{r}_1 - \boldsymbol{r}_2$ is the separation of the incident electron (i=1) and inner-shell electron (i=2) and $V(\boldsymbol{r}_1)$ is the potential from the rest of the atom. The solution to Equation 5.1 with the Hamiltonian in Equation 5.3 is the product of a spherical wave and an inelastic form factor

$$f_{in}(\boldsymbol{q}) = -\frac{m_e}{2\pi\hbar^2}\langle\beta|\langle\boldsymbol{k}|H'|\boldsymbol{k}_0\rangle|\alpha\rangle \qquad 5.4$$

where $\boldsymbol{q}=\boldsymbol{k}-\boldsymbol{k}_0$. Substituting Equation 5.3 into Equation 5.4 and noting that $\boldsymbol{r}_1$ only appear in $|\boldsymbol{k}\rangle$, $|\boldsymbol{k}_0\rangle$, and $V(\boldsymbol{r}_1)$ while $\boldsymbol{r}_2$ only appears in $|\alpha\rangle$ and $|\beta\rangle$ provides

$$f_{in}(\boldsymbol{q}) = -\frac{m_e}{2\pi\hbar^2}\begin{pmatrix} e^2\left\langle\beta\middle|\left\langle\boldsymbol{k}\middle|\frac{1}{|\boldsymbol{R}|}\middle|\boldsymbol{k}_0\right\rangle\middle|\alpha\right\rangle \\ +\langle\alpha|\beta\rangle\langle\boldsymbol{k}|V(\boldsymbol{r}_1)|\boldsymbol{k}_0\rangle \end{pmatrix} \qquad 5.5$$

Because the atomic wave function is orthogonal the term $\langle\alpha|\beta\rangle = 0$ in Equation 5.5 and only the coulombic interaction of the incident electron with the inter-shell electron remains. Note that the orthogonality is not always true, for example, when a core hole is present for example, but the orthogonality is generally a valid approximation. Representing the incident electron's waves through a Fourier transform f_{in} can be represented in real space as

$$f_{in}(\boldsymbol{q}) = -\frac{m_e e^2}{2\pi\hbar^2}\iint \frac{e^{-i\boldsymbol{k}\cdot\boldsymbol{r}_1}e^{-i\boldsymbol{k}_0\cdot\boldsymbol{r}_1}}{|\boldsymbol{R}|}\psi_\beta^*\psi_\alpha d^3\boldsymbol{r}_2 d^3\boldsymbol{r}_1$$

and framed with respect to the inner-shell electron by substituting $\boldsymbol{r}_1 = \boldsymbol{r} + \boldsymbol{r}_2$ and $\boldsymbol{q}=\boldsymbol{k}-\boldsymbol{k}_0$,

$$f_{in}(\boldsymbol{q}) = -\frac{m_e e^2}{2\pi\hbar^2}\int \frac{e^{-i\boldsymbol{q}\cdot\boldsymbol{R}}}{|\boldsymbol{R}|}d^3\boldsymbol{R}\int e^{-i\boldsymbol{q}\cdot\boldsymbol{r}_2}\psi_\beta^*\psi_\alpha d^3\boldsymbol{r}_2 \qquad 5.6$$

To simplify the readability of the Equations we will substitute in the Bohr radius $a_0 = \hbar^2/m_e e^2$. The first integral in Equation 5.6 describes the spatial interaction of the two electrons as the volume of a spherical wave $(4\pi/\boldsymbol{q}^2)$. The second integral describes the transition probability from state α to β resulting from a transferred momentum $\hbar\boldsymbol{q}$. Scattering probability per unit angle is described by the differential cross-Section (DCS)

$$\frac{d\sigma}{d\Omega} = f^*f$$

in terms of a solid angle increment $d\Omega = 2\pi\frac{\boldsymbol{q}}{k^2}d\boldsymbol{q}$ providing an inelastic DCS as

$$\frac{d\sigma}{d\Omega} = \frac{4}{a_0^2\boldsymbol{q}^4}\left|\left|\int e^{-i\boldsymbol{q}\cdot\boldsymbol{r}_2}\psi_\beta^*\psi_\alpha d^3\boldsymbol{r}_2\right|^2\right. \qquad 5.7a$$

or

$$\frac{d\sigma}{d\boldsymbol{q}} = \frac{8\pi}{a_0^2k^2\boldsymbol{q}^3}\left|\left|\int e^{-i\boldsymbol{q}\cdot\boldsymbol{r}_2}\psi_\beta^*\psi_\alpha d^3\boldsymbol{r}_2\right|^2\right. \qquad 5.7b$$

which encompasses the joint probability of scattering from state α to β. In literature the bracketed term is known as the *dynamical structure factor* or *transition matrix element*. The scattering properties of Equation 5.7b are isolated and multiplied by the difference in energy of the two states ($E_{\alpha\beta} = E_\beta - E_\alpha$) to define a generalized oscillator strength

$$G_{\alpha\beta}(\boldsymbol{q}) \equiv \frac{2m_e}{\hbar^2\boldsymbol{q}^2}E_{\alpha\beta}\left|\left|\int e^{-i\boldsymbol{q}\cdot\boldsymbol{r}_2}\psi_\beta^*\psi_\alpha d^3\boldsymbol{r}_2\right|^2\right. \qquad 5.8$$

with the pre-factor $\frac{2m_e}{\hbar^2\boldsymbol{q}^2} = \frac{1}{E}$ being the inverse energy-loss of the incident electron, $E = E_0 - E_f$ where E_f is the final energy not to be mistaken with Fermi energy. Note that energy is conserved because $E_0 + E_\alpha = E_f + E_\beta$ and therefore the energy-loss $E = E_0 - E_f = E_\alpha - E_\beta = E_{\alpha\beta}$ both defines and restricts the energy lost by the electron. $G_{\alpha\beta}$ emphasizes that the inelastic excitation seen in EELS is proportional to i) the energy difference between states relative to the change energy transferred by the incident electron and ii) the transition probability between occupied and unoccupied states!

To incorporate the continuous nature of the unoccupied states in a material and the number of states per energy we consider the unoccupied density of states, $N(E) = d\beta/dE$. This is accounted for by multiplying Equation 5.7 by $N(E)dE$. This multiplication and the substitution of Equation 5.8 gives

$$\frac{d\sigma}{d\boldsymbol{q}} = \frac{4\pi\hbar^2}{a_0^2 k^2 m_e}\frac{1}{\boldsymbol{q}}\frac{N(E)}{E_{\alpha\beta}}G_{\alpha\beta}(\boldsymbol{q}) \qquad 5.9$$

The k dependence of Equation 5.9 can be removed, and relativistic effects of the fast electron accounted for, by multiplying by $\frac{E_0}{T} \approx \frac{E_f}{T} = \frac{\hbar^2 k^2}{2m_e}\frac{1}{T}$ where

$$T = \frac{E_0}{2}\frac{1+\gamma_{vac}}{\gamma_{vac}^2}$$

is the relativistic kinetic energy of the incident electron,

$$\gamma_{vac} = \frac{1}{\sqrt{1-(v/c)^2}}$$

is the Lorentz contraction factor of special relativity accounting for the electrons velocity relative to light in vacuum, and the approximation $E_0 \approx E_f$ is valid since the energy-loss is $\sim 10^{-3}$ smaller than the initial energy. Equation 5.9 is thus

$$\frac{d\sigma^2}{d\boldsymbol{q}dE} = \frac{2\pi\hbar^4}{a_0^2 m_e^2 T}\frac{1}{\boldsymbol{q}}\frac{N(E)}{E_{\alpha\beta}}G_{\alpha\beta}(\boldsymbol{q}) \qquad 5.10$$

Equation 5.10 provides a local momentum-resolved density of states interpretation for EELS and expresses i) the local momentum dependence of scattering through $\frac{1}{\boldsymbol{q}}G_{\alpha\beta}(\boldsymbol{q})$, ii) the shape and energy of the edge through $G_{\alpha\beta}(\boldsymbol{q})$, and iii) the shape of the edge resulting from local chemical effects through $N(E)$. What this allows for is a local probing of the electronic state in a material including effects from local coordination and chemical bonding. This will be used in analyzing the evolution of electronic structure as the period size changes in STO-CTO SLs.

The local momentum-resolved density of states interpretation for EELS aids in understanding modulations within ~40 eV of the core-loss edge known as electron energy-loss near-edge fine structure (ELNES). To illustrate we will first consider the L_2 and L_3 edge (often collectively referred to as the $L_{2,3}$ edge). The L_2 edge is a result of $2p_{1/2}$→$3d$ transitions and the L_3 edges from $2p_{3/2}$→$3d$ transitions. When examining the $L_{2,3}$ spectra from metals, like Ti, there are often four peaks rather than two. This is a result of crystal field effects splitting the d-orbital into multiple bands and therefore peaks, discussed in Section 1.1. For example, a six-fold coordinated octahedral site would have e_g and t_{tg} d-orbitals and the $L_{2,3}$ edge would have L_3-t_{tg}, L_3-e_g, L_2-t_{tg}, and L_2-e_g peaks known as white lines which correspond to $2p_{1/2}$→$3d$-t_{tg}, $2p_{1/2}$→$3d$-e_g, $2p_{3/2}$→$3d$-t_{tg}, and $2p_{3/2}$→$3d$-e_g transitions, respectively. Ratioing the peaks within the L_2 or

L_3 edge provides the relative ratio of occupancy in the two sub bands. For octahedral coordination, the high-energy t_{2g} has three orbitals and the low-energy e_g band has two orbitals, whereas for tetrahedral coordination the high energy e_g band has two orbitals and the low-energy t_g band has three orbitals. The white line ratio method provides a good sense of CN. Alternatively, probing the occupancy (or lack of occupancy) of the *d*-orbitals is akin to determining oxidation state. This has been employed in many oxides with multivalent Ti, such as STO, Nb:$BaTiO_3$, and $La_{1-x}Sr_xTiO_3$ (Klie et al., 2003, 2009; Nord et al., 2016; Ohtomo et al., 2002; Shao et al., 2016). It is also worth noting that ELNES provide the same information as x-ray absorption near-edge fine-structure (XANES) but with higher spatial resolution. A comparative study of EELS and x-ray absorption was used to characterize the conduction band of CTO (Ueda et al., 1998). One particularly relevant XANES example is a study performed by Cao et al. of STO and CTO on an NGO substrate (Cao et al., 2016). They found that the tetragonal distortion of TiO_6 octahedra resulted in degenerate Ti3*d*-t_{2g} orbitals splitting into d_{xy}/d_{yz} and d_{xy} bands and degenerate Ti3*d*-e_g splitting into $d_{x^2-y^2}$ and d_{z^2} bands. This is the transition from octahedral coordination to square-planar shown in Figure 1.1. In addition to occupancy, the crystal field splitting of orbitals can be directly measured from peak separation, therefore also provides information on local symmetry. Cations chemical and physical environments can therefore be determined locally using ELNES.

Table 5.1. Energy ranges for different bonding with O2*p*-orbitals present in the O-K edge of STO (from (de Groot et al., 1993; Tomita et al., 2017)) and the predict energy range in ELNES.

Bonding	DFT	EELS O-K (DFT + 532)
Ti3*d*-t_{2g}	0 - 4.5	532 - 536.5
Ti3*d*-e_g	4.5 - 8	536.5 - 540
Sr5*s* or Sr4*d*-e	8 - 12	540 - 544
Sr5*p* or Sr4*d*-t_2	15 - 20	547 - 552
Ti4*sp*	21 - 23	553 - 555

So far, *d*-orbitals were specifically addressed, but a rich near-edge fine structure is also found for the O-K edge of oxides. The most pertinent example is the O-K edge of STO and CTO (de Groot et al., 1993; Tomita et al., 2017, 2017; Wu et al., 2001). As discussed in Section 1.1, O atoms in perovskite oxides bond to both A- and B-site atoms and their local coordination changes with the structural distortions of the crystal. Table 5.1 shows the energy range of different O2*p* bonds formed in STO (de Groot et al., 1993). These energies are typical for all perovskites with shifts and intensity changes resulting from different bonding or other physical phenomena such as core holes (to be discussed later). For example, O2*p*-Ti4*sp* bonds in CTO are typically at energies >557 eV. Oxygen coordination and bonding can therefore be determined locally using ELNES.

Caution should be used when interpreting ELNES using a density of state and molecular orbital theory approach in ionic materials because the excitation of the inner-shell electron from its ground state leaves behind a locally charged region which attracts orbitals, known as a core hole

(Egerton, 2011; Leapman et al., 1982). The local charge region which attracts orbitals distorts the ground state structure and lowers binding energies (Egerton, 2011). This predominantly effects cations but in ionic materials where d-e$_g$ orbitals overlap oxygen orbitals the anion edges may also be impacted. If one looks to be quantitative, core hole effect can be included in density functional calculation using a Z+1 (Z being atomic number) substitution or by directly comparing spectra with standards (Rez & Muller, 2008). The capability of ELNES to observe similar changes in electronic structure lends it to local probing in structures such as SLs.

In this Section the EELS density of states interpretation was first developed which emphasized the capability for local probing of electronic structure in a material including effects from local coordination and chemical bonding. Specific examples of d-orbital crystal field effects in L$_{2,3}$ ELNES and bonding with O2p orbitals was presented. This allows for interpretation of near-edge fine structure in terms of local coordination and oxidation state and the ability to understand bonding with high spatial resolution in heterostructures such as SLs.

5.2 Dipole Approximation

In the dipole approximation, the energy lost ($E = \hbar\omega$) by the incident electron is equivalent to the work done on the electron ($-W$) by an induce field (Egerton, 2011; Forstmann et al., 1991; Garcia-Molina et al., 1985; Konečná, 2019; Ritchie, 1957; Z. L. Wang, 1996). Consequently, the loss per pathlength of electron traveling along $\hat{z}$ is given by the stopping power,

$$S = -\frac{dW}{dz} \qquad 5.11$$

i.e. the backward acting force. An electron traveling with velocity ($\boldsymbol{v}$) feels a Lorentz force

$$\boldsymbol{F} = -e(\boldsymbol{E} + \boldsymbol{v} \times \boldsymbol{B})$$

where $\boldsymbol{B}$ is the magnetic field. Since the magnetic component of $\boldsymbol{F}$ is perpendicular to $\boldsymbol{v}$ it does not contribute to S. For an electron traveling with $\boldsymbol{v} = v\hat{z}$ only the z-component of the electric field contributes providing,

$$S = eE_z \qquad 5.12$$

To consider the energy-loss due to an excitation, it is helpful to relate the energy loss from the excitation to the probability of the excitation per path length traveled and per unit energy. This probability is given by the inelastic differential scattering cross-Section (DCS, $\Gamma = \frac{d\sigma_i}{d\omega}$) which is related to S by,

$$S = \int_0^\infty \Gamma(\omega)\, \hbar\omega\, d\omega \qquad 5.13$$

Relating Equation 5.12 to 5.13 the double differential scattering cross-Section is found to be,

$$\int_0^\infty \Gamma\, \hbar\omega\, d\omega = eE_z \qquad 5.14$$

Thus, the scattering probability per energy is found by finding the z-component of the induced electric field. For interfaces, the DCS is referred to as a differential probability rather than cross-Section. For this document σ and probability, and their derivatives, are used interchangeably.

Excitations in a material often have a characteristic E as a function of scattering wave vector ($\boldsymbol{q}$), known as a dispersion. The momentum transfer associated with $\boldsymbol{q}$ is $\hbar\boldsymbol{q}$, and since the two are proportional by a constant will be used synonymously. It is sometimes helpful and informative to examine the dispersion and therefore the double differential cross Section per momenta (DDCS, $\frac{d^2\sigma}{d\omega dq}$). In conventional EELS an entrance aperture (EA) is used to limit $\boldsymbol{q}$ entering the spectrometer such that

$$\Gamma = \int_0^{q_{EA}} \frac{d^2\sigma}{d\omega dq} dq$$

where q_{EA} is the maximum $\boldsymbol{q}$ accepted by the EA and often set to the critical value (q_c) describing the limit of dipole scattering.

In the case of momentum-resolved EELS ($\boldsymbol{q}$-EELS) the full DDCS can be collected instantaneously using a slit aperture ($\boldsymbol{q}$-slit). A $\boldsymbol{q}$-slit is fixed aperture with length perpendicular to the dispersion direction of the spectrometer. The $\boldsymbol{q}$-slit therefore provides a means to selects a continuous momentum transfer perpendicular ($\boldsymbol{q}_\perp$) to the electron beam. The $\boldsymbol{q}$-slit has a finite width (1mm), however this width is often neglected since it is small and in the dispersion direction. Since the $\boldsymbol{q}$-slit is fixed, the $\boldsymbol{q}$-space projected onto the aperture is rotated by rotating the sample (with a tilt-rotate holder) or using the projection system. Rotating the sample is more desirable since it maintains the microscopes optics at a fixed condition. As an alternative to using a $\boldsymbol{q}$-slit, discrete momentum transfers can be collected by projecting $\boldsymbol{q}$-space over a small spectrometer EA. This is done by either; 1) using the diffraction shift coils to displace the diffraction pattern, or 2) tilting the electron beam. This is the spectroscopic equivalent of displaced vs. axial darkfield (DF) imaging and therefore (1) will be referred to as DDF and (2) as DF. Each approach has advantages and disadvantages. When DDF is used, the incident electrons remain parallel to the optic axis and therefore the sampled $\boldsymbol{q}_\perp$is relatable to inhomogeneities in real space, whereas DF changes the relative orientation of the incident electrons with respect to real space. For example, the energy loss and $\boldsymbol{q}_\perp$ at an interface will vary if the initial trajectory of the probe is changed. (Paragraph is Irrelevant unless we do $\boldsymbol{q}$-EELS).

In this Section the dipole approximation for inelastic electron scattering was introduced. This is developed further in Section 6 and is the first step in understanding vibrational EELS results in Sections 11 and 12.

6 Electron as an Electromagnetic Wave

In this Section the electron will be treated as an EM wave traveling through an arbitrary sample with unknown geometry or defect structure. This will allow for generalized wave Equations that with appropriate bound conditions can provide E_z required for the EELS dipole approximation discussed in Section 5.2.

Maxwell's Equations describe the induced $\boldsymbol{E}$ and $\boldsymbol{B}$ in a material that results from current density ($\boldsymbol{J}$) and free charge (ρ);

$$\nabla \cdot \boldsymbol{D} = \rho \tag{6.1a}$$

$$\nabla \times \boldsymbol{H} - \frac{\partial}{\partial t}\boldsymbol{D} = \boldsymbol{J} \tag{6.1b}$$

$$\nabla \times \boldsymbol{E} + \frac{\partial}{\partial t}\boldsymbol{B} = 0 \tag{6.1c}$$

$$\nabla \cdot \boldsymbol{B} = 0 \tag{6.1d}$$

where $\boldsymbol{H} = \frac{1}{\mu}\boldsymbol{B}$ is magnetic induction. $\mu = \mu_0 \mu_r$ is permeability of the materials with μ_0 and μ_r being the free-space and relative permeabilities. The phase velocity of the field in a material is given by $v_p = \frac{c}{\sqrt{\mu_r \varepsilon_r}}$ with the speed of light $c = \frac{1}{\sqrt{\mu_0 \varepsilon_0}}$. Lastly, the continuity Equation dictates that $\frac{\partial}{\partial t}\rho + \nabla \cdot \boldsymbol{J} = 0$.

Combining Maxwell's Equations produces the wave Equations,

$$\left(\nabla^2 - \mu\varepsilon \frac{\partial^2}{\partial t^2}\right)\boldsymbol{E} = \nabla \frac{\rho}{\varepsilon} + \mu \frac{\partial}{\partial t}\boldsymbol{J}$$

$$\left(\nabla^2 - \mu\varepsilon \frac{\partial^2}{\partial t^2}\right)\boldsymbol{B} = -\mu \nabla \times \boldsymbol{J}$$

or more generally

$$\left(\nabla^2 - \frac{1}{v_p^2}\frac{\partial^2}{\partial t^2}\right)\boldsymbol{\psi} = \boldsymbol{\psi_{src}}(\boldsymbol{r}, t) \tag{6.2}$$

where $\boldsymbol{\psi}$ is a general wave (ie $\boldsymbol{E}$ or $\boldsymbol{B}$) and $\boldsymbol{\psi_{src}}(\boldsymbol{r}, t)$ is a driving term from the source. This is a partial second order inhomogeneous differential Equation and has a general solution,

$$\boldsymbol{\psi}(\boldsymbol{r}, t) = \boldsymbol{\psi}_H(\boldsymbol{r}, t) + \boldsymbol{\psi}_I(\boldsymbol{r}, t)$$

where subscripts H and I identify the homogeneous and inhomogeneous solutions. One homogeneous solution to Equation 6.2 is a spherical wave,

$$\boldsymbol{\psi}_H(\boldsymbol{r},t)=\frac{\boldsymbol{\psi}_{\mathbf{0}}}{\boldsymbol{q}}e^{i(\boldsymbol{q}\boldsymbol{r}-\omega t)}$$

We like to consider the field of an electron as a traveling spherical wave and in the limit of the detector being far from the electron we can approximate the spherical wave as a plane wave,

$$\boldsymbol{\psi}_H(\boldsymbol{r},t)=\boldsymbol{\psi}_{\mathbf{0}}e^{i(\boldsymbol{q}\boldsymbol{r}-\omega t)}$$

which is also a homogeneous solution to Equation 6.2[4]. If the system lacks a driving force the homogeneous form of Equation 6.1a and d results in $0=\nabla\cdot\boldsymbol{\psi}=i\boldsymbol{q}\cdot\boldsymbol{\psi}$ which is only satisfied when $\boldsymbol{q}\cdot\boldsymbol{\psi}_{\mathbf{0}}=0$. For example, the field from $\boldsymbol{\psi}$ traveling in the z-direction has the plane wave solution

$$\boldsymbol{\psi}(z,t)=\begin{pmatrix}\psi_x\\ \psi_y\\ 0\end{pmatrix}e^{i(q_z z-\omega t)}$$

In other words, without a source ***H₀*** and ***E₀*** must be perpendicular to ***q*** and is always a transverse wave. Photons fall into this category and are described as a transverse electromagnetic wave. Electrons however act as a source term and therefore have both transverse and longitudinal components. Equation 6.1d is always homogeneous and therefore this perpendicular nature always holds for ***B***. When the wave has a driving force Equation 6.1a provides a magnitude of ***E*** dictated by the divergence of ρ. If it is assumed that the general solution of Equation 6.2 is time harmonic, as are spherical and plane waves, then Equation 6.2 simplifies to the Helmholtz Equation

$$(\nabla^2+\alpha^2)\boldsymbol{\psi}=-\boldsymbol{\psi}_{\boldsymbol{src}}(\boldsymbol{r},\omega) \qquad 6.3a$$

$$\chi^2=\frac{\omega^2}{v_p^2}=k_c^2\varepsilon_r \qquad 6.3b$$

with the propagation constant α and free space wavevector of light $k_c=\frac{\omega}{c}$. For ***E*** and ***B***

$$(\nabla^2+\alpha^2)\boldsymbol{E}=\nabla\frac{\rho}{\varepsilon}-i\omega\mu\boldsymbol{J} \qquad 6.4a$$

$$(\nabla^2+\alpha^2)\boldsymbol{B}=-\mu\nabla\times\boldsymbol{J} \qquad 6.4b$$

It is important to remember that ***E*** and ***B*** are not decouple but rather relatable by Faraday's law of induction (Equation 6.1c). Plugging either the spherical or plane wave into the homogeneous version of Equation 6.3 provides the relation, $\alpha^2=\boldsymbol{q}^2$, between the propagation constant and wave-vector for a wave. The source terms complicate the solution of Equation 6.3a, but

---

[4] A plane wave traveling in $\boldsymbol{q}$ means that $\boldsymbol{\psi}$ normal to $\boldsymbol{q}$ is constant $\nabla\boldsymbol{\psi}_{\mathbf{0}}=0$.

simplifications can be made if the symmetry of the system is known. Two-dimensional symmetry will be presented in Section 6.1.

In an approximately infinite homogeneous material, the direct solution of Maxwell's Equations yields,

$$\boldsymbol{E} = \frac{ie}{\pi}\int \frac{\boldsymbol{q}/\varepsilon - k_c\beta}{q^2 - k_c^2\varepsilon} e^{i\boldsymbol{q}\cdot\boldsymbol{r}}\delta(\omega - \boldsymbol{q}\cdot\boldsymbol{v}) \qquad 6.5$$

where $\beta = \frac{\boldsymbol{v}}{c}$ is the relativistic velocity of the electron(García de Abajo, 2010). Equation 6.5 expresses three physical phenomena; i) energy conservation through the Dirac-delta term, ii) retardation effects through $k_c^2\varepsilon$, and iii) dispersion relation through the poles (zeroes of the denominator). The dispersion relation

$$q^2 = k_c^2\varepsilon \qquad 6.6$$

indicates the dispersion of light in a material. As $q \rightarrow k_c$ the excited modes couple to the electric filed becoming "light like" and are known as polaritons. When an electron travels faster than the speed of light in a material, i.e. with $q^2 > k_c^2\varepsilon$, then the electron will emit Cherenkov radiation(Egerton, 2011; García de Abajo, 2010; Garcia-Molina et al., 1985; Kliewer & Fuchs, 1966; Kröger, 1970). This is best seen when the integral in Equation 6.5 is solved,

$$\boldsymbol{E} = \frac{2e\omega}{v^2\gamma_\varepsilon\varepsilon} e^{i\frac{\omega}{v}z}\left[\frac{i}{\gamma_\varepsilon}K_0\left(\frac{k_c}{\gamma_\varepsilon}R\right)\hat{\boldsymbol{z}} - K_1\left(\frac{k_c}{\gamma_\varepsilon}R\right)\hat{\boldsymbol{R}}\right]$$
$$\gamma_\varepsilon = (1 - \varepsilon\beta^2)^{-0.5}$$

where γ_ε is the Lorentz contraction factor of special relativity describing the change in time, length, and mass for an object in motion, K_0 and K_1 are the first and second order modified Bessel functions, and here $\boldsymbol{R}$ represents the radial coordinate (not to be confused with $\boldsymbol{R}$ in diffraction). When the electron is faster than light $\varepsilon\beta^2 > 1$ such that γ_ε is imaginary. This attenuates K_0 and K_1 which is indicative of radiation. The radiation itself is not of concern in the presented study but it is important in vibrational EELS because it results in energy-loss like vibrational modes. Therefore, Cherenkov radiation peaks can be mistaken as a vibrational peak or mask vibrational peaks and need be considered. Excited phonon modes also have the potential to be radiative, this is another reason why relativity is important as it describes the observed excitations.

In this Section electrodynamic wave Equations were discussed in the context of an electron traveling through a material characterized by ε and μ. The induced field from an electron traversing a non-magnetic material only depends on ε and the geometry of the system (via Equation 6.4a). Therefore, the energy lost by the electron from a dipole resonance is calculated with Equation 5.14 if ε is known. Additionally, the polaritonic and radiative nature of vibrations in a material were described. This will appear again in the discussion of electrons traveling near interfaces.

6.1 Electron Traveling Parallel to Infinite Interface(s)

This Section will consider interface modes that are induced by an electron traveling parallel to interfaces. First, a single interface is considered, and the dispersion relation of an interface phonon is derived in addition to conditions for polaritonic and radiative vibrational modes. The DDCS in the relativistic and non-relativistic (NR) approximation are then considered which describes how the interface contributes to energy loss. The picture will then be broadened to two bounding interfaces that can couple which introduces additional modes with special symmetry. Lastly, an infinite SL is considered.

For an electron traveling with $\boldsymbol{v} = v\hat{z}$ and parallel to an interface with a normal $\hat{x}$, as shown in Figure 6.1, ρ is given by,

$$\rho(\boldsymbol{r}, z, t) = -e\delta(x-b)\delta(y)\delta(z-vt) \qquad 6.7$$

where the impact parameter b is the distance from the interface and $\boldsymbol{J} = \rho\boldsymbol{v}$.

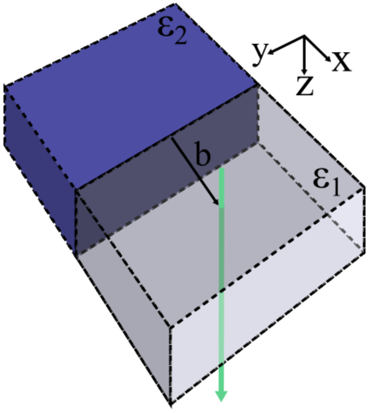

Figure 6.1. Schematic of a two-slab system with an interface normal to x and an electron traveling along z. The permittivity of the slabs is denoted by ε1 and ε2.

If the energy loss of the electron is assumed to be small, then the associated change in $\boldsymbol{v}$ is small and considered constant. The x, z, and t invariant symmetry of the wave is best represented after the three dimensional Fourier transform $\mathcal{F}_{\boldsymbol{r}_\parallel,t}[f(\boldsymbol{r}_\parallel,t)](\boldsymbol{q}_\parallel,\omega) = \int f(\boldsymbol{r}_\parallel,t)e^{i(\boldsymbol{q}_\parallel\cdot\boldsymbol{r}_\parallel-\omega t)}$ where $\boldsymbol{q}_\parallel$ and $\boldsymbol{r}_\parallel$ lie in the plane of the interface. This transforms Equation 6.7 into

$$\rho = -2\pi e\delta(x-x_0)\delta(vq_z-\omega) \qquad 6.8$$

[5] with the wave vector

$$q_z = \frac{\omega}{v} \qquad 6.9$$

and Equations 6.4a and b into,

---

[5] The Dirac delta function δ(t) has the property $\int \delta(vt-t_0)f(t) = \frac{1}{|v|}f(t_0)$. A Fourier transform $\mathcal{F}_t[f(t)](\omega) = \int f(t)e^{-i\omega t}$ of δ(t) is therefore $e^{-i\omega t_0}$. Also given that $\delta(at) = \frac{1}{|a|}\delta(t)$ then $\mathcal{F}_t[\delta(at-t_0)](\omega) = \frac{1}{|a|}e^{-i\omega\frac{t_0}{a}}$

$$\left(\nabla^2 - q_\parallel^2 + \frac{\omega^2}{v_p^2}\right)\boldsymbol{E} = \nabla\frac{\rho}{\varepsilon_j} + i\omega\mu\boldsymbol{J} \qquad 6.10$$

where ε_j is the relative permittivity of material *j*. The wave vector in the plane of the interface is

$$q_\parallel^2 = q_z^2 + q_y^2 \qquad 6.11$$

Plugging Equation 6.9 and 6.11 into the source less version of Equation 6.10, the momentum transferred perpendicular to the interface is given by,

$$\begin{aligned} q'^2_{\perp j} &= k_c^2\varepsilon_j - q_\parallel^2 \\ &= q_z^2\left(\beta^2\varepsilon_j - 1\right) - q_y^2 \end{aligned} \qquad 6.12$$

When χ' is real $\boldsymbol{E}$ is an oscillatory function and Cherenkov radiation is emitted. When $q'_\perp$ is imaginary $\boldsymbol{E}$ is purely real. For convenience, the imaginary component of $q'_\perp$ is factored out such that $q'_\perp = iq_\perp$ and

$$\begin{aligned} q^2_{\perp j} &= q_\parallel^2 - k_c^2\varepsilon_j \\ &= q_y^2 + q_z^2\left(1 - \beta^2\varepsilon_j\right) \end{aligned} \qquad 6.13$$

This imposes that $\boldsymbol{E}$ is purely real when $q_\perp$ is real. The parenthetical term describes the velocity of an electron relative to light in a material like γ_ε. The first thing to notice is that Equation 6.13 is always real when ε<0 and therefore radiative modes will not occur in a Reststrahlen band where SPh often exist. Equation 6.13 imposes for $q_\perp$ to be real that

$$1 \geq \beta^2\varepsilon_j \qquad 6.14a$$

$$q_\parallel^2 \geq k_c^2\varepsilon_j \qquad 6.14b$$

Equation 6.14a indicates that the velocity of an electron cannot exceed the speed of light in a material. It was already stated that the radiative condition is never satisfied for frequencies with ε<0, where interface modes often exist, Equations 6.14a and b further this remark. When ε>0, where bulk modes exist, the radiative condition depends on the magnitudes of β and ε_j. The equivalence condition in Equation 6.14b is the dispersion of light in a material, as shown in Equation 6.6. Equation 6.14b define the region of $\boldsymbol{q}$-space as $q_\parallel$ larger than the wavevector of light in the material, this condition is satisfied to the left of the "electron line", $\omega = q_\parallel v$. For illustration, the reader is referred to Figure 2.1(b). When the electron is moving faster than light in the material and has a smaller $q_\parallel$ (i.e. or in terms of energy, $q_\parallel v > q_\parallel \frac{c}{\sqrt{\varepsilon}}$) then the electron will emit Cherenkov radiation.

Within the sample there are six waves that need to be considered; 1) The induced waves from the electron, $\boldsymbol{E}_1$ and $\boldsymbol{B}_1$, 2) the waves that will reflect off the boundary, and 3) the waves transmitted through the boundary. Solving Equation 6.10 provides a solution to the induced wave. The amplitudes of the six waves are found by applying Gauss's law and the boundary conditions

$$\begin{aligned} \varepsilon_1 E_{1x}|_{x=0} &= \varepsilon_2 E_{2x}|_{x=0} \qquad & B_{1x}|_{x=0} &= B_{2x}|_{x=0} \\ E_{1y}\Big|_{x=0} &= E_{2y}\Big|_{x=0} \qquad & B_{1y}\Big|_{x=0} &= B_{2y}\Big|_{x=0} \\ E_{1z}|_{x=0} &= E_{2z}|_{z=0} \qquad & B_{1z}|_{x=0} &= B_{2z}|_{z=0} \end{aligned}$$

With the amplitudes and the full wave Equation we can consider; 1) the dispersion relation of interface and bulk modes, which tells us if they are polaritons and/or radiative, 2) the wavelength of the modes which can be important when considering thin samples, and 3) E_z which is required for the DDCS. These three topics are detailed below.

Forstmann et al. decomposed the amplitude of E_z into p- and s-polarization into reflection coefficients

$$r_p = \frac{q_{\perp 1}\varepsilon_2 - q_{\perp 2}\varepsilon_2}{q_{\perp 1}\varepsilon_2 + q_{\perp 2}\varepsilon_2} \tag{6.15a}$$

$$r_s = \frac{q_{\perp 1} - q_{\perp 2}}{q_{\perp 1} + q_{\perp 2}} \tag{6.15b}$$

(Forstmann et al., 1991; García de Abajo, 2010). The p-polarized component results from transverse magnetic (TM) waves and the s-polarized component from transverse electric waves (TE). The resonance associated with the reflection of the wave is the interface phonon (IPh) and signifies a collective oscillation of the atomic lattice at the interface. When either material is vacuum ($\varepsilon_1 = 1$ or $\varepsilon_2 = 1$) then Equation 6.16b describes a SPh. In literature IPh are often termed as SPh. Since SPh are a subclass of IPh and we are interested in both IPh and SPh we will use the distinguishable nomenclature. The denominator of Equation 6.15a signifies the dispersion of the p-polarized interface resonance and will be discussed later.

Equation 6.15a diverges when its denominator is zero signifying a resonance. Setting the denominator of Equation 6.15a to zero and solving for $q_\parallel$ provides the excitation dispersion. The denominator of the TM component in Equation 6.15a result in dispersions of

$$q_\parallel^{IPh} = k_c \sqrt{\frac{\varepsilon_1 \varepsilon_2}{\varepsilon_1 + \varepsilon_2}} \tag{6.16a}$$

for the IPh. In a similar manner the Ph dispersion

$$q_\parallel^{Ph} = k_c \sqrt{\varepsilon_1} \tag{6.16b}$$

is obtained from the divergence of the electric field in a homogeneous medium. An example of the dispersions in Equation 6.16 are shown in Figure 2.1 for hexagonal BN. Note that when damping is included in the permittivity then the IPh (or SPh) dispersion will diverge instead of crossing the light-line. Because of scale this is not noticeable in Figure 2.1. The dispersion relation in 6.16b can also be derived directly from the continuity of ***D*** boundary condition, imposed by Maxwell’s Equations, combined with the propagation wave vector, Equation 6.12

(Raether, 1988). Equations 6.13 and 6.16 also provides the perpendicular component of the wave vector as

$$q_{\perp j}^{IPh} = k_c \sqrt{-\frac{\varepsilon_j^2}{\varepsilon_1 + \varepsilon_2}} \qquad 6.17$$

For Equations 6.16a to be real $\varepsilon_1\varepsilon_2$ and $\varepsilon_1 + \varepsilon_2$ have to have the same sign. For Equation 6.17 to be real $\varepsilon_1 + \varepsilon_2$ must be negative. Given the two sets of conditions, non-radiative IPh exist when both $\varepsilon_1\varepsilon_2 < 0$ and $\varepsilon_1 + \varepsilon_2 < 0$ while radiative IPh exist when $\varepsilon_1\varepsilon_2 > 0$ and $\varepsilon_1 + \varepsilon_2 > 0$. An electron will only excite modes with $q_{\parallel} \geq \frac{\omega}{v}$, according to energy conservation, and therefore higher velocity electrons (high keV) excite smaller $q_{\parallel}^{IPh}$ and $q_{\parallel}^{Ph}$. The group velocity (v_g) relative to the *c* is considered to distinguish between polaritonic and non-polaritonic modes. In the limit $q_{\parallel} \rightarrow \infty$ the group and phase velocity of the longitudinal SPh approach zero indicating a localized non-propagating excitation. In plasmonics this is the Ritchie surface plasmon (ω_{SP}) and for phononics this is TO ω_{SPh}. The same $v_g = \infty$ limit is found for transverse IPh and as $q_{\parallel} \rightarrow 0$, these are the LO ω_{SPh}. The third limit is when $q_{\parallel}^{IPh} \rightarrow k_c$ (i.e. approaching the "light line"), where v_g of the excitation approaches *c* and the collective behavior hybridizes with propagating EM waves. The hybridization and "light-like" character is known as a polaritonic IPh (IPhP). The IPh(P) to the right of the "light line" are non-radiative (Kliewer & Fuchs, 1967; Kretschmann & Raether, 1968; Ritchie, 1957). The hybridization results in modes with ranging $\boldsymbol{q}$ and ω, as found in Equation 6.16a and b.

The resulting E_z along with Equation 5.14 results in a relativistic DDCS which has been solved by prior authors (Forstmann et al., 1991; Garcia-Molina et al., 1985; Konečná, 2019; Konečná et al., 2018; Moreau et al., 1997; Z. L. Wang, 1996). The DDCS is

$$\frac{d^2\sigma}{dEdq_y} = \frac{e^2}{2\pi v^2 \varepsilon_0}\left(f_{bulk} + f_{beg} + f_{int}\right) \qquad 6.18a$$

$$f_{bulk} = \Im\left\{-\frac{1 - \varepsilon_1\beta^2}{\varepsilon_1 q_{\perp 1}}\right\} \qquad 6.18b$$

$$f_{beg} = \Im\left\{\frac{1 - \varepsilon_1\beta^2}{\varepsilon_1 q_{\perp 1}} e_1^{-2q_{\perp 1}b}\right\} \qquad 6.18c$$

$$f_{int} = \Im\left\{e_1^{-2\chi_1 b}\left(-\frac{2}{\varepsilon_1 q_{\perp 2} + \varepsilon_2 q_{\perp 1}} + \frac{2}{q_{\perp 1} + q_{\perp 2}}\right)\right\} \qquad 6.18d$$

where f_{bulk}, f_{beg}, and f_{int} are the bulk, *begrenzungs* and interface energy loss functions, respectively. The subscript 1 indicates the material the electron is moving through and subscript 2 is the material on the other side of the interface. The bulk term is identical to the energy loss function in the absence of an interface and includes retardation effects through both the numerator and χ. The bulk dispersion relation, Equation 6.16b, is also a pole (i.e. when the denominator is zero). In Equation 6.18c and d the exponent term describes the strength of interaction with interface relative to the probe position. Apart from the exponential term, Equation 6.18b and c are equal and opposite. This is interpreted as a reduction in probability of bulk excitation as the probe approaches the interface which is necessary to allow for a probability of interface excitation. This phenomenon is known as the *begrenzungs* (boundary) effect. Equation 6.18d is the energy loss function that results in loss from the reflected wave and includes the effect of Cherenkov radiation on the wave. The first and second term in parenthesis are from the electrons *p*-polarized TM and *s*-polarized TE fields that interact with the interface, respectively. The IPh dispersion relations, Equation 6.16a, are also poles in this loss function. The TM is typically one to two orders of magnitude larger than the TE component so will contribute relatively little to the total energy loss of the electron. The interface loss is therefore considered primarily TM in character. The TE component cannot however be ignored and becomes important when radiative modes become prevalent. An important feature to note is that if the electron is in vacuum ($\varepsilon_1 = 1$) near a material then the bulk and *begrenzungs* losses (Equation 6.18b and c) will be zero but the loss from the interface (Equation 6.18d) will still exist. This geometry is known as aloof spectroscopy. Aloof spectroscopy is gaining popularity and has large impacts in fields studying radiation sensitive materials since the sample is never directly exposed to the electron beams.

The non-polaritonic case of Equation 6.16, where v_g diverges from c, is best examined by taking the limit of $c \to \infty$ (and therefore $\beta \to \infty$ and $q_{\perp j} = q_{\parallel}$). This is known as the NR approximation since all propagating waves travel slower than c and are non-radiative.

$$\frac{d^2\sigma^{NR}}{dEdq_y} = \frac{e^2}{2\pi v^2 \varepsilon_0}\frac{1}{q_{\parallel}}\left(f_{bulk}^{NR} + f_{beg}^{NR} + f_{int}^{NR}\right) \tag{6.19a}$$

$$f_{bulk}^{NR} = \Im\left\{-\frac{1}{\varepsilon_1}\right\} \tag{6.19b}$$

$$f_{beg} = e^{-2q_{\parallel}b}\Im\left\{\frac{1}{\varepsilon_1}\right\} \tag{6.19c}$$

$$f_{int} = e^{-2q_{\parallel}b}\Im\left\{-\frac{2}{\varepsilon_1 + \varepsilon_2}\right\} \tag{6.19d}$$

The poles of Equation 6.19b-d (ie their divergence) are purely dependent on ε_j and lack dispersion. These poles signify collective resonances without a characteristic ***q*** (i.e. non-polaritonic). Although the NR approximation does not capture all losses that might be present, it does allow for a closed form solution of the DCS,

$$\Gamma^{NR} = \frac{e^2}{2\pi v^2 \varepsilon_0}\left(\Gamma_{bulk}^{NR} + \Gamma_{beg}^{NR} + \Gamma_{int}^{NR}\right) \tag{6.20a}$$

$$\Gamma_{bulk}^{NR} = \ln\left(2q_c\frac{\hbar v}{E}\right)\Im\left\{-\frac{1}{\varepsilon_1}\right\} \tag{6.20b}$$

$$\Gamma_{beg}^{NR} = \mathrm{K}_0\left(2b\frac{E}{\hbar v}\right)\Im\left\{\frac{1}{\varepsilon_1}\right\} \tag{6.20c}$$

$$\Gamma_{int}^{NR} = \mathrm{K}_0\left(2b\frac{E}{\hbar v}\right)\Im\left\{-\frac{2}{\varepsilon_1 + \varepsilon_2}\right\} \tag{6.20d}$$

where q_c is the critical angle of dipole scattering or the angle of the spectrometer entrance aperture, and K_0 is the zero-order modified Bessel function of the second kind. The closed form solution of Γ^{NR} describes that the probability of energy loss from a Ph depends on the area of ***q*-**

space sampled and in the presence of a boundary decreases as a function of $b\omega/v$. The Γ_{int}^{NR} component describes an energy loss from an IPh is only dependent on its proximity to the interface and the average of the bounding permittivities. For both the interface and bulk losses, the peak position determined by $\Im\{\ldots\}$ which is independent of $\boldsymbol{q}$.

The wavelength associated with Equations 6.16 and 6.17 are given by their reciprocals ($\lambda_{\parallel/\perp} = 2\pi/\boldsymbol{q}_{\parallel/\perp}$). For the example of h-BN the SPhP wavelengths for a 60 keV electron are $\lambda_{\parallel} = 2.99$ and $\lambda_{\perp} = 1.94$ µm. These wavelengths are not the spatial extent or delocalization of the field. The delocalization of the field is better measured by the exponential damping of the electric field provided by the imaginary component of $\boldsymbol{q}_{\parallel/\perp}$. The decay length is typically considered where the exponential decay reaches 1/e, i.e. the imaginary component of the exponential function's argument is 1. For h-BN the 1/e decay lengths are 21.04 and 365.75 µm for the parallel and perpendicular directions, respectively. The exponential decay of the electric field perpendicular to an interface is also found in Equations 6.18c and d[6]. Within the NR approximation at q_y=0 $q_{\perp j} = \frac{\omega}{v}$. This factor is found in the exponent in the DDCS and K_0 in the DCS, serving as the same measure of spatial delocalization. Setting the same 1/e criteria the delocalization is found as $b = \frac{\omega}{v}$. An interesting consequence of this delocalization is that an electron traveling in vacuum near a material can still characterize the vibrational response of the material.

Another consequence of the delocalization is that when two interfaces are close to one another they can interact. In the simplest case of two interfaces, the interfacial waves can couple in-phase and out of phase which are known as symmetric (IPh^+) and asymmetric (IPh^-) interface modes (Chen et al., 2005; Egerton, 2011; Raether, 1988). For large $q_{\parallel}$ (i.e. $q_{\parallel} = q_{\perp j}$) the dispersions are given by,

$$\frac{\varepsilon_2 + \varepsilon_1}{\varepsilon_2 - \varepsilon_1} = \pm e^{-q_{\parallel} t}$$

where t is the thickness of the film. An example of SPh coupling is shown in Figure 2.1(b) for a 200 nm film of h-BN. The coupling of the interface is most pronounced when $q_{\parallel} t \ll 1$ and degenerates to the SPh when $q_{\parallel} t > 1$.

As the number of interfaces increases the number of coupled configurations increases. For N number of interfaces this creates N number of configurations. For example, a single film bound by vacuum would have two interfaces, one SPh^+ and one SPh^-, where a superlattice with seven layers would have six interfaces, three IPh^+, and three IPh^-. Examples of coupling for SPh are found in references (Colvard et al., 1985; Gleize et al., 1999; Hessmer et al., 1992; Jusserand et al., 1984) and references (Albuquerque & Cottam, 1993; Bolton & Chen, 1995; Neyer et al., 1997) for surface plasmons, which obey similar physics in the dipole approximation. As with any lattice, as the number of layers/interfaces becomes increasingly large the dispersions merge into a singular band that spans a range of energy for a given $\boldsymbol{q}$ (Albuquerque & Cottam, 1993;

---

[6] The ***E*** exponential is given as $e^{-q_{\perp} x}$ where the exponent in the DDSC is given as $e^{-2q_{\perp} x}$. The factor of two difference in the exponential's argument is because the DDSC is a probability (or intensity) where ***E*** is a field.

Colvard et al., 1985; Gleize et al., 1999; Jusserand et al., 1984). When this occurs, the response is characterized by a single broad peak rather than many "sub" peaks. Herein these peaks will be referred to as SLPh.

In Section 6, the concept of an electron as an EM wave was introduced, which is necessary for calculating E_z and therefore the energy loss of an electron from dipole excitations, as described in Section 5.2. Then in Section 6.1 the boundary conditions for an interface were introduced which lead to i) the dispersion relation of IPh, ii) the concept of delocalization and its relation to the electric field's damping, iii) differentiation between (non)polaratonic modes and (non)radiative modes, iv) relativistic DDCS factored into f_{bulk}, f_{begr}, and f_{inter} which explaneed the probability of inelastic scattering as a function of E, $\boldsymbol{q}$, and b, v) the NR DCS which provided a $\boldsymbol{q}$ independent energy for IPh and Ph, and the relative intensity of scattering depending on the collection of $\boldsymbol{q}$-space. The idea of coupled interfaces modes, IPh$^+$ and IPh$^-$, in a thin film was then introduced which led to a discussion of SL thin films, which exhibit the same number of coupled modes as the number of interfaces. In the limit of an infinite lattice the IPh$^+$ and IPh$^-$ becomes bands termed SLPh$^+$ and SLPh$^-$.

7 Sample Description

Symmetric CTO-STO superlattice samples provided by Prof. R. Ramesh were grown on a (001)$_{pc}$-oriented NdGaO$_3$ substrate using pulsed laser deposition until the film thickness was 200 nm, further detail is found in reference (Ravichandran et al., 2014). Cross-Sectional SL specimens were prepared using a Helios dual-beam focused ion beam (FIB). The initial beam voltage and current were 30 kV and 2.5 nA, respectively. The current and voltage were then gradually reduced while thinning to final values of 1kV and 93 pA, respectively, to reduce and remove surface damage caused by the Ga-beam. The final thickness of samples was approximately 50 nm. The superlattices in this study were symmetric and contained n=1, 2, 4, and 27 unit-cells in a layer. One period of a n=4 SL is shown in Figure 7.1 as an example. Other examples of n=2 and n=3 are shown later in Figure 8.1. For brevity, the samples were named SL1, SL2, SL4, and SL27, after the number of unit-cells in a layer.

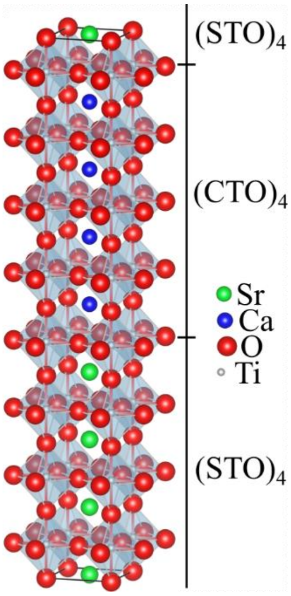

Figure 7.1. Schematic of SL4 (n=4).

8 Diffraction from a Superlattice Derivation

The theoretical background for diffraction from a generalized lattice was presented in Section 2. In this Section a theory will be developed that presents diffraction from a symmetric SL composed of layers containing n unit-cells of atomic lattice. We will reduce the number of dimensions from $\mathbb{R}^3 \rightarrow \mathbb{R}^1$ so that we consider only layers in a SL and planes in a crystalline lattice. This simplifies the clarity of the derivation, but the results are general for any dimensional SL.

Uppercase subscripts G and K are used to represent the SL and lower case will represent the atomic lattice, as shown in Figure 8.1.

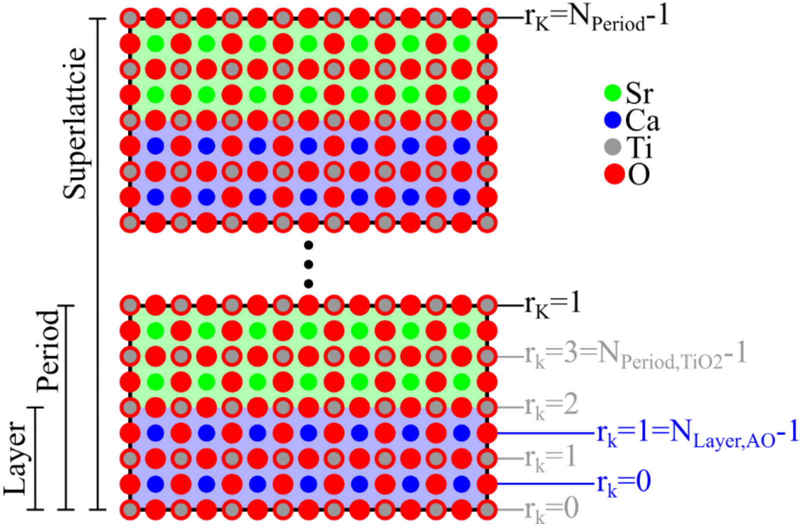

Figure 8.1. Schematic of a two unit-cell symmetric SL with various periodicities and lattice translation vectors labeled for reference. For clarity, r_k TiO_2 planes in a period were labeled explicitly from one to three and the CaO planes were labeled explicitly from one to two. r_k is in fact identical for AO and TiO_2 planes as they belong to the same unit-cell. The primary distinction is rather summing over a layer or period.

Equation 3.4 for the SL becomes,

$$\psi_{SL} = S_{SL} F_{SL} \qquad 8.1a$$

$$S_{SL} = \sum_{r_K=1}^{N_{Period}-1} e^{-iq_z r_K} \qquad 8.1b$$

$$F_{SL} = \sum_{r_G}^{SL\,Basis} f_{r_G} e^{-iq_z r_G} \qquad 8.1c$$

where N_{Period} is the number of periods within the SL sample. The TiO_2 layers share the same periodicity throughout the full SL period and therefore it is informative to split F_{SL} into the scattering from the TiO_2 and AO sublattices,

$$F_{SL} = F_{SL,TiO_2} + F_{SL,AO} \qquad 8.2a$$

$$F_{SL,TiO_2} = \sum_{r_g}^{TiO_2} f_{TiO_2} e^{-iq_z r_g} \qquad 8.2b$$

$$F_{SL,AO} = \sum_{r_g}^{AO} f_{r_g} e^{-iq_z r_g} \qquad 8.2c$$

where $F_{SL,i}$ is the scattering amplitude from TiO_2 or AO sublattices within a SL period.

The number of TiO_2 layers contributing to F_{SL,TiO_2} is well defined by the number of unit-cells in the SL period and the scattering from a TiO_2 layer is to first approximation identical in all $ATiO_3$ layers, such that,

$$F_{SL,TiO_2} = f_{TiO_2} S_{Period,TiO_2} \qquad 8.3a$$

$$S_{Period,TiO_2} = \sum_{r_k}^{N_{TiO_2}-1} e^{-iq_z r_k} \qquad 8.3b$$

where N_{TiO_2} is the number of unit-cells within the SL period, and L represents the index of the SL's reciprocal lattice along (001) similar to *l*'s relation to the pc crystal's reciprocal lattice. *L* follows the relation *l=L/2n*. In addition to the previously stated assumptions, Equation 8.3 is only valid for a SL that has identical TiO_2 interplanar spacing in the various layers, otherwise a phase shift needs to be between TiO_2 scatters needs accounted for. Combining Equations 8.1, 8.2a, and 8.3a provides,

$$\psi = S_{SL}\left(S_{Period,TiO_2} f_{TiO_2} + F_{SL,AO}\right) \qquad 8.4$$

The multiplication of S_{SL} with S_{Period,TiO_2} is the sum of all waves scattered from TiO_2 layers within the entire SL and as such the first term in Equation 8.4 amounts to the scattering amplitude of the TiO_2 sublattice

$$\psi_{TiO_2} = S_{SL} S_{Period,TiO_2} f_{TiO_2}$$

ψ_{TiO_2} is independent of i) the number of unit-cells in a layer and ii) the A species present in the layers. The importance of this term is that it represents the scattering from the TiO_2 backbone that extends throughout the entire quasi-1D SL. If the same analysis thus far is followed in 3D then a term ψ_{TiO_6} representing the TiO_3 octahedra backbone would appear.

The second term in Equation 8.4 accounts for diffraction from the AO sublattice is

$$\psi_{AO} = S_{SL} F_{SL,AO}$$

The AO sublattice cannot be factorized to the extent of the TiO_2 sublattice but given the translational symmetry and known number of unit-cells within layers, minor reductions can be made. The summation in Equation 8.2c can be broken into contributions from each layer,

$$F_{SL,AO} = F_{SL,SrO} + F_{SL,CaO} \qquad 8.5$$

where $F_{SL,SrO}$ and $F_{SL,CaO}$ represent the sum over AO planes in the CTO or STO layer in accordance with Equation 8.2c, with the first TiO_2 plane as the zero within the layer. For a symmetric SL, the number of AO planes in each layer is equivalent, so Equation 8.5 can be factored into a dimensional and compositional component,

$$F_{SL,AO} = S_{Layer,AO} F_{AO} \tag{8.6a}$$

$$S_{Layer,AO} = \sum_{r_k}^{N_{Layer,AO}-1} e^{-iq_z r_k} \tag{8.6b}$$

$$\begin{aligned} F_{AO} &= e^{-i\frac{\pi}{2n}L}\left(f_{SrO} + f_{CaO} e^{-i\frac{\pi}{2n}L}\right) \\ &= e^{-i\pi l}\left(f_{SrO} + f_{CaO} e^{-i\pi l}\right) \text{ when FR} \end{aligned} \tag{8.6c}$$

where $N_{Layer,AO}$ is the number of AO planes within a SL layer. $S_{Layer,AO}$, like other shape factors, does not contain information on the scattering amplitude from scatters within the (super)lattice, but describes the cumulative interference that results from the number of scatters. Note that Equation 8.3b and 8.6b for S_{Period,TiO_2} and $S_{Layer,AO}$, respectively, have identical arguments but are summed over a different number of lattice translation vectors, e.g. $N_{Period,TiO_2} = 2N_{Layer,AO} = 2n$. Remembering that the width of peaks given in S_i scales as scales as $(N_i a_i)^{-1}$, then the factorized representation gives the impression that constructive scattering within ψ_{TiO_2} will contribute to a much narrower peak than ψ_{AO}. F_{AO} contains the relative phase and amplitude of waves scattered from the generalized AO sublattice. The denominator in the exponents of Equation 8.6c makes F_{AO} a complex amplitude. The wave scattering amplitude from the CaO planes is $\pi L/2n$ out of phase with the SrO planes and is purely real when $L=2nl$, i.e. for a fundamental reflection (FR) of the underlying lattice. The amplitude is purely imaginary when $L=nl$, i.e. at the BZ of the SL. The first exponent describes the phase of the AO scattered waves relative to the TiO_2 scattered waves.

We will now consider Equations 8.1-8.6 collectively which will result in two representations of ψ both providing different perspectives. First, direct substitution of Equations 8.2-8.6 into Equations 8.1 provides the scattering amplitude of the SL and its constituent $ATiO_3$ lattice,

$$\psi = S_{SL}\left[S_{Period,TiO_2} f_{TiO_2} + S_{Layer,AO} e^{-i\frac{\pi}{2n}L}\left(f_{SrO} + f_{CaO} e^{-i\frac{\pi}{2n}L}\right)\right] \tag{8.7a}$$

represented in a way that describes i) the scattering from interfering layers containing AO planes and ii) the scattering from the TiO_2 plane backbone within the SL period. This emphasizes the interference of atomic sublattices. The shape factors S_{SL}, S_{Period,TiO_2}, and $S_{Layer,AO}$ amount to the magnitude of constructive interference within the SL, SL period, and layer, which depends on their thicknesses and reflects the regions of uniform periodicity.

The second representation relies on the superlattice being symmetric such that $N_{Period,TiO_2} = 2N_{Layer,AO}$. With the symmetric condition Equation 8.7a can be written as,

$$\psi = S_{SL}S_{Layer,AO}\left[\left(1+e^{-i\pi L}\right)f_{TiO_2} + e^{-i\frac{\pi}{2n}L}\left(f_{SrO} + f_{CaO}e^{-i\frac{\pi}{2n}L}\right)\right] \qquad 8.8b$$

which groups structure factor terms and shape factor terms. This emphasizes the interference of SL layers. From a first glance the first term in the brackets suggests that the TiO_2 planes can add out of phase when L is odd, however $L=2nl$ and therefore the phase is always a multiple of 2π enforcing constructive interference as would be expected form Equation 8.7a. There are two primary L conditions to consider: i) where L is a FR of the constituent $ATiO_3$ lattice, $L=2nl$, and ii) at the BZ of the constituent $ATiO_3$ lattice, at l=1/2. For condition (i)

$$\psi = S_{SL}S_{Layer,AO}\left[2f_{TiO_2} + f_{SrO}e^{-i\pi l} + f_{CaO}\right]$$

such that the SrO and CaO planes scatter πl out-of-phase. For l=odd, all planes scattering in-phase and for l=even the SrO planes scatter out-of-phase with the TiO_2 and CaO planes. For case (ii)

$$\psi = S_{SL}S_{Layer,AO}\left[(1+(-1)^n)f_{TiO_2} + f_{SrO}e^{-i\frac{\pi}{2}} - f_{CaO}\right]$$

Now we find that the scattering amplitude from the TiO_2 planes in the two layers depends on the number of unit-cells in a layer. For n=odd the TiO_2 planes deconstructively interfere. providing zero intensity at the BZ. For n=even the TiO_2 planes constructively interfere, providing intensity at the BZ. An odd result is that the CaO planes always contribute a constant amplitude and the SrO planes always contribute an imaginary amplitude, both being independent of the number of unit-cells. The intensity at the BZ ($|\psi|^2$) is therefore non-zero for both odd and even n if only structure factor-like terms are considered!

The intensities associated with the shape factor terms S_L, S_{SL}, and S_LS_{SL} in Equation 8.8 are plotted in Figure 8.2 for in SL1, 2, 4 and 27 (the samples studied in this thesis). The total intensity from cumulative interference of the lattice is the product of the two, $N_{SL}^2N_{AO}^2$, which is equivalent to all planes in the SL. The damping function of the AO layers causes a reduced intensity at the BZ such that the total intensity at the BZ is much less than at the FRs. Another result from factoring into S_{AO} and S_{SL} is that S_{AO} determines the apparent superlattice reflections (SLR) that are present. For example, the second SLR is missing in SL4. This is because the first minimum of S_{AO} is at $q_z = 2\pi/N_{AO}a$ which is always a SLR. Further minima occur at integers of $2\pi/N_{AO}a$. Therefore, the BZ intensity for n=even is zero and for n=odd is one. Reflections observed at the brillouin zone in SLs with n=even (such as SL2 and SL4) are therefore Bragg reflection from the underlying lattice signaling the doubling of the lattice along the given BZ direction.

This section presented the theory for diffraction from a one-dimensional SL comprised of a TiO_2 backbone and layers with different AO planes. It was concluded that the scattered intensity associated F_{SL}, for any period SL will have, is non-zero. However, the intensity associated with

S_{AO} at a BZ is zero for even period SL and one for odd period SL. The total intensity at the BZ, that is the product of F_{SL}, S_{SL}, and S_{AO}, for an n=odd is therefore $|F_{SL}S_{AO}|^2$ and zero for n=even.

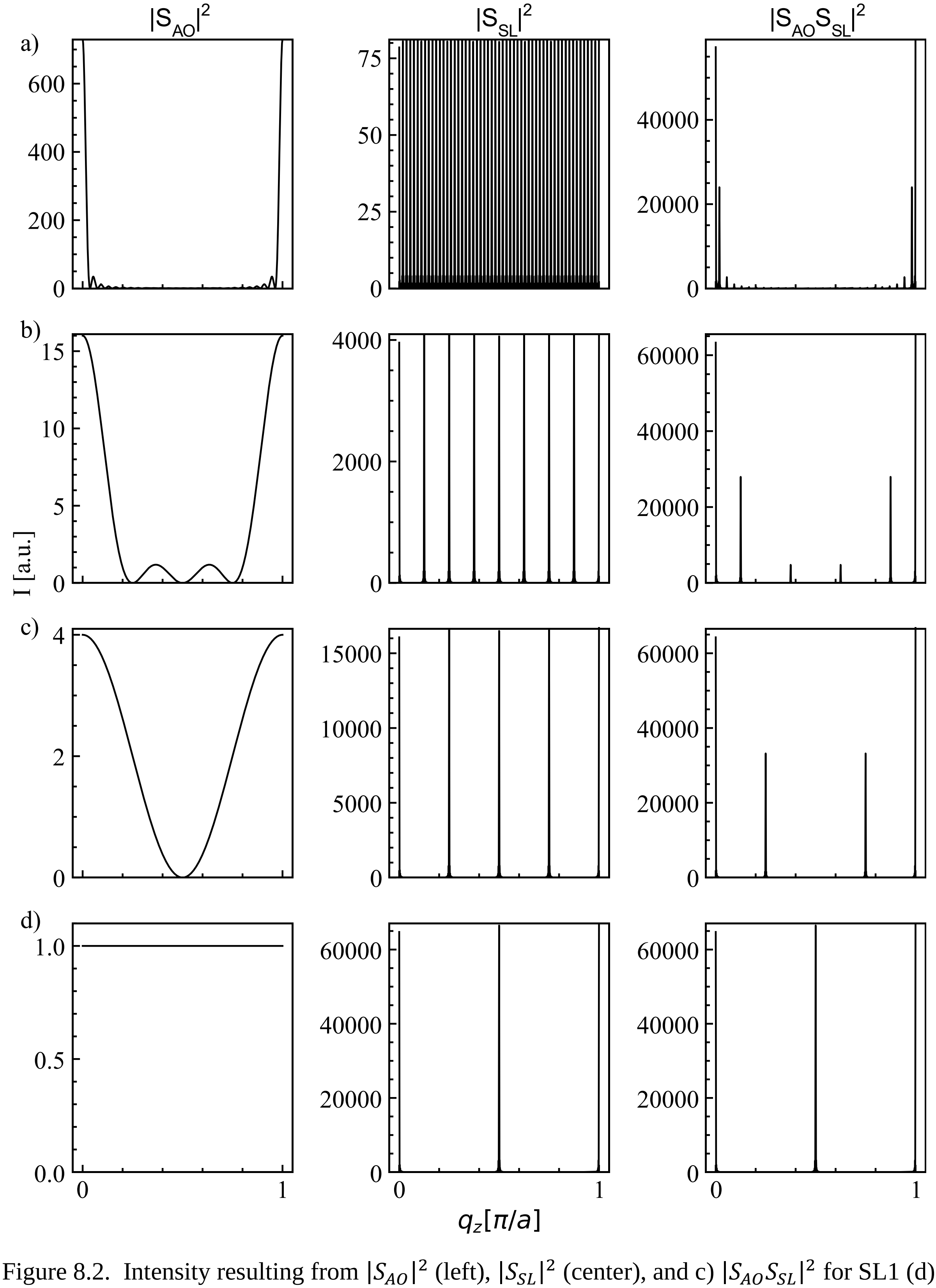

Figure 8.2. Intensity resulting from $|S_{AO}|^2$ (left), $|S_{SL}|^2$ (center), and c) $|S_{AO}S_{SL}|^2$ for SL1 (d), 2 (c), 4 (b), and 27 (a).

9 Superlattice-Dependent Crystal Structure

In this section, and subsections, the crystal structure of the STO and CTO phases within the SL is discussed in addition to the orientation of the lattices. This is done through the analysis of TEM images, SADP, CBED, XRD, HAADF, and iDPC.

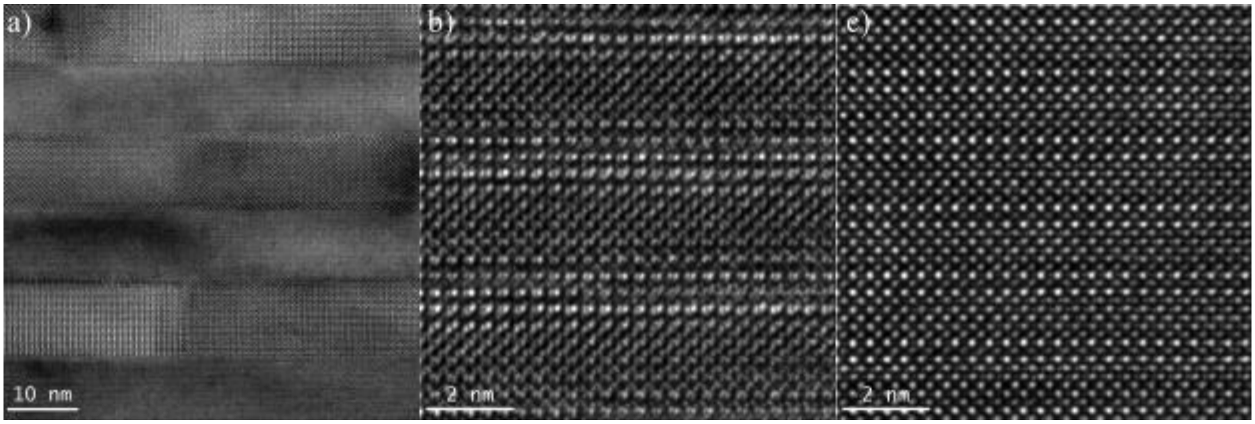

Figure 9.1. HRTEM images in a pc ZA for SL27 (a), 4 (b), and 2 (c). are seen in (a) while not in (b) or (c).

Figure 9.1 shows representative images from SL27, 4, and 2. The intensity of the atomic columns follows the same periodicity as the number of unit-cells within the respective SL, appearing well ordered. Contrast changes in SL27 within a layer are the result of differently oriented CTO domains. Domains were observed in SL27 but not in SL4 and 2. The microstructural and crystallographic details of the SLs are discussed in Sections 9.1, 9.2, and 9.3 as follows.

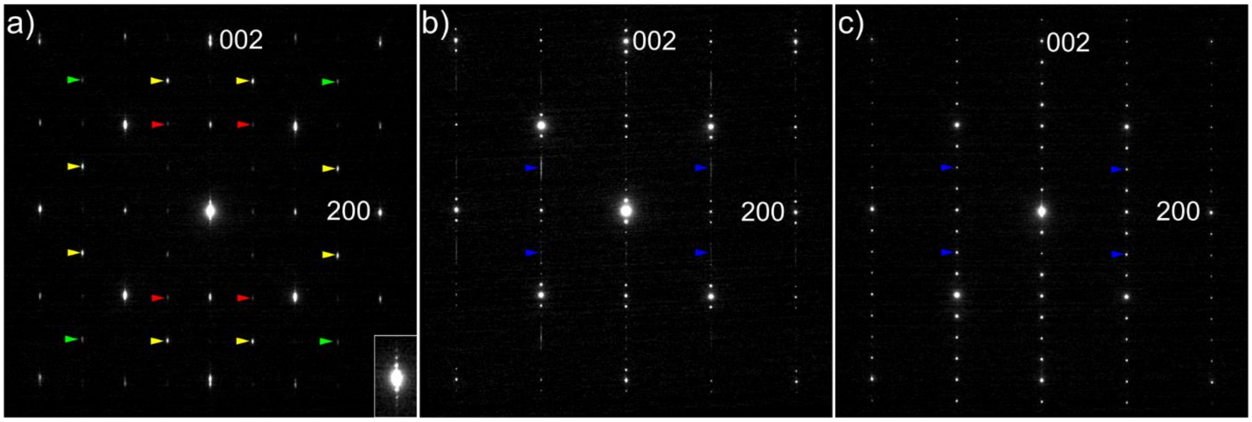

Figure 9.2. ZA SADP along the pc axis in SL (a) 27, (b) 4, and (c) 2 grown on NGO. In (b) and (c) SLRs are seen in the 001 direction. In (a) the SLRs were not individually distinguishable at low camera lengths, the insert shows the SLRs from an acquisition with higher camera length. ORs ½{102}$_{pc}$ from two domain variants are shown by blue and red arrows, and ½{303}$_{pc}$ and ½{103}$_{pc}$ ORs from a third domain variant are indicated by green and yellow arrows.

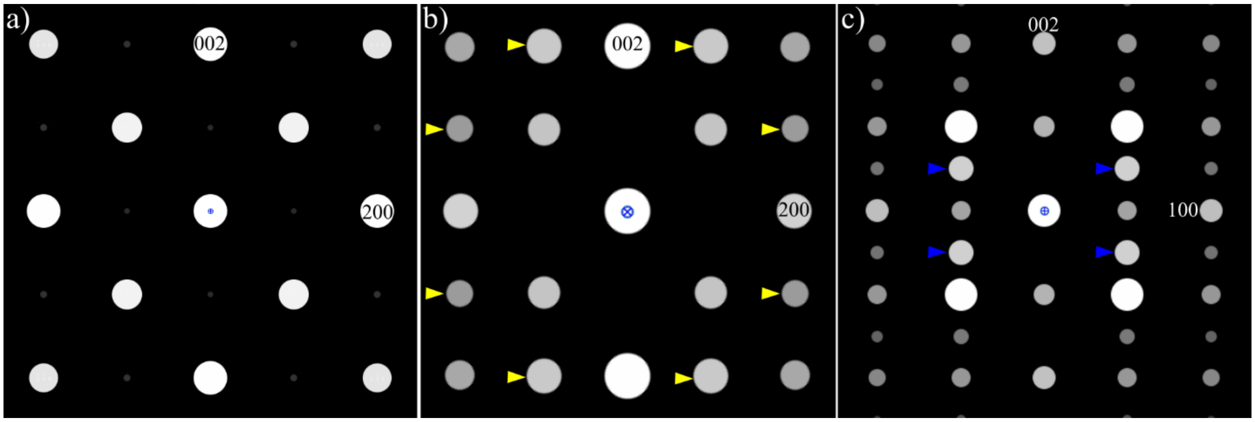

Figure 9.3. Simulated SADP for: (a) $Pm\bar{3}m$ and (b) Pbnm along the in-phase tilt axis and (c) along one of the out-of-phase tilt axes. Blue and yellow arrows indicate the same ½$\{102\}_{pc}$ and ½$\{103\}_{pc}$ OR, respectively, observed in the experimental SADP shown in Figure 9.2.

Figure 9.2 shows the SADP for SL27, 4, and 2 taken on a pc ZA. The $(002)_{pc}$ Bragg reflection of SL27 was split into two peaks. This is a result of the lattice relaxing out of plane, and the STO and CTO phases taking on the monolithic equilibrium phases. Only one $(200)_{pc}$ Bragg reflection was seen, so the layers remained epitaxially strained. The $(002)_{pc}$ Bragg reflection was not split in SL2 or 4, meaning the lattice parameter was identical in STO and CTO layers. The SADP for SL1, as shown in Figure 9.23(e), also showed a single $(002)_{pc}$ peak.

XRD was performed with a 2θ-ω scan geometry to determine the out-of-plane pc lattice constant. The NGO substrates $(002)_{pc}$ was used for alignment and the calculated lattice parameter showed minimal deviation between samples. It is assumed that the measured lattice parameter of the NGO substrate should be identical for all techniques and all samples. Therefore, all SADP and XRD measurements of STO, CTO, and NGO were scaled such that the NGO $(002)_{pc}$ lattice parameter equaled the average NGO $(002)_{pc}$ lattice parameter of the XRD scans. Lattice parameters were extracted from the SADP in Figure 9.2 and Figure 9.23(e), and the scaled values are shown in Table 9.1. The lattice parameters calculated from XRD experiments are shown in Table 9.2. The scaled lattice parameters from SADP and XRD are plotted together as a function of SL period in Figure 9.4.

Table 9.1. Scaled lattice parameters calculated from SADP in SL1-27. Values are in Å.

	002			**200**
	STO	**CTO**	**NGO**	**STO/CTO**
1	3.876		3.862	3.880
2	3.874			3.873
4	3.872			3.866
27	3.925	3.806		3.876

Table 9.2. Scaled lattice parameters calculated from XRD in SL1-27. Values are in Å.

	STO	**CTO**	**NGO**
2	3.873		3.862

4	3.872		
27	3.804	3.946	

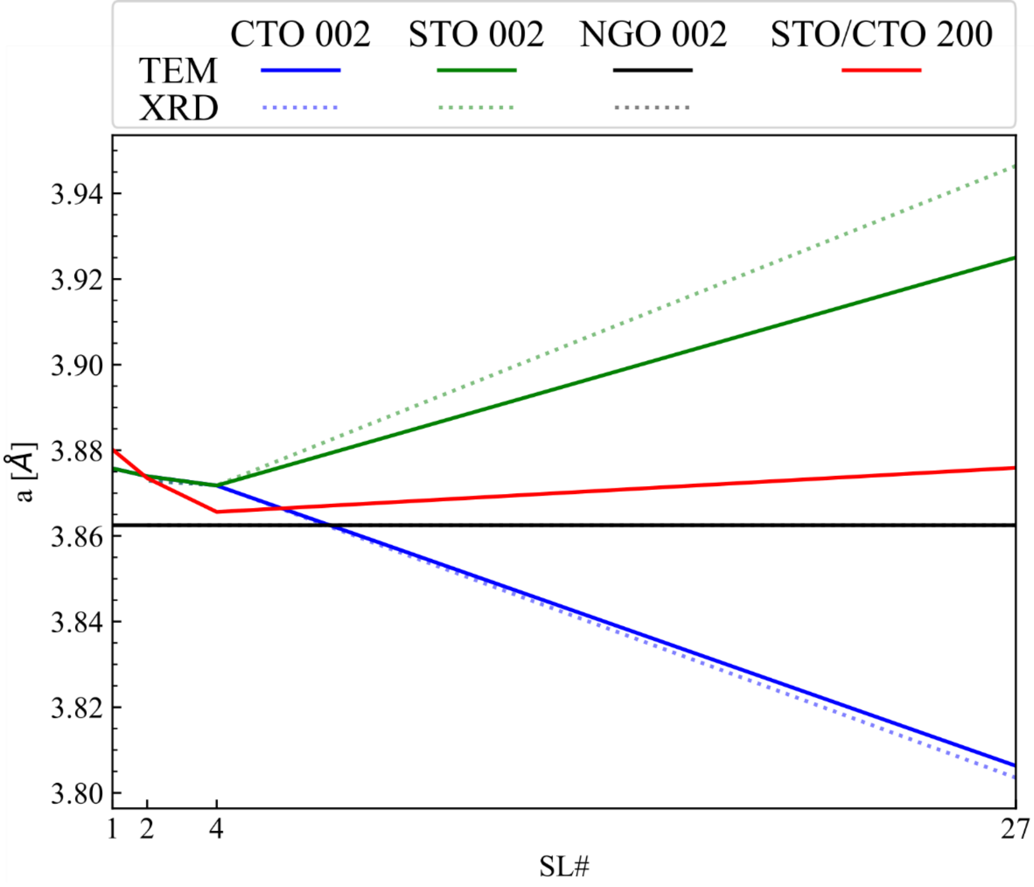

Figure 9.4. Calibrated lattice parameter calculated from the $(002)_{pc}$ Bragg peak using TEM (solid) and XRD (dotted) for CTO (blue), STO (green), and the NGO substrate (black). The in-plane lattice parameter for STO and CTO calculated from the $(200)_{pc}$ Bragg peak in a SADP is shown (red).

From the measured lattice parameters, it was found that the out-of-plane lattice parameter converged to a single STO/CTO value that was approximately the average of the two unrelaxed lattice parameters of SL27. This is a theme that will arise throughout the thesis, that is the lattices are finding a “happy medium”. The in-plane lattice parameter was different (but nearly equivalent) to the substrate in SL4 and 27. SL2 and 1 had in-plane lattice parameters similar to their out-of-plane lattice parameter and were larger than SL 4 and 27, indicating that the film in-plane lattice parameters are not determined by the substrate.

9.1 SL27: Development of a Preferential Orientation Relation in $CaTiO_3$

This subsection will focus on SL27. It is shown using SAD, scanning-CBED, HAADF, and iDPC that the STO and CTO layers exhibited their standard room temperature and pressure phases. It is then shown that out-of-phase tilt displacements persist across the STO-CTO interface into STO, because of coupling between the two layers. Rotation of the octahedra was not rigid, but had some distortion of the TiO_6 octahedra such that the displacements within the oxygen octahedra are considered as out-of-phase like displacements.

The SADP of SL27 is shown in Figure 9.2(a). The $(002)_{pc}$ Bragg reflection of SL27 was split into two peaks corresponding to interplanar spacings of 3.80 and 3.92 Å, which are the lattice parameters of monolithic CTO and STO, respectively. This shows that the STO and CTO have relaxed to their monolithic equilibrium phases. The $(200)_{pc}$ peak corresponded to an interplanar spacing of 3.85 Å and did not exhibit splitting, therefore the STO and CTO layers within the superlattice grew epitaxially with one another. The STO lattice parameters of 3.92 and 3.85 implies that the epitaxial strain has forced the lattice into a non-cubic symmetry. The SAED pattern had ORs at $\frac{1}{2}(102)_{\mathrm{pc}}$ and $\frac{1}{2}(\bar{1}02)_{\mathrm{pc}}$, which are of the type $\frac{1}{2}(\mathrm{oee})_{k\neq l_{\mathrm{pc}}}$ signifying mixed tilting of TiO_6 octahedra or antiparallel Ca displacements parallel to $[0\bar{1}1]_{pc}$. ORs $\frac{1}{2}(303)_{\mathrm{pc}}$ and $\frac{1}{2}(\bar{3}03)_{\mathrm{pc}}$ were also observed and are $\frac{1}{2}(oeo)_{h\neq l}$ ORs that signify in-phase tilting of TiO_6 octahedra. This SADP is the superposition of Pbnm taken along the a $[001]_{pc}$ ZA and a $[010]_{pc}$ ZA, shown in Figure 9.3(b,c), with $[001]_{pc}$ lying in plane. This suggests two domains both with the Pbnm c-axis in plane. $\frac{1}{2}(102)_{\mathrm{pc}}$ ORs were rarely observed and when present were faint due to a low volume fraction sampled by the SA, suggesting that Pbnm CTO with c-axis out-of-plane was rare. The orientation relation of the domains within the CTO layer was $[100]_{pc-CTO}//[010]_{pc-CTO}$.

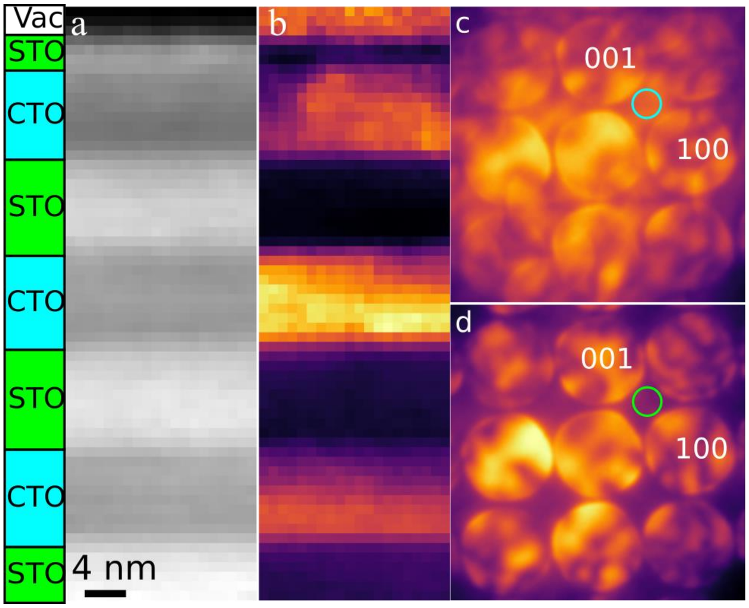

Figure 9.5. (a) HAADF acquired during a scanning NBED scan in SL27. Position averaged convergent-beam electron diffraction (PACBED) patterns for: (c) the top CTO and (d) STO layers. (b) The intensity in the virtual DF is from the virtual aperture marked in (c) and (d).

The split $(200)_{pc}$ peak suggested that the layers relaxed to close to their monolithic phase lattice parameters, but this does not rule out tilting within the STO phase. Unlike the $(200)_{pc}$ and $\{202\}_{pc}$ Bragg reflections, OR splitting was not observed. Therefore, it was safe to assume that tilting was not present in STO. It is quite possible that the OR of STO are too faint and indistinguishable from the CTO ORs. To further investigate scanning NBED was performed in SL27, as shown in Figure 9.5. The STO layers in Figure 9.5(a) appear brighter because Sr is heavier than Ca. The PACBED in CTO had ORs at $\frac{1}{2}\{101\}_{pc}$ and STO did not, as shown in Figure 9.5(c,d). This is reflected in the virtual DF image, Figure 9.5(b), by CTO layers appearing bright and STO layers appearing dark. It is experimentally convenient that the semi-convergence angle was equal to the Bragg angle of CTO. This condition means that $(001)_{pc}$ and $(100)_{pc}$ OR discs would contribute intensity to an aperture centered at $(101)_{pc}$. Therefore, both CTO domain orientations contributed intensity to the virtual DF image.

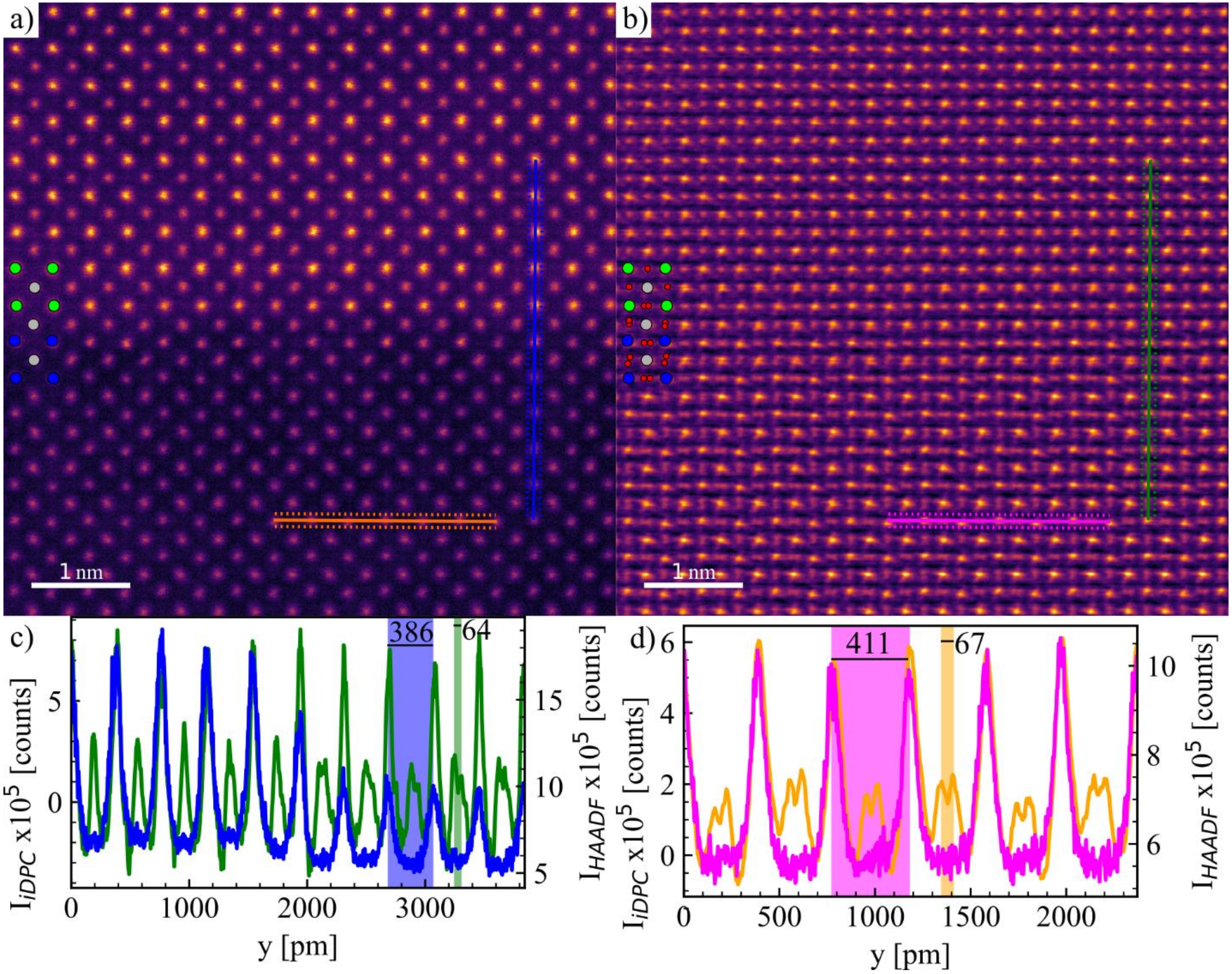

Figure 9.6. False color: (a) HAADF and (b) iDPC image taken at 15.3Mx of SL27. In (a) one unit-cell is illustrated on each side of the interface with Sr, Ca, and Ti indicated by green, blue, and gray circles, respectively. The (b) iDPC image shows the same unit-cell with oxygen indicated with red circles. (c,d) The integrated signal from 30 pixel wide line profiles shown in (a) and (b). The HAADF signal in (c) showed the transition from Sr to Ca columns. The signal in (c) and (d) are from out-of-plane and in-plane directions, respectively. All signals and line profiles are color coded. Oxygen column peak splitting is clear in the iDPC line profiles.

A HAADF and iDPC image at 15.3Mx of SL27 are shown in Figure 9.6. A full SL period is not in the field of view but this magnification allowed for clear visualization of the oxygen columns in Figure 9.6(b). In Figure 9.6(a), the HAADF image, with intensity proportional to atomic number, shows a well terminated interface between the STO and CTO layers. The in- and out-of-plane lattice parameters in the CTO were measured as 386 and 411 pm, respectively, as shown in Figure 9.6(c,d). This agrees with SAD data presented in this thesis and literature values. Using the line profiles in Figure 9.6(a,b) as reference, it is also observed that every other Ca column is anti-parallel displaced. The oxygen positions in the STO layer are well aligned into a single atomic column, as shown in Figure 9.6(b) or the line profiles in Figure 9.6(c,d). On the lower half of Figure 9.6(b), in the CTO layer, oxygen columns appear as dumbbells as a result of octahedral tilting separating the columns. The projected distance between the columns was 67 pm in-plane and 64 pm out-of-plane. The position of each column of oxygen was manually located and the tilt angle for each octahedra measured, as shown in Figure 9.7.

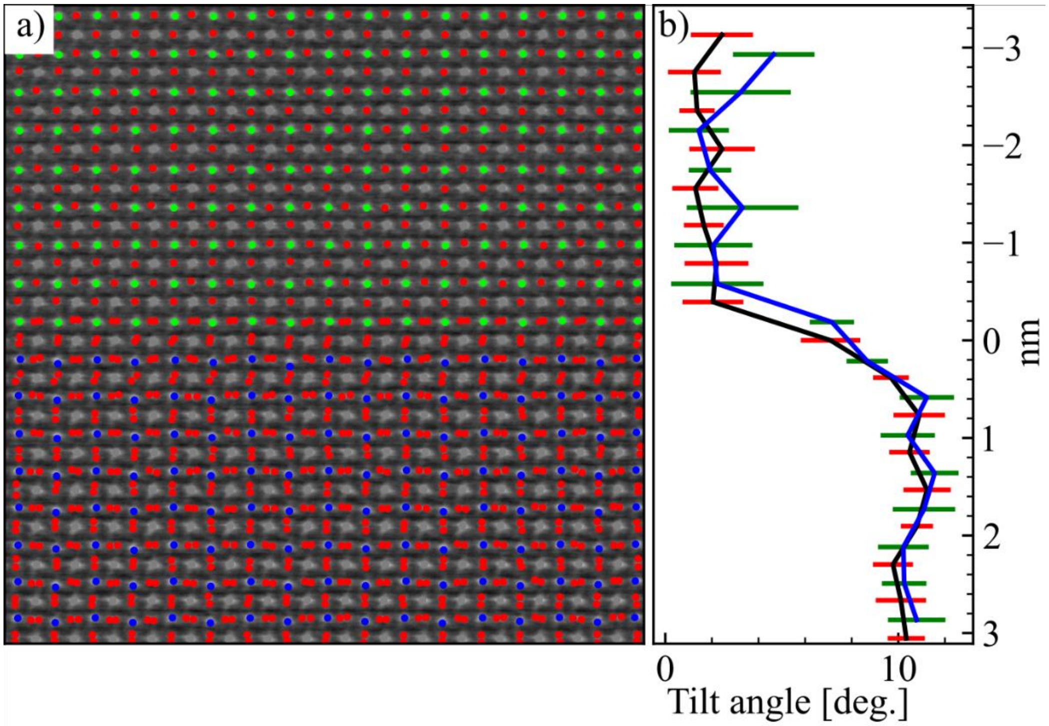

Figure 9.7. (a) iDPC image of SL27 with manually assigned column positions overlaid. (b) Average of the measured tilt angle from the (black) TiO_2 plane and (blue) AO plane. Red and green error bars represent the standard deviation within the plane. The zero on the y-axis indicates the chemically assigned TiO_2 interface plane.

Center-of-mass and Gaussian fitting was not used to refine the atom positions because these methods did not handle the proximity of the split columns well. Because only single oxygen columns were discernible in the STO the out-of-phase angle is zero and the plotted values are in-phase tilt angles calculated as $(180^{o} - \measuredangle \mathrm{OTiO})/2$, where the two O are on opposite sides of the central Ti atom. The in-phase tilting in the STO layer was 1.84^{o} and 2.69^{o} in the TiO_2 and AO planes, respectively. No in-phase tilting is expected within the STO layers and the small values could result from manual placement of the O columns or be a physical result from coupling of the ATO layers. In the CTO and at the interface where the split O columns were apparent the out-of-phase angle was measured as $\measuredangle \mathrm{OTiO}/2$, where the two O are the split sites. The out-of-phase tilting in the CTO layer was 10.04° and 10.32° in the TiO_2 and AO planes, respectively. It is interesting to now consider the question "what is the interface?", is it the TiO_2 plane that separates the STO and CTO layers or is it diffuse extending further into the layers? If only chemistry is considered, then the interface is abrupt with all A-sites above the TiO_2 interface being Sr and all below the TiO_2 interface being Ca, as seen in the HAADF image shown in Figure 9.6(a). If the structural distortions in the TiO_6 octahedra that result from coupling between the layers is considered, then there is a three layer decay of the tilt angle from CTO into STO, and therefore, the interface is diffuse, consisting of these three layers. If the AO-TiO_2-AO section of the interfacial region is examined in the iDPC image, as shown in Figure 9.7(b), the split O columns in the AO plane have the same orientation as the O columns in CTO. The split O columns in the TiO_2 plane (ie the "chemical interface") are sheared relative to the vertical split O columns in the TiO_2 planes in CTO. The shearing in the TiO_2 plane and non-shearing in the AO planes results in a distorted TiO_6 octahedra. This $CaSrTi_2O_6$ structural unit with out-of-phase tilting and distortion of TiO_6 octahedra along the ZA repeats 2 dimensionally forming an interface layer. One can therefore characterize the interface as being chemically abrupt, structurally diffuse, or as a $(1\mathrm{x}1\mathrm{x}2)_{pc}$ structural unit with out-of-phase tilting and distortions of the TiO_6 octahedra.

Measurement of the TiO_6 tilt angle is only as accurate as the placement and discernability of split O columns. An alternative approach is to assign a single position to each split or non-split column of atoms then fit the column with a 2-dimensional Gaussian. The fitted Gaussian for single columns is symmetric and the fitted Gaussian for split columns is elliptical. The ellipticity of a Gaussian is defined by

$$elip. = \begin{cases} {}^{\sigma_x}\!/_{\sigma_y} \text{ when } \sigma_x > \sigma_y \\ {}^{\sigma_y}\!/_{\sigma_x} \text{ when } \sigma_y > \sigma_x \end{cases}$$

where σ is the standard deviation of the Gaussian. The ellipticity in the AO layers is represented in Figure 9.8(a,b) as a vector image and Figure 9.9 as an intensity map. Figure 9.8(c) shows a line profile of the mean and standard deviation of ellipticity in each plane.

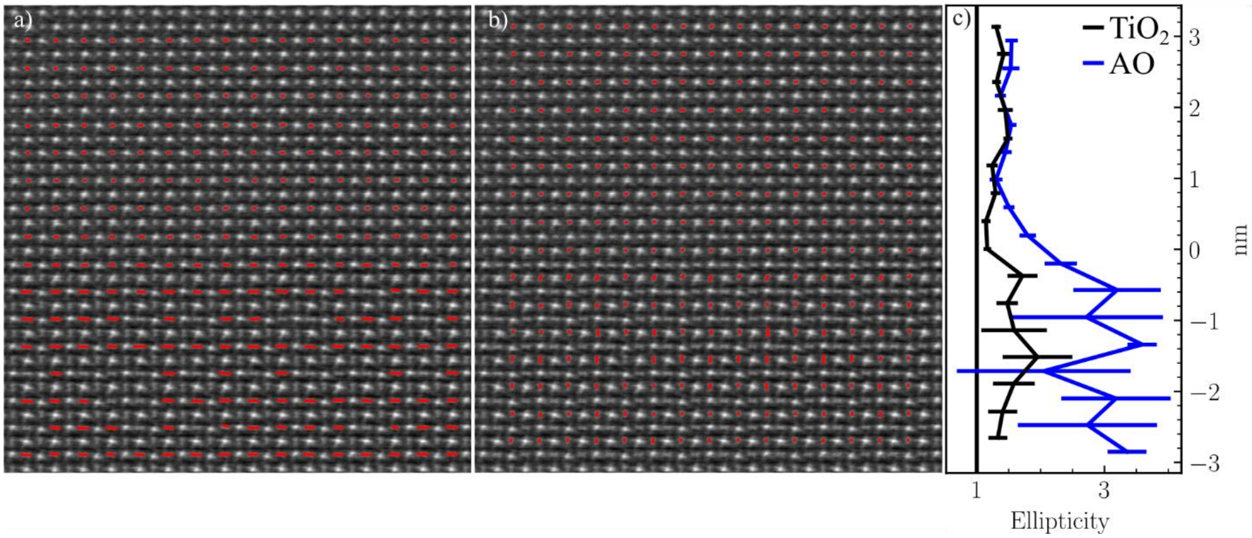

Figure 9.8. iDPC image of SL27 with a vector overlay representing the ellipticity of columns in (a) AO and (b) TiO_2 planes. (b) a line profile showing the mean and standard deviation of ellipticity within an (blue) AO (black) TiO_2 plane. The zero on the y-axis indicates the chemically assigned TiO_2 interface plane.

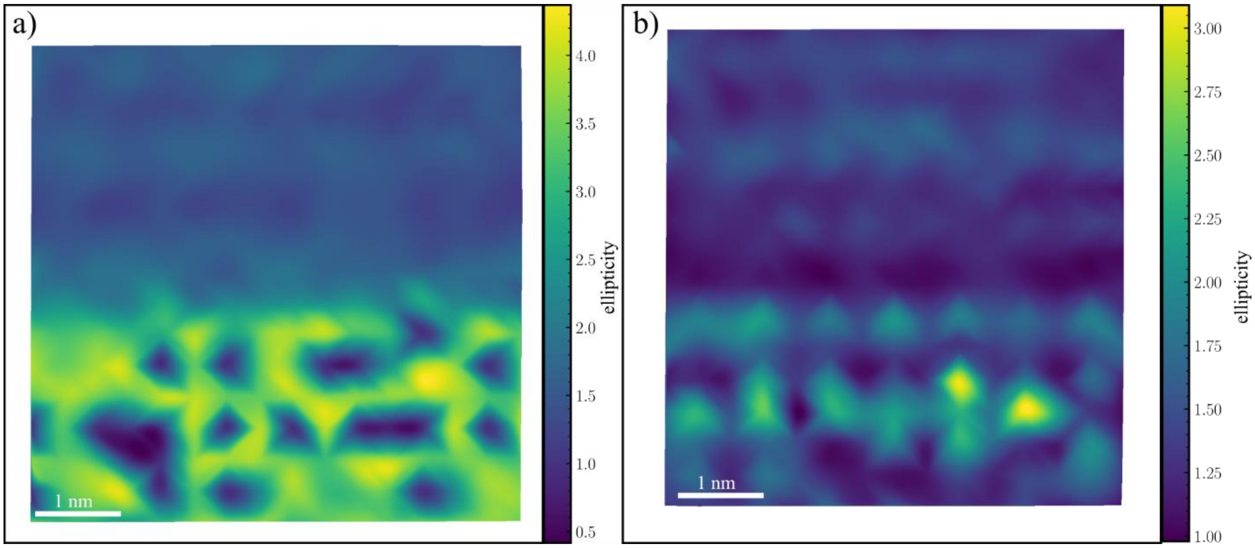

Figure 9.9. Ellipticity measurements for split O columns in (a) AO and (b) TiO_2 planes of SL27.

The measured values in the STO layer are not equal to one as expected for a single column because the fitted Gaussians are influenced by the intensity of the neighboring A and Ti columns. This skewing of ellipticity from neighboring A and Ti columns is also expected to occur in the CTO layer but to lesser degree because the Ca is less intense. The ellipticity profile, as shown in Figure 9.8(c), has the same overall trend as the directly measured out-of-phase angle measurements shown in Figure 9.7(b). The approximately 10^{o} out-of-phase angle in CTO AO layers translates to an ellipticity of roughly 3 and the 0° out-of-phase angle in STO translates to an ellipticity of roughly 1.5. The approximately 10° out-of-phase angle in CTO TiO_2 layers translates to an ellipticity of roughly 1.6, and the 0° out-of-phase angle in STO translates to an ellipticity of roughly 1.3. The fitting of the single Gaussian to two columns is not linear and some fitting errors are present as observed in the STO region, these results do however provide a benchmark for the relation of ellipticity to an out-of-phase angle measurement in the two layers. The zero on the y-axis of Figure 9.8(b) indicates the chemically assigned TiO_2 interface plane. The ellipticity of the first CaO plane is slightly lower than in the CTO layer. The first SrO plane, and arguably the second SRO plane, are at values higher than in the STO layers. The ellipticity value in the TiO_2 planes does not show as large of a gap between STO and CTO layers so does not provide for the same perspective but if the direction of the ellipticity is consider, as shown in Figure 9.8(b), the interface and even the skewed distortions are seen. This shows that the ellipticity measurements show the same trend as directly measuring out-of-phase tilt angles without the use of column positioning manually chosen. The ellipticity parameter thus allows for a qualitative measure of out-of-phase tilt angle that can be automated for a larger field-of-view and for column splitting not discernable to the human eye.

Splitting of $(002)_{pc}$ and $\{202\}_{pc}$ diffraction peaks and non-split OR indicated that the thin film had relaxed to Pbnm-CTO and strained Pm$\overline{3}$m-STO, much like the monolithic constituents. The presence of $\frac{1}{2}(102)_{\mathrm{pc}}$ and $\frac{1}{2}(303)_{\mathrm{pc}}$ ORs and absence of $\frac{1}{2}(201)_{\mathrm{pc}}$ ORs indicated two domains of CTO were present with c-axes in the plane of the film and an orientation relation of $[100]_{pc-CTO}//[010]_{pc-CTO}$. The Pbnm-CTO and Pm$\overline{3}$m-STO phases were then further confirmed using scanning NBED. Using iDPC an in-phase tilt angle was measured in the STO layer as 1.84° and 2.69° in the TiO_2 and AO planes, respectively, and is thought to result from either an error in the manual placement of O positions or coupling between the ATO layers of the SL. The out-of-phase tilting in the CTO layer was 10.04° and 10.32° in the TiO_2 and AO planes, respectively. The interface between the STO and CTO layers of the SL was characterized as chemically abrupt, structurally diffuse, and as a $(1x1x2)_{pc}$ structural unit with out-of-phase tilting and distortions of the TiO_6 octahedra.

9.2 SL2 and SL4: To a Happy Medium

This subsection will focus on SL2 and SL4. It is shown using SAD and CBED that the entire superlattice takes on a singular orientation and has octahedral tilting in both phases. It is then shown using iDPC and HAADF that out-of-phase tilt-like displacements in the oxygen octahedra reminiscent of the interface structural unit in SL27 are present in both SL4 and SL2. In SL4 minima and maxima inn the out-of-phase tilt angle are still present but are not in SL2, showing that the system transitions from an interface dominated structure to a singular phase.

The SADP of SL2 and 4 are shown in Figure 9.2(b) and (c), respectively. The density of diffraction spots in the SADPs is much higher than observed for SL27. SLRs appear continuously between the fundamental pc reflections with decreasing amplitude approaching the BZ. Additionally, no peak splitting was observed in SL2 or 4 along $(200)_{pc}$ indicating that a lattice took on a singular pc lattice parameter both in-plane and out-of-plane. The measured SLR spacing in SL2 was 0.645 nm^{-} (c_{SL}=1.549 nm) corresponding to a pc lattice parameter of c=3.873

Å. The measured SLR spacing in SL4 was 0.032 nm^{-} (c_{SL}=3.098 nm) corresponding to a pc lattice parameter of c=3.872 Å.

Intensity was observed where the $\frac{1}{2}(201)_{pc}$ OR should be in the SADP of SL2 and 4. Based on the periodicity of the SLRs this could also be a SLR. The shape factor for the AO sublattice with $n=even$ is zero at BZs, and because the total intensity is proportional to the squared product of the lattice and SL shape factor then the intensity of a SLR at $\frac{1}{2}(201)_{pc}$ must be zero, as derived in Section 6. To back this theory, a SADP was simulated from a two unit-cell STO-CTO SL with the backbone lattice having a Pm$\overline{3}$m space group using JEMS, as shown in Figure 9.10.

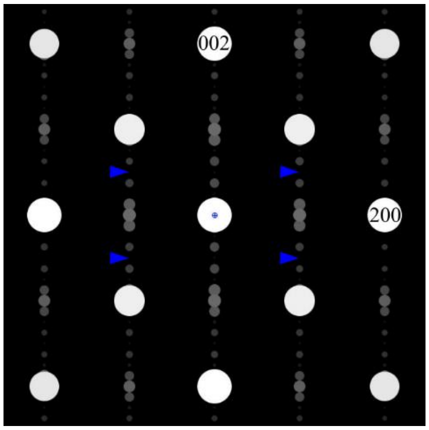

Figure 9.10. Simulated SADP of a STO-CTO SL with the backbone lattice having a Pm$\overline{3}$m space group. The blue arrows marking $\frac{1}{2}(201)_{pc}$ show the lack of a SLR.

The ½$(201)_{pc}$ positions are indicated with blue arrows and have zero intensity. Therefore, any intensity observed at these positions is a result of octahedral ordering and not the SL. Therefore, the intensity in Figure 9.2(b) and (c) is from an OR and not a SLR. In addition, the intensity of the peak at ½$(201)_{pc}$ in SL4 is higher than the surrounding SLR, which is in disagreement with the $1/(q_z a_{SL})^2$ envelope function decaying toward the BZ, thus providing further evidence that the reflection in the SADP is an OR. Interestingly the SLR in SL4 had a diffuse background that may provide insight toward strain, order, or softening phonon modes, but the exact origins are unknown.

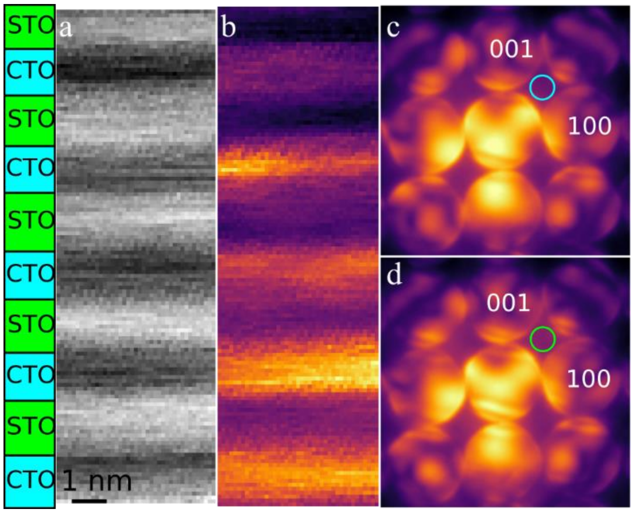

Figure 9.11. (a) HAADF acquired during a scanning NBED scan in SL4. PACBED patterns for: the (c) top CTO and (d) STO layers. (b) The intensity in the virtual DF is from the virtual aperture marked in (c) and (d).

Scanning-CBED was performed to identify the DP from an individual layer rather than the entire SL. The PACBED patterns shown in Figure 9.11(c) and (d) from CTO and STO layers, respectively, show much more similarity than PACBED patterns from SL27, as shown in Figure 9.5. The main difference between Figure 9.11(c) and (d) is the intensity at ½$\{101\}_{pc}$ positions that appears as background intensity, but could also be from discs at ½$(001)_{pc}$. The intensity variation of ½$(101)_{pc}$ was largest in the CTO layers, meaning that the octahedral tilts were largest in the CTO layers. The STO layers have a non-zero intensity at the virtual aperture positions. This indicates that octahedral ordering occurred within the STO layers. Therefore, STO no longer was $Pm\bar{3}m$, but rather, inherited tilting from the CTO layers approaching a singular crystal structure.

The ½$\{201\}_{pc}$ OR in the [010] ZA of SL2 and 4, as shown in Figure 9.2(b) and (c), appear at 90^{o} to the ½$\{201\}_{pc}$ OR in SL27. This indicates that the c-axis is out of plane, if the CTO monolithic Pbnm space group is assumed. This would place the in-phase tilt axis in the growth direction and normal to the SL. In general, if the Pbnm space group is not assumed, the ½$\{201\}_{pc}$ OR all with ½$(eeo)_{h\neq k}$ indicated a mixed tilt system which induces anti-parallel A-site displacement.

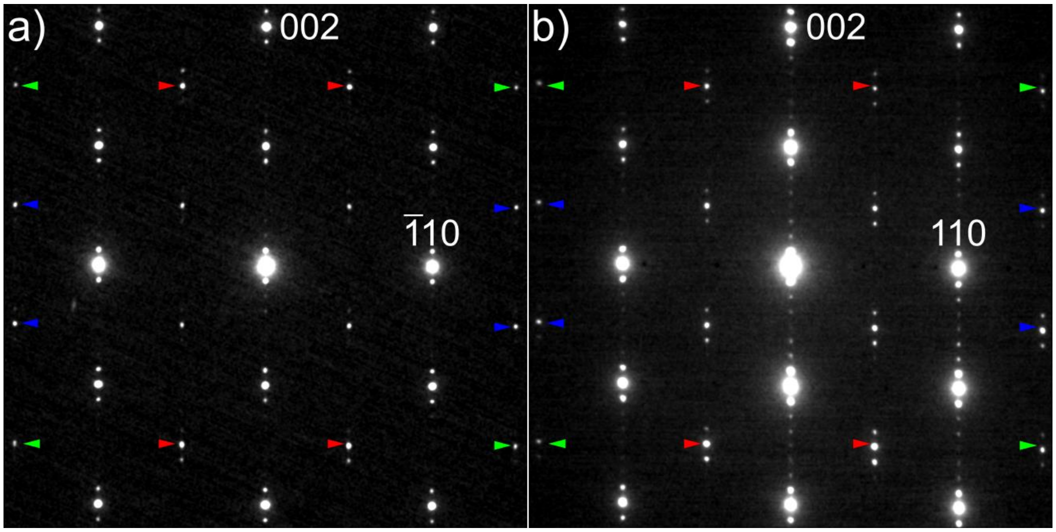

Figure 9.12. (a) SADP in $[1\bar{1}0]$ and (b) $[\bar{1}10]$ ZAs showing ½{113} (red), ½{331} (blue), and ½{333} (green) ORs.

SADP of SL4 were also acquired for the two in-plane $\langle 110\rangle_{pc}$ ZAs, as shown in Figure 9.12. The SADPs showed the same SLR that were observed in the [010] ZA, as shown in Figure 9.2. ½$\{ooo\}_{h\neq k}$ and ½$\{ooo\}_{k\neq l}$ were observed in the $\langle 110\rangle_{pc}$ ZAs indicating an out-of-phase tilt axis along $[100]_{pc}$ and/or $[010]_{pc}$ with unequal tilt angles, refer to the rules in Section 1.2 and Table 1.5 for tilt systems with combined in- and out-of-phase tilts. This would rule out the possibility of the SL adopting the Pbnm space group from monolithic CTO, leaving only space groups $P2_1/m$ ($a^-b^-c^+$) and Cmcm ($a^0b^-c^+$). It is to be noted that ½(ooe) and ½(eeo) OR are expected in both the $[1\bar{1}0]$ and $[\bar{1}10]$ ZA of $P2_1/m$ and Cmcm space groups, but none were observed.

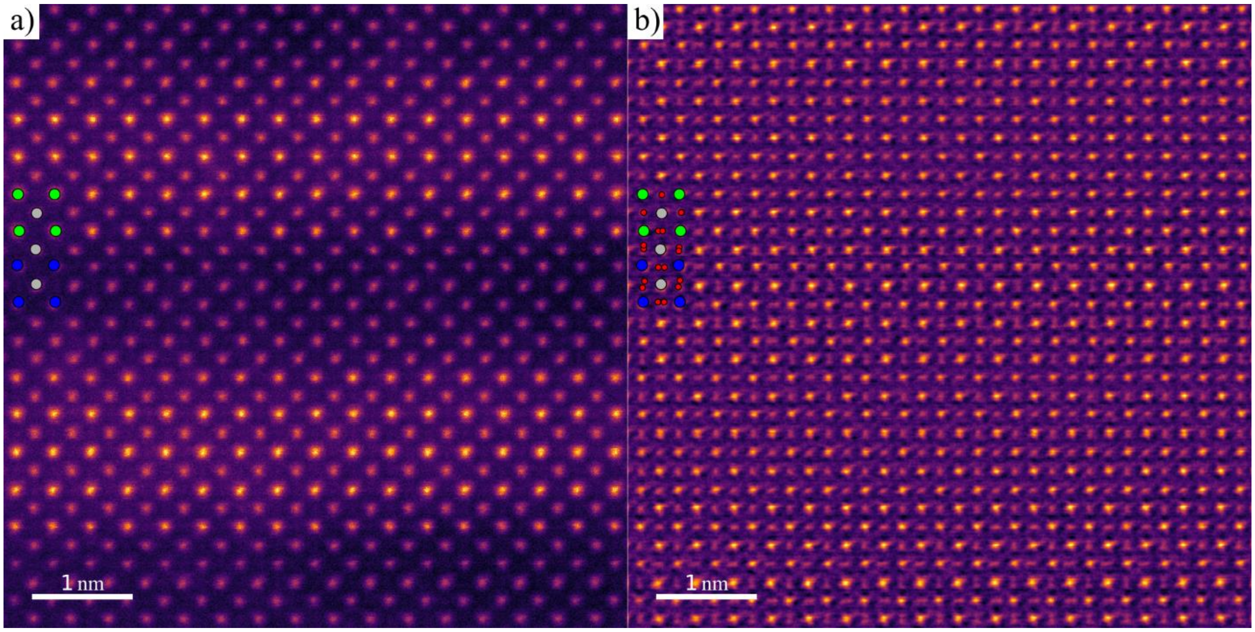

Figure 9.13. False color: (a) HAADF and (b) iDPC image taken at 15.3Mx of SL4. In (a) one unit-cell is illustrated on each side of the interface with Sr, Ca, and Ti indicated by green, blue,

and gray circles, respectively. The (b) iDPC image shows the same unit-cell with oxygen indicated with red circles.

A HAADF and iDPC image at 15.3Mx of SL4 is shown in Figure 9.13. In the Figure 9.13(a), two complete STO layers and one complete CTO layer are within the field-of-view. In Figure 9.13(b) all cations and oxygen are visible. The oxygen columns in the CTO layer appear split much like in SL27, shown previously in Figure 9.6. The oxygen columns in the STO layer of SL4 almost all appear elliptical, with the columns closer to the interface between the STO and CTO more elliptical than those at the center of the STO layer. The octahedral tilt and distortions at the interface between the layers that was observed in SL27 also appears in SL4. To better understand the spatial extent of changing tilt-like angles, two positions were manually assigned to every oxygen column. For columns that were clearly separated, two well-separated positions were defined. For the columns that appeared almost symmetric the two positions were assigned as nearly identical so that the resulting measured angle was small. The results of manual column placement and the measured out-of-phase tilt-like angle are shown in Figure 9.14.

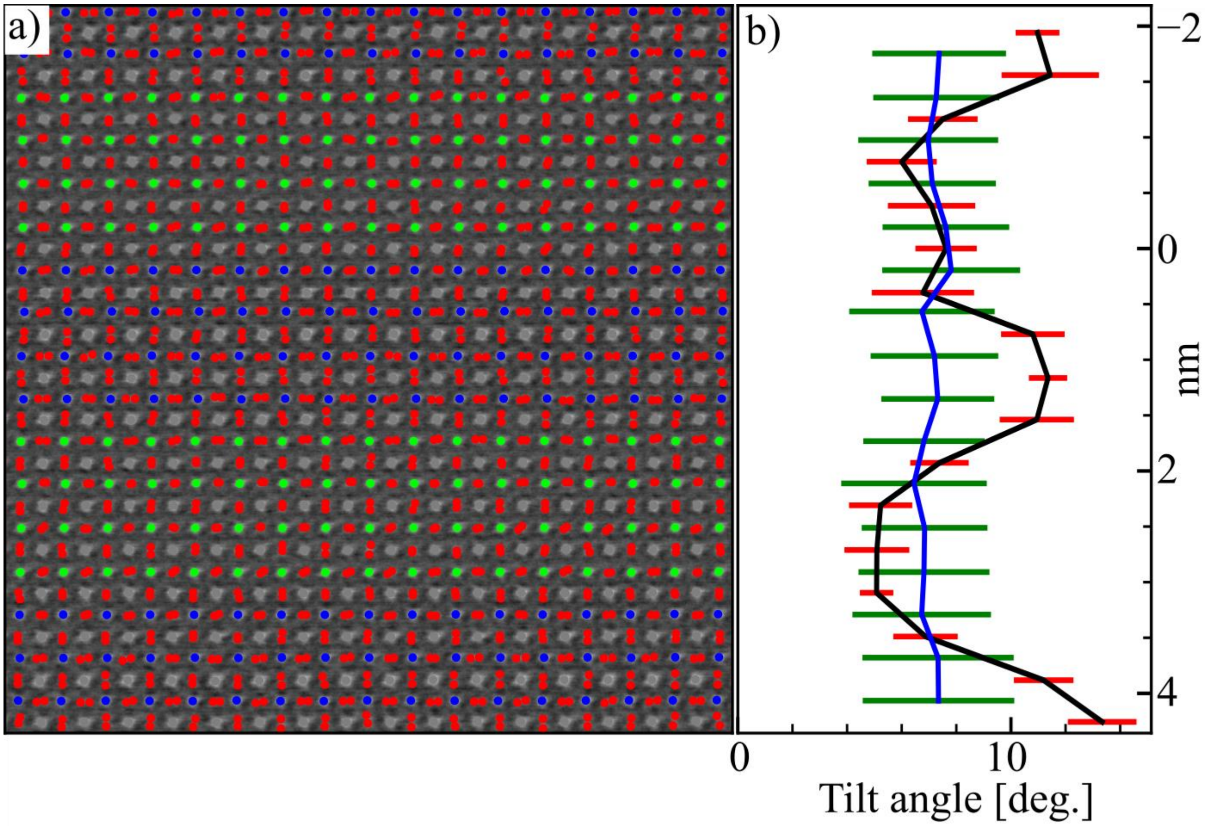

Figure 9.14. (a) iDPC image of SL4 with manually assigned column positions overlaid. (b) Average of the measured tilt angle from the (black) TiO_2 plane and (blue) AO plane. Red and green error bars represent the standard deviation within the plane. The zero on the y-axis indicates the chemically assigned TiO_2 interface plane between the first complete STO and CTO period.

Center-of-mass and Gaussian fitting was not used to refine the atom positions because these methods did not handle the proximity of the split columns well. Only out-of-phase angles were measured ($\measuredangle \mathrm{OTiO}/2$) since two positions were assigned per column. The out-of-phase tilt-like angle in the AO planes had a nearly constant value of 7.186^{o} on average and the angle in the TiO_2 planes was approximately sinusoidal with an average of 8.513^{o}, as shown in Figure 9.14(b). This sinusoidal pattern in octahedral titling appears similar to a spinodal gradient, as described in the Cahn-Hilliard equation (Cahn, 1961; Cahn & Hilliard, 1958). The sinusoidal variation in angle, or irregularity in oxygen displacement pattern, could be the origin for the diffuse intensity surrounding the ORs in SADP, as shown in Figure 9.2(b). The largest mean angle was in the top CTO layer and was 13.340^{o}. The central CTO layer, that was the only full CTO layer, had a maximum tilt angle of 11.358^{o}. Minima were present in the STO layers with the lowest mean being 5.080^{o}. The displacements within a TiO_6 octahedra have therefore extended into the STO layers with an out-of-phase tilt-like angle half of the CTO tilt angle but distinct layers exist.

The positions for split oxygen-positions is sensitive to the user manual placements and for the smallest splits it is difficult to assign two positions two a seemingly singular elliptical column. For these reasons, 2D Gaussians were fitted to each oxygen column as in Section 9.1. The results are shown in Figure 9.15 as a vector image and line profile of the (001) plane ellipticity and in Figure 9.16 as a color map of the ellipticity.

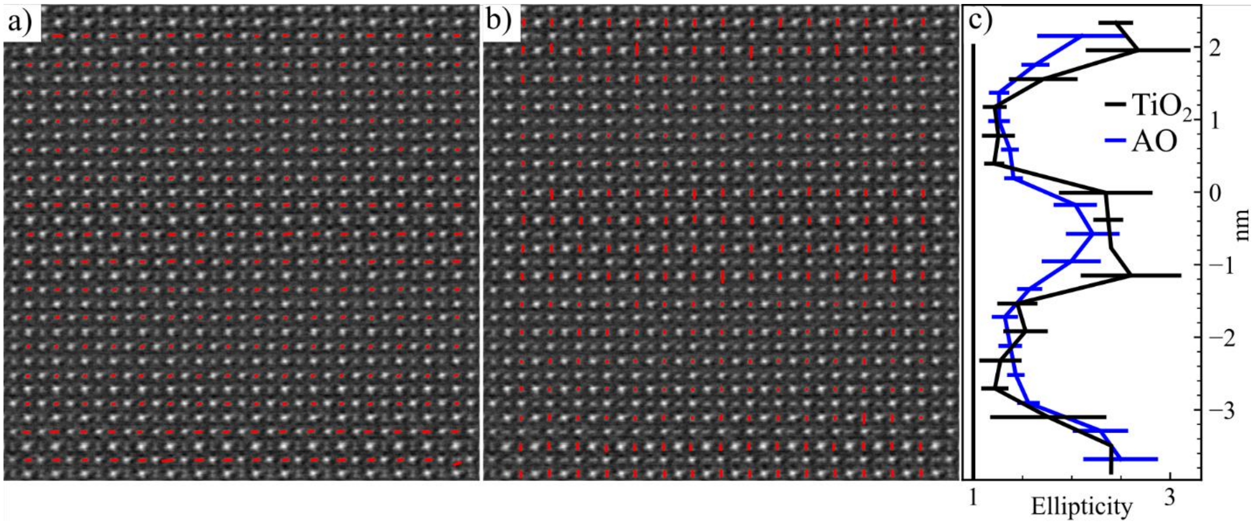

Figure 9.15. iDPC image of SL4 with a vector overlay representing the ellipticity of columns in (a) AO and (b) TiO_2 planes. (b) a line profile showing the mean and standard deviation of ellipticity within an (blue) AO (black) TiO_2 plane. The zero on the y-axis indicates the chemically assigned TiO_2 interface plane between the first complete STO and CTO period.

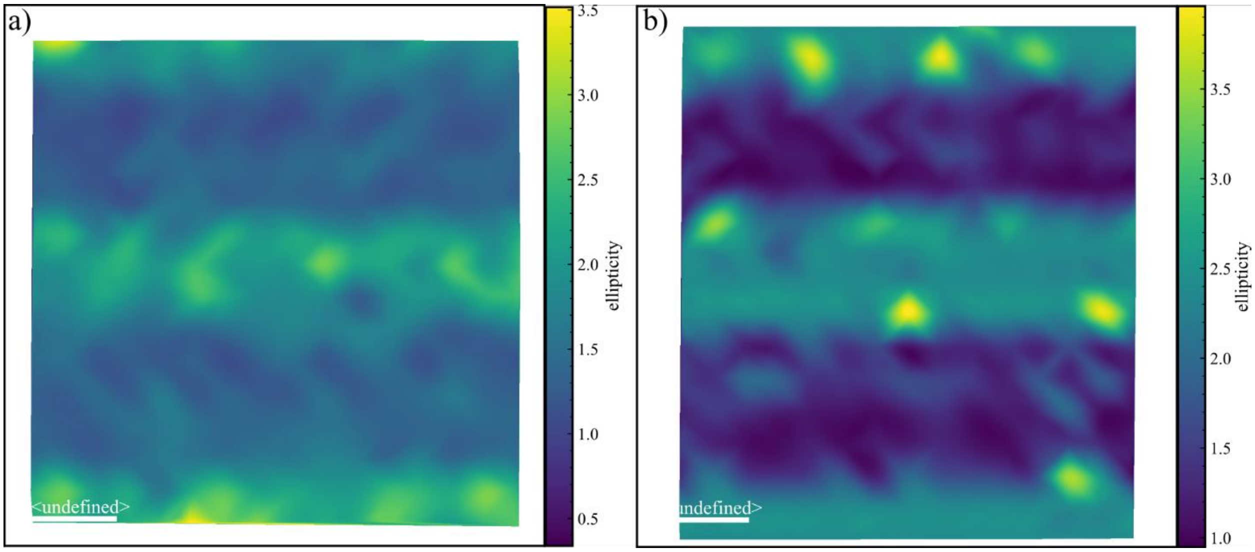

Figure 9.16. Ellipticity measurements for split O columns in (a) AO and (b) TiO_2 planes of SL4.

The ellipticity in the TiO_2 planes was sinusoidal much like the direct out-of-phase tilt angle measurements. The ellipticity in the STO layers of SL4 was near the same benchmark values of SL27. However, observation of the iDPC images by eye clearly showed ellipticity in SL4 that was not present in SL27. The fitting and ellipticity might be skewed by neighboring cations. Therefore, the ellipticity measurements are best used for a qualitative trend in TiO_6 tilting and it is best to not try to calibrate the ellipticity measurements with measured tilt angles unless the cation column intensity is first fitted and removed. This removal was not possible in these iDPC images because the columns often had a four-fold symmetry and therefore a subtracted Gaussian would still leave residual intensity. Overall, the same sinusoidal pattern of octahedral tilt was observed in the TiO_2 planes. In addition to the ellipticity parameter that is related to an out-of-phase tilt-like displacement pattern the direction of ellipticity is shown in Figure 9.15 as a rotation of the ellipticity vector. Rotations within the TiO_2 and AO planes are minimal but systematic from plane to plane. This suggests that the displacement of oxygen atoms is not simply a rigid body rotation of the TiO_6 octahedra but rather a rotation and distortion.

The results from measuring the out-of-phase tilt angle in SL4 was vastly different than SL27. To begin, the STO layer of SL27 did not have out-of-phase tilting, that was shown by single non-elliptical atomic oxygen columns. Only the first and arguably second SrO layer(s) near the STO/CTO interface had titling because of coupling between the layers. In SL4 the STO layers always had some degree of out-of-phase tilting from coupling to the CTO layers and the minimum tilt angle of 5.080^o in the TiO_2 planes was approximately half of the tilt angle of CTO in SL27. The maximum in the CTO layers of SL4 was at approximately the same tilt angle as in SL27. This suggests that as the layers become smaller and approach the length scale of the structurally diffuse interfaces observed in SL27, then the STO layer preferentially loses its original “bulk like” characteristics. The preferred tilt accommodation of STO was also seen in the ellipticity measurements of SL27 where the ellipticity decayed over two SrO planes compared to one CaO plane. At this point we do not want to speculate the origin of the preferential tilting in STO over CTO, but will do so later in Section 9.3 where a comparison of

SL2, SL4, and SL27 is presented. This result shows that the layers of the SL are converging to a singular tilt pattern, much like the 4D-STEM results.

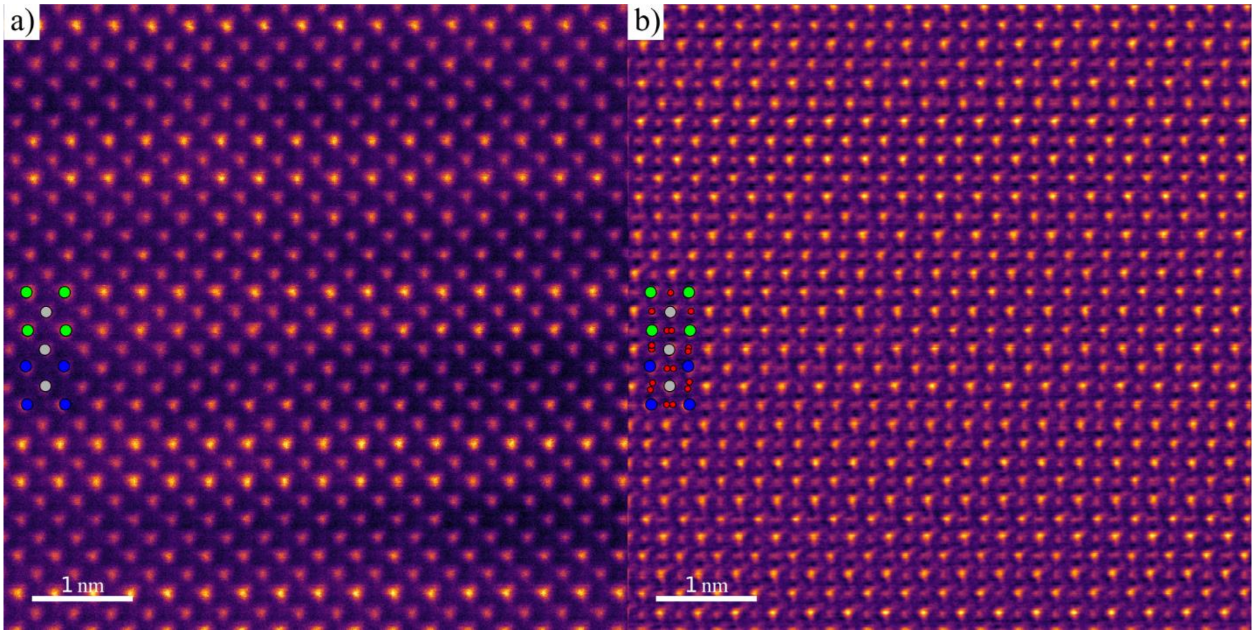

Figure 9.17. False color: (a) HAADF and (b) iDPC image taken at 15.3Mx of SL2. In (a) one unit-cell is illustrated on each side of the interface with Sr, Ca, and Ti indicated by green, blue, and gray circles, respectively. The (b) iDPC image shows the same unit-cell with oxygen indicated with red circles.

A HAADF and iDPC image at 15.3Mx of SL2 is shown in Figure 9.17. In the Figure 9.17(a) , three complete STO layers (bright layers) and four complete CTO layers (dark layers) are within the field-of-view. In Figure 9.17 (b), all cations and oxygen are visible. The oxygen columns in both CTO and STO layers appear elliptical much like in SL4. To better understand the spatial extent of changing tilt angles, two positions were manually assigned to every oxygen column in the same manner as SL4. The results of manual column placement and the measured out-of-phase tilt angle is shown in Figure 9.18.

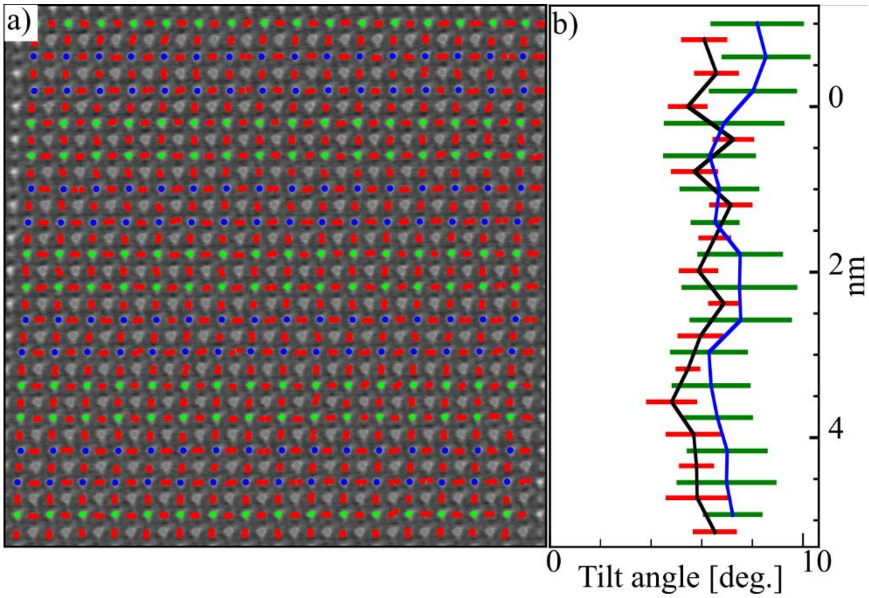

Figure 9.18. (a) iDPC image of SL2 with manually assigned column positions overlaid. (b) Average of the measured tilt angle from the (black) TiO_2 plane and (blue) AO plane. Red and green error bars represent the standard deviation within the plane. The zero on the y-axis indicates the chemically assigned TiO_2 interface plane between the first complete STO and CTO period.

The out-of-phase tilt-like displacements were quantified using the same procedure in SL4 and the results for the mean value per (001) plane are shown in Figure 9.18(b). Unlike SL4, little layer to layer variation is observed in either the AO or TiO_2 planes. A small sinusoidal variations with a four unit-cell (one period) wavelength could be argued in the TiO_2 planes, that is the central TiO_2 plane of a layer being extrema and the interface TiO_2 planes as zero-nodes, but the variation is small compared to the other SLs and is verging on the measurement error. The mean value was 7.138^o and 6.096^o in the AO and TiO_2 planes, respectively. This is nearly the same as the average tilt angle in the AO planes of SL4 and the interface tilt angle in the TiO_2 planes of SL4 and SL27. Thus, it appears that the entire structure of SL2 has adopted the structure of the proposed interface structural unit in the larger SLs. In other words, the SL no longer consists of structurally distinct phases but is a single chemically ordered phase.

For consistency ellipticity measurements were performed using the previously described methods. The results are shown in Figure 9.19 as a vector image and line profile of the (001) plane ellipticity and in Figure 9.20 as a color map of the ellipticity.

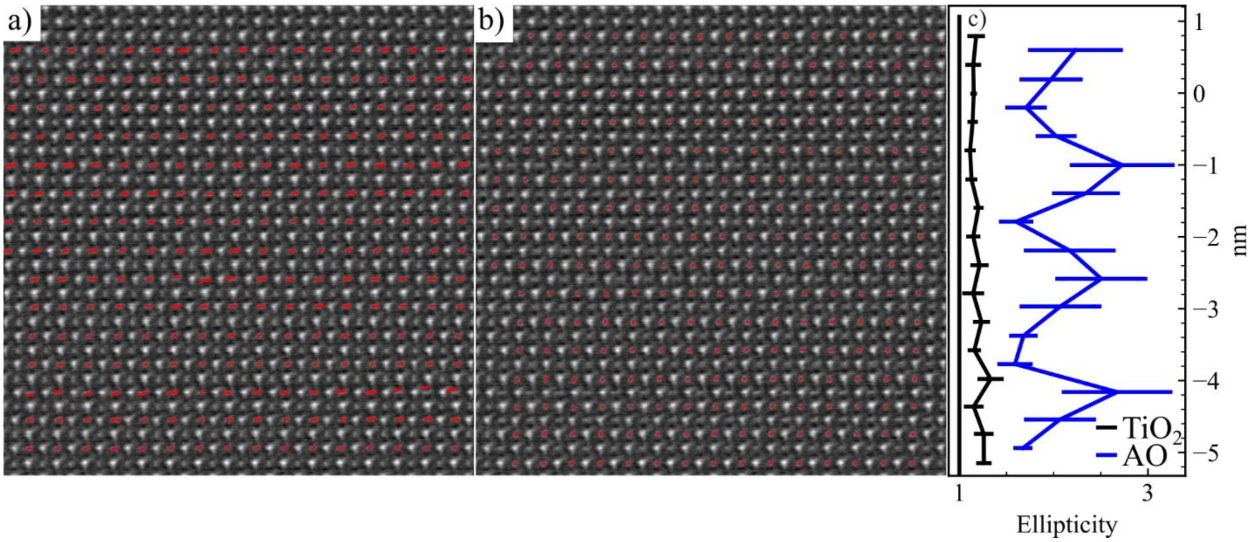

Figure 9.19. iDPC image of SL2 with a vector overlay representing the ellipticity of columns in (a) AO and (b) TiO_2 planes. (b) a line profile showing the mean and standard deviation of ellipticity within an (blue) AO (black) TiO_2 plane. The zero on the y-axis indicates the chemically assigned TiO_2 interface plane between the first complete STO and CTO period.

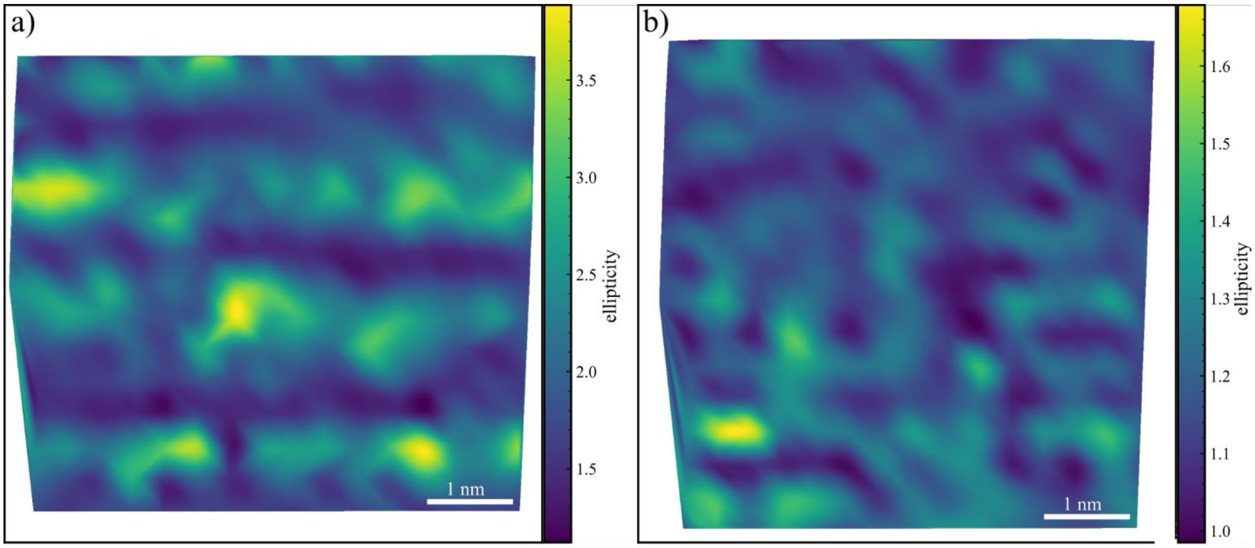

Figure 9.20. Ellipticity measurements for split O columns in (a) AO and (b) TiO_2 planes of SL4.

No variation in ellipticity was measured in the TiO_2 planes and some ellipticity was measured in the AO planes. This is the opposite of the manually measured tilts in Figure 9.18(b) where the TiO_2 planes had a minimal variation and the AO had none. This is thought to result from fitting to the tails of cation columns in the AO layers. The sinusoidal variation of ellipticity follows the same periodicity of the SL with minima in the CTO layer and maxima in the STO layer. If tilting were the result of this trend, then one would expect that the atoms in the STO would be less elliptical than in the CTO layers. Instead, the trend follows the A-site intensity suggesting fitting errors as the origin in ellipticity variations. It is suggested that only samples with uniform intensity providing a consistent skew in ellipticity, or the removal of cation site intensity through

2D-Gaussian subtraction of Gaussian columns to remove the skewing entirely, are used if ellipticity is used for a measure of out-of-phase tilting.

In this subsection the SADP from the $[010]_{pc}$ showed that SL2 and 4 had ordered octahedral tilts. Unlike in SL27, the in-phase tilt axis was in the growth direction and SL normal with only one orientation of the crystal present (i.e. no domains). SADP taken from the two in-plane $\langle 110\rangle_{pc}$ ZAs further refined the possible space group of the lattice to either $P2_1/m$ or Cmcm and not Pbnm, however some discrepancies were found with both $P2_1/m$ and Cmcm so the exact space group was not determined. With the $[010]_{pc}$ and $\langle 110\rangle_{pc}$ ZAs it was concluded that SL4 had both ordered in- and out-of-phase tilt axes. Tilt angle measurements in iDPC images showed that SL4 had a sinusoidal variation in its out-of-phase tilt-like displacements structure in AO planes. The average tilt angles in SL4 were 7.186^o and 8.513^o in the AO and TiO_2 planes, respectively. The tilt angles in SL2 were consistent through the entire SL with average angles of 7.138^o and 6.096^o in the AO and TiO_2 planes, respectively. This showed that as the number of unit-cells in a SL layer decreases the system transitions from bulk layers separated by interface to a system dominated by interfaces lacking bulk-like character, to a singular chemically ordered phase with a structure like the structural units in the larger period SLs. The average tilt anlges are near to the interface values observed in SL27, also showing structural distortion converge to the structure of an interface in larger period SLs. The iDPC results connect the large field-of-view SADP observations with atomically resolved structural information. All techniques point to the convergence of structure to a “happy medium”.

9.3 “Where is the Interface?”: A Comparison of SL2, SL4, and SL27

Before continuing to SL1, we should consider where or what the interface and bulk like layers are in the previously shown SLs. This is an interesting scientific question because the choice of interface depends on whether you consider only chemistry, displacements, or both. It also is stringent on whether proper conventions for an interface are chosen or if the most representative but non-conventional interface is chosen.

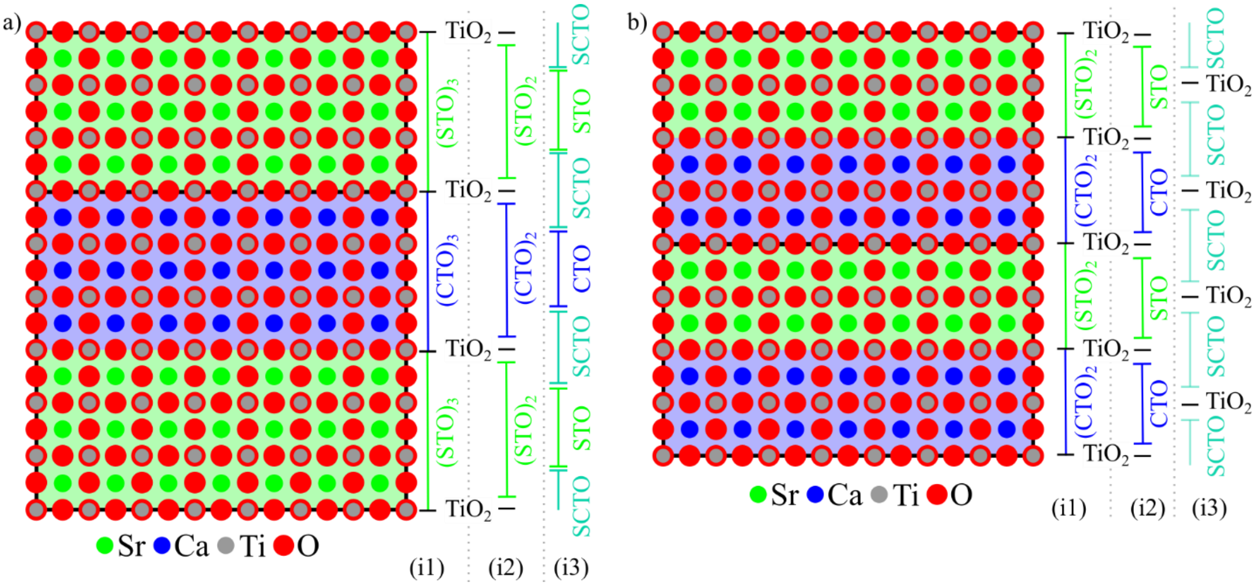

Figure 9.21. Schematic of SLs with (a) *n*=3 and (b) *n*=2 unit-cells per layer. Three series are shown that represent different choices in interface. (i1) $(CTO)_n - (STO)_n$ has ATO layers that share a TiO_2 interface plane. (i2) $(CTO)_{n-1} - TiO_2 - (STO)_{n-1}$ follows the convention of an interface not intersecting atoms and results in an interface TiO_2 plane that does not belong to either ATO layer. (i3) demonstrates a choice of interface where every atom in a layer has an ideal first nearest like neighbor (i.e. the ideal atom within a sublattice or the third nearest neighbor in the ATO_3 unit-cell).

Figure 9.21 shows a projection of a SL with *n*=3 and *n*=2 "unit-cells per layer" and three series with different choices of interfaces. The superlattices throughout the thesis are described by repeating $ATiO_3$ simple cubic unit-cells centered such that Ti atoms occupy the corners sites and A atoms occupy body centered positions. In this description the SL layers are terminated by TiO_2 planes that belong to both the STO and CTO layers. This choice of interface, for a chemically abrupt SL that lacks structural distortions around the interface, is indicated in Figure 9.21 series (i1) by horizontal black lines. The SL is a series of $(CTO)_n - (STO)_n$ repeat units with the TiO_2 interface being partially contain in CTO and part in STO. This does not follow the correct convention of an interphase interface. Conventionally an interface is chosen so that it does not intersect atomic planes as in (i1). If we choose to hold with convention and place the interface between two planes that chemically see different neighbors than expected in the bulk of a material, then we can place the interface between the TiO_2 interface described in (i1) and either bounding AO plane. Note, that not one of these choices of interfaces can be chosen, but both must be since the TiO_2 plane dividing the chemically distinguishable A-sites sees different neighbors above and below than expected in CTO and STO, therefore excluding it from either phase. This is illustrated in (i2) where the same choice of a TiO_2 layer is chosen with the interfaces defined above and below the plane. Series (i2) differs from (i1) in that the bulk ATO layers have *n*-1 unit-cells divided by a 2-dimensional TiO_2 plane. The third option is to define a

SCTO ($Sr_{0.5}Ca_{0.5}TiO_3$) structural unit as the interface. This choice of interface is distinguishable because every atom sees its ideal first nearest like neighbor. This is equivalent to saying every atom sees the ideal nearest neighbor within its sublattice or third nearest neighbor in the full ATO_3 basis. In series (i1) and (i2) both SL2 and SL3 have distinguishable ATO layers, however (i3) has distinguishable ATO layers in SL3 and loses this bulk like ATO structure in SL2. Thus, when an interface is defined by (i3) there is a minimum number of unit-cells to define a SL, $n \geq 3$, otherwise the material is a singular phase consisting of structural units that defined the interface in larger SLs. In the larger SLs the series is $(CTO)_{n-2} - Sr_{0.5}Ca_{0.5}TiO_3 - (STO)_{n-2}$. This describes three very distinct choices of interface(s) that are purely dependent on the chemical species present and not to displacements in the structure.

We begin by considering the structural distortions in SL27. In SL27 there were distinguishable tilt patterns in STO and CTO, with STO having no tilt and CTO having out-of-phase tilting as in their bulk like phases. There were three planes at the interface, CaO-TiO_2-SrO that had tilting or a displacive pattern that was different than in the bounding SL layers. This can be considered as a local coupling and structural accommodation of the STO and CTO tilt patterns. The CaO-TiO_2-SrO series is identical to the choice of interface in series (i3), as shown in Figure 9.21. Therefore, a $Sr_{0.5}Ca_{0.5}TiO_3$ layer describes the structural and chemical nature of the interface unlike the singular TiO_2 interface in (i1) and (i2).

We now consider SL4, where a sinusoidal variation of out-of-phase tilt-like displacements were present. SL4 is only one unit-cell per layer larger than the schematic shown in Figure 9.21. In a SL with *n*=3 unit-cells per layer the choice of (i3) presents a series of layers each containing one ATO_3 unit-cell. It would therefore make sence that if the displacement structure of SL27 carried to the smaller SL4 that the tilt angles would appear sinusoidal, as they do. The choice of interfaces in series (i3) thus seems to again be the best fit for the chemical and structural interface. One unique thing about SL4 is that the STO does not have zero out-of-phase tilt-like displacements, but rather all columns appear elliptical therefore having some type of displacement pattern along the projected direction.

Lastly, we can consider SL2 where the manually placed positions showed that the out-of-phase tilt-like displacements were constant throughout the entire SL structure. Examining series (i3) in Figure 9.21(b) shows that the entire structure consists of SCTO “interface” structural units divided by TiO_2 planes. The distinguishability between the TiO_2 planes and the SCTO units is ambiguous. Rather than defining each separately, the two could be combined into a single $SrCaTi_2O_6$ unit-cell that repeats throughout the entire structure. The reason that the displacement structure remains relatively constant through the entire SL can be attributed to the SL being a singular chemically ordered phase.

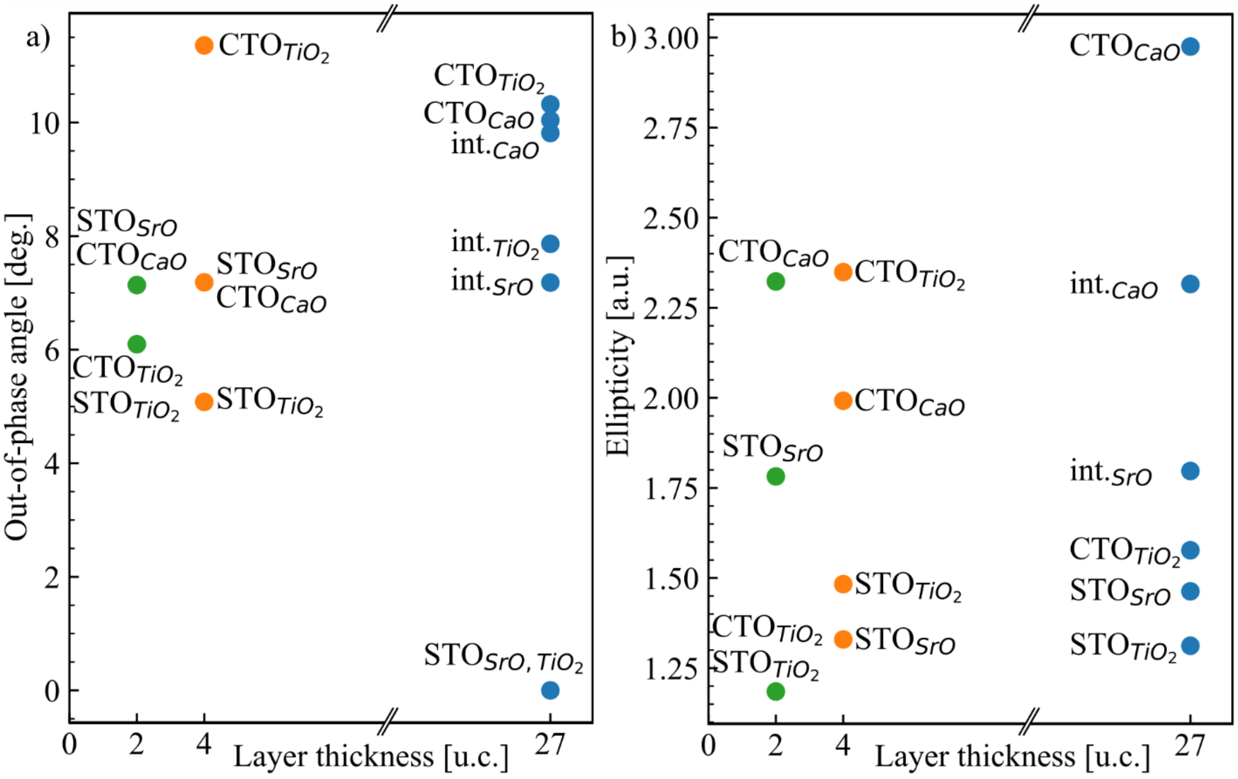

Figure 9.22. (a) Measured out-of-phase tilt-like angles in each plane of SL2, SL4, and SL27. In general the angle converged to the angle of the interface (int.) plane as the number of unit-cells per SL layer decreased. (b) Measured ellipticity in each plane of SL2, SL4, and SL27. Altogether the ellipticity lacked a trend across the SL series.

Figure 9.22 compares the directly measured angle and the ellipticity of the out-of-phase tilt-like displacements as a function of unit-cells per SL layer. SL27 showed three distinct regions of tilt that are classified into the STO, interface, and CTO regions. In terms of the (i3) series the same regions are STO, SCTO, CTO. SL4 had three distinct regions. The SrO plane in STO and the CaO plane in CTO were at 7.186° which is near the same tilt angle as the interface planes in SL27. This tilt angle is not exactly halfway between the 0 and 10.04° tilt angles measured in the bulk like layers of SL27 but is skewed toward the CTO's larger tilt angle. The same is seen in SL27 where the SrO plane was at 7.186° and the CaO plane was at 10.04° compared to the 0 and 10.04° tilt angles measured in the bulk CTO and STO layers, respectively. This shows a tendency for the STO to distort more than the CTO relaxes. If we consider that the origin of tilting is bonding and the Ca is more covalent and therefore has stronger bonding than we can postulate that the stronger bonding present in CTO than in STO might be responsible for the skewed "happy medium". We can also look at the temperature stability of the phases for STO and CTO. STO is tilt free above ~150 K and has out-of-phase tilting below ~150 K. CTO lacks tilting above ~1374 K and transitions to a phase with out-of-phase tilting below ~1374 K and takes on another out-of-phase tilt axis and an in-phase tilt axis below ~1250 K. The higher and wider temperature range of CTO would suggest that the tilting is more stable in CTO than in STO. The bonding and temperature ranges can be loosely considered as the enthalpic and entropic stability of the tilting. Tilting in CTO appears more stable in both cases, which explanes why experimentally the CTO had a smaller deviation from the bulk at the interface than STO and why the angle was 7.186° and not closer to 5.02° (i.e. the average of the bulk tilts). SL2 continued the trend of convergence with only two distinct tilt angles present, in TiO_2 and AO planes.In this subsection, three choices of interface(s) were described for a SL that did not have structural distortions. It was then shown that the choice of a SCTO structural unit at the interface described both the chemical and structural nature of the interfaces. Comparing the series of SLs, it was found that the SCTO structural unit that was well separated by bulk ATO layers in SL27 was the predominant structure in SL4 and the entire structure in SL2. Thus as the number of unit-cell per layer decreased the SL transitioned from a system of bulk ATO layers separated by interfaces (SL27) to a system predominantly consisting of interfaces (SL4) to a system with a singular phase characteristic of the prior interface structure. The tilt angle converged to a value between the two bulk like phases' tilt angles as the interface structure predominated. The angle was skewed toward the tilt angle of CTO which was concluded to result from the higher stability of tilting in CTO than STO.

9.4 SL1: A Modulated Antiparallel Displacements

In the SADP of the one unit-cell CTO-STO superlattice, as seen in Figure 9.23, ORs were present at both ½$[120]_{pc}$ and ½$[210]_{pc}$ positions, or more generally, at ½$(oee)_{k\neq l}$ and ½$(eoe)_{h\neq l}$. This is the SADP expected if one domain of Pbnm-CTO had its c-axis aligned with the films normal and one aligned in-plane (perpendicular to the viewing direction). However, it is not possible for the CTO layer to have a c-axis of $2a_{pc}$ aligned with the film normal because a one unit-cell superlattice has a layer thickness of a_{pc}. The ½$(oee)_{k\neq l}$ therefore indicates that the superlattice "on the whole" has taken on a periodicity of its own and can be considered as a single lattice with chemical ordering on the A-sublattice. The ½$(eoe)_{h\neq l}$ ORs also indicate that the unit-cell has doubled in the plane of the film. Taken together, the ½$(oee)_{k\neq l}$ and ½$(eoe)_{h\neq l}$ ORs indicate that the unit-cell doubling in the viewing direction was $2a_{pc} \times 2a_{pc}$, which does not prescribe to a space group of either monolithic constituent.

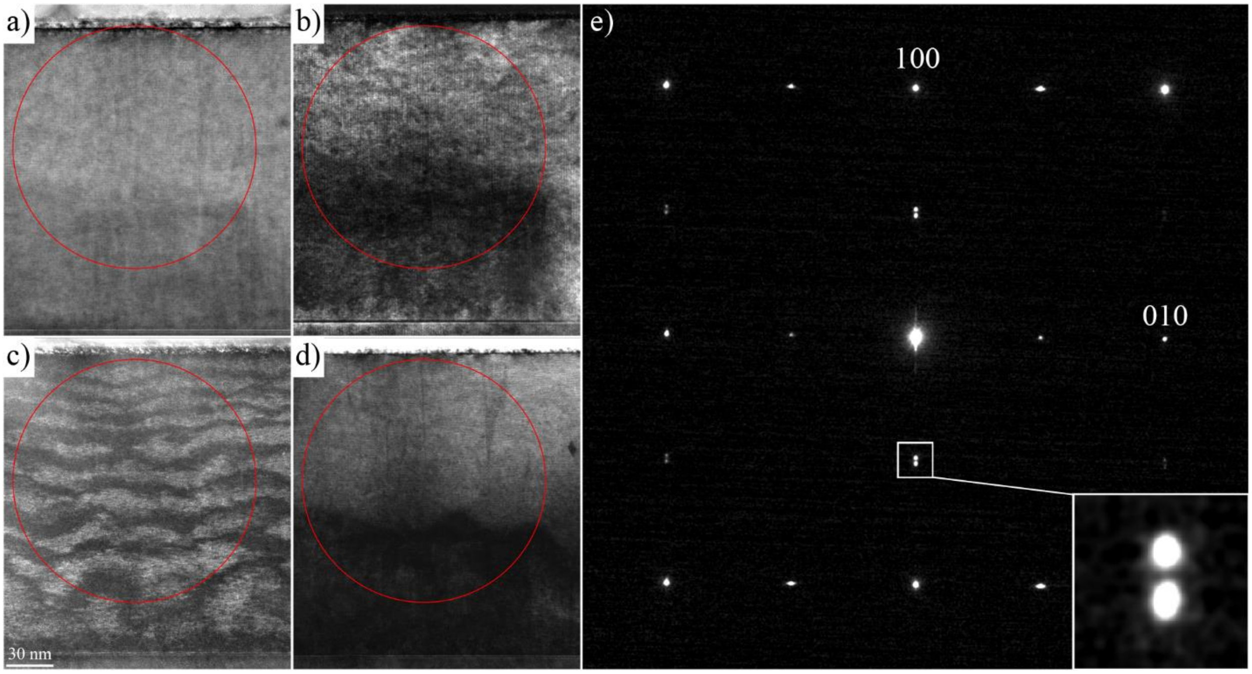

Figure 9.23. Bright-field images formed: (a) without and (b) with an objective aperture. The modulated structure was observed in the ½(100) dark-field image in (c), but is not present in either bright-field image or the (100) dark-field image in (d). (e) The [001] ZA SADP had ½(100) and ½(010) OR. The inset in (e) is an enlargement of the split ½(100) Bragg peak which resulted from the modulated displacement amplitude normal to the film.

On closer examination of the ORs, all ½(oee)$_{k\neq l}$ peaks were split into two peaks (see inset of Fig. 1(e)). Splitting was not necessarily along the $[100]_{pc}$ growth direction. To identify the origin of this splitting, axial dark-field imaging was performed with ½$(100)_{pc}$ OR. The resulting dark-field image, seen in Figure 9.23(c), exhibits a modulated intensity that was nearly faceted in appearance. The average wavelength of modulations, directly measured along the film thickness, was 15.6 nm. This distance is nearly equal to the reciprocal-space distance between the maxima of the split OR, which was measured to be 0.064 nm^{-1} or λ=15.625 nm. We also note that split peaks had a x-shaped diffuse background which we attribute to the faceted "fine structure" in the modulations. Further examination of the SADP accompanied by additional dark- and bright-field imaging support this conclusion. For example, the $[010]_{pc}$ peak was broadened but not split (see Figure 9.23(e)). Furthermore, the modulations were not observed in the bright-field image either with or without an aperture, as shown in Figure 9.23 (a,b). Neither were they observed in a dark-field image formed with the (001) fundamental Bragg reflections, as shown in Figure 9.23 (d). Taken together, we therefore conclude that the splitting of the ½(oee)$_{k\neq l}$ peaks is therefore a consequence of a real-space modulation in the periodicity of the superlattice as a whole along the growth direction.

Modulations in the dark-field images like those observed in Figure 9.23 (c) have been observed in other oxide systems and attributed to competition between soft modes (Anderson et al., 1992; Borisevich et al., 2012; Marrec et al., n.d.; Rondinelli & Fennie, 2012; Salje, 2012; Yamamoto et al., 1990). This competition can arise owing, at least in part, to the influence of the substrate atop of which the oxide forms, in a templating like effect (Biegalski et al., 2015; Borisevich et al., 2012; Middey et al., 2018; Moore & Howe, 2000). For example, patterning of substrates has been linked to the initialization of similar modulations in other oxide systems. Here, the constant dark band nearest to the NGO substrate, as seen in Figure 9.23(c), is different to the rest of the structures wavy pattern. This, in turn, suggests that the modulations are either constrained, or initialized, by the substrate.

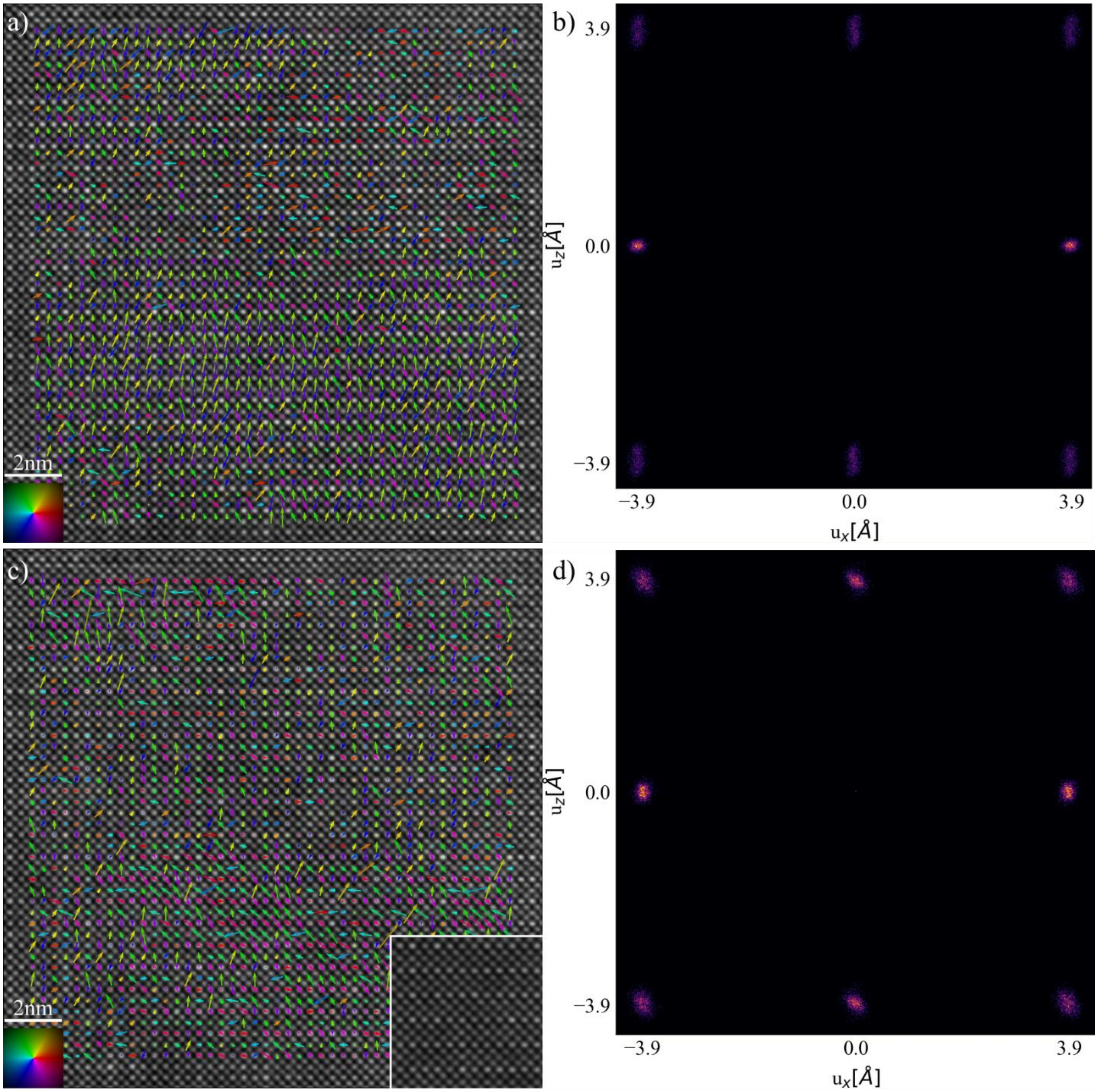

Figure 9.24. HRTEM image with overlaid displacement vectors for the: (a) Ti-sublattice and (c) A-sublattice. The n.l.n. distribution [100] was streaked along: (b) [100] in the Ti-sublattice, and (d) $[1\bar{1}0]$ in the A-sublattice. The inset in (c) shows a magnified region of the superlattice with layered A-site ordering.

To identify the origin while simultaneously assessing the implications of the long-range order implied by the observed dark-field modulations, high-resolution TEM (HRTEM) images were acquired as shown in Figure 9.24(a,c). Contrast variations in these images show a superlattice that is chemically well ordered. Thus, we conclude chemical variation is not the cause of the observed modulations. Rather, variations in the lattice positions themselves can be linked to the modulations. To support this claim, the position of atomic columns in the images of Figure 9.24(a,c) were located by finding intensity maxima then refined via fitting to 2D Gaussian functions. Using the fitted positions and known periodicity of the lattice, the A- and Ti-sites were then separated into sublattices for further analysis. Distances to the eight nearest-like-neighbor (n.l.n.) were calculated resulting in the distributions shown in Figure 9.24(b,d) for the Ti- and A-sublattices, respectively. Upon examination, the first n.l.n cluster for the Ti-sublattice at $\{110\}_{pc}$, $[100]_{pc}$, and $[\bar{1}00]_{pc}$ were bimodal. This bimodal nature is similar to that observed for the ½$(oee)_{k\neq l}$ OR splitting observed in the SADP (seen in Figure 9.23(e)). The bimodal structure in the n.l.n. cluster showed that two distinct distances existed along [100] suggesting systematic displacements in the cation sublattices.

To investigate, the ideal center of each column was calculated by averaging the n.l.n. distribution, whereupon displacement of each column was calculated subtracting the actual and the ideal center positions. This value was converted to a complex number that is indicative of the magnitude and angle of lattice displacements. These displacements are overlaid on the HRTEM image in Figure 9.24(a,c) as arrows, with the bivariate colormap indicating the magnitude and angle of displacements. The resulting bivariate displacements show the emergence of antiparallel displacements in the one unit-cell CTO-STO superlattice. Similar observations can be found in naturally ordered perovskites and one unit-cell PTO-STO superlattices which display hybrid improper ferroelectricity (Bousquet et al., 2008; Pitcher et al., n.d.; Rondinelli & Fennie, 2012). Hybrid improper ferroelectricity results from the competition of octahedral rotations in two non-equivalent tilt systems, much like STO and CTO. The possible hybrid improper ferroelectric behavior observed here, however, is starkly differentiated from these other systems, because neither CTO nor STO naturally exhibit ferroelectric or anti-ferroelectric properties on room temperature and pressure.

The displacements in the Ti-sublattice fell into two characteristic regions: i) areas comprised of antiparallel displacements along $[100]_{pc}$ (green/yellow to purple/blue), and ii) regions with slightly more disorder and a general pattern of alternating displacements 90° out of phase (red to yellow/green or blue/purple). The same regions in the A-sublattice had systematic displacements categorized as: i) anti-parallel displacements along $[1\bar{1}0]_{pc}$ (green to pink), and ii) regions with more disorder. The HRTEM results demonstrate that regions of A- and Ti-sublattice displacements, and other regions without observed displacements, are responsible for the modulated structure observed in the dark-field images Figure 9.23). Therefore, the one unit-cell CTO-STO superlattice had modulated antiparallel displacements.

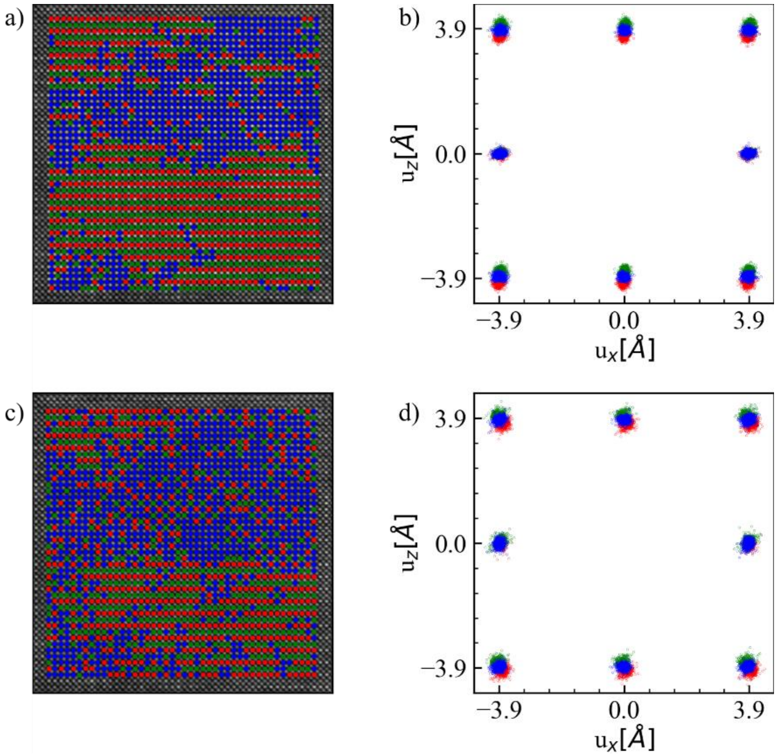

Figure 9.25. K-means clustering of n.l.n. in the: (a) Ti and (b) A sublattices. Antiparallel displacements (green and red) and non-displaced (blue) regions are present.

To further categorize the displacement patterns observed in the lattice, K-means clustering was performed on the n.l.n. distribution. The results for the Ti- and A-sublattice n.l.n. using three clusters are shown in Figure 9.25(a,b) and Figure 9.25(c,d), respectively. For further information on the choice of three clusters and the effect of cluster number, the reader is referred to the supplemental Section S1. The region causing the bimodal distribution of $[100]_{pc}$ first n.l.n. was from the same area that had antiparallel displacements observed in Figure 9.24(a, c). The green and red clusters are equally split about $[100]_{pc}$, $[\bar{1}00]_{pc}$, and $\langle 110\rangle_{pc}$ in both sublattices. In the Ti-sublattice, the red and green clusters are from n.l.n. displaced along $[100]_{pc}$ and $[\bar{1}00]_{pc}$, respectively, and these co-exist within a single region as alternating layers. The same behavior was observed in the A-sublattice, with green and red n.l.n. clusters displaced along $[2\bar{1}0]_{pc}$ and $[\bar{2}10]_{pc}$, respectively. This supports the conclusion that there are regions of antiparallel displacements. The blue clusters correspond to atomic columns that do not have displacements in the observed projection, and these spatially separate the antiparallel displaced areas. This showed that K-means clustering with three clusters had two characteristic regions: one with antiparallel displacements, and another without displacements, further demonstrating the spatial variation and antiparallel displacements of the one unit-cell CTO-STO superlattice.

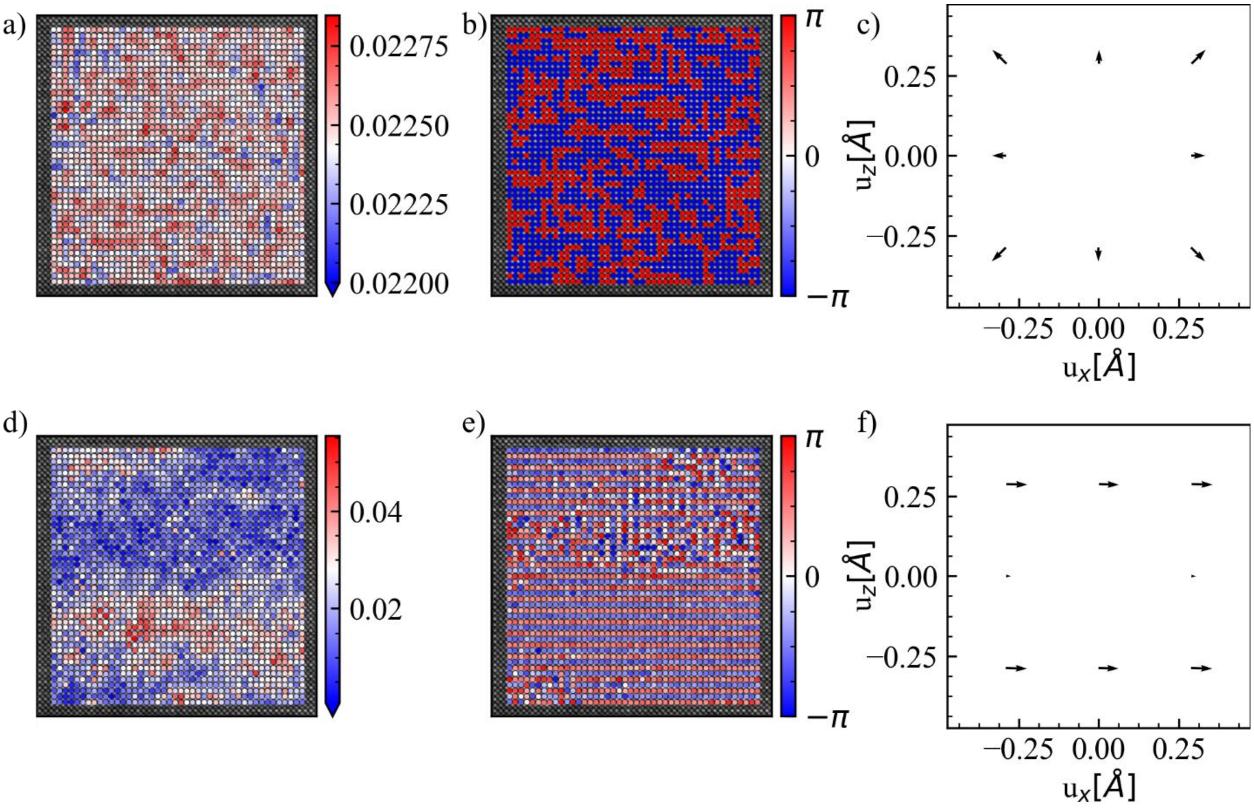

Figure 9.26. (a-c) Component 1, and (d-f) component 2 of SVD performed on the complex valued n.l.n. list in the Ti-sublattice. The (a,d) magnitude and (b,e) phase of the complex value loading along with (c,f) eigenvector displacements showed a displacement along the pc axes for component 1 and grains with anti-parallel displacements along $[100]_{pc}$ for component 2.

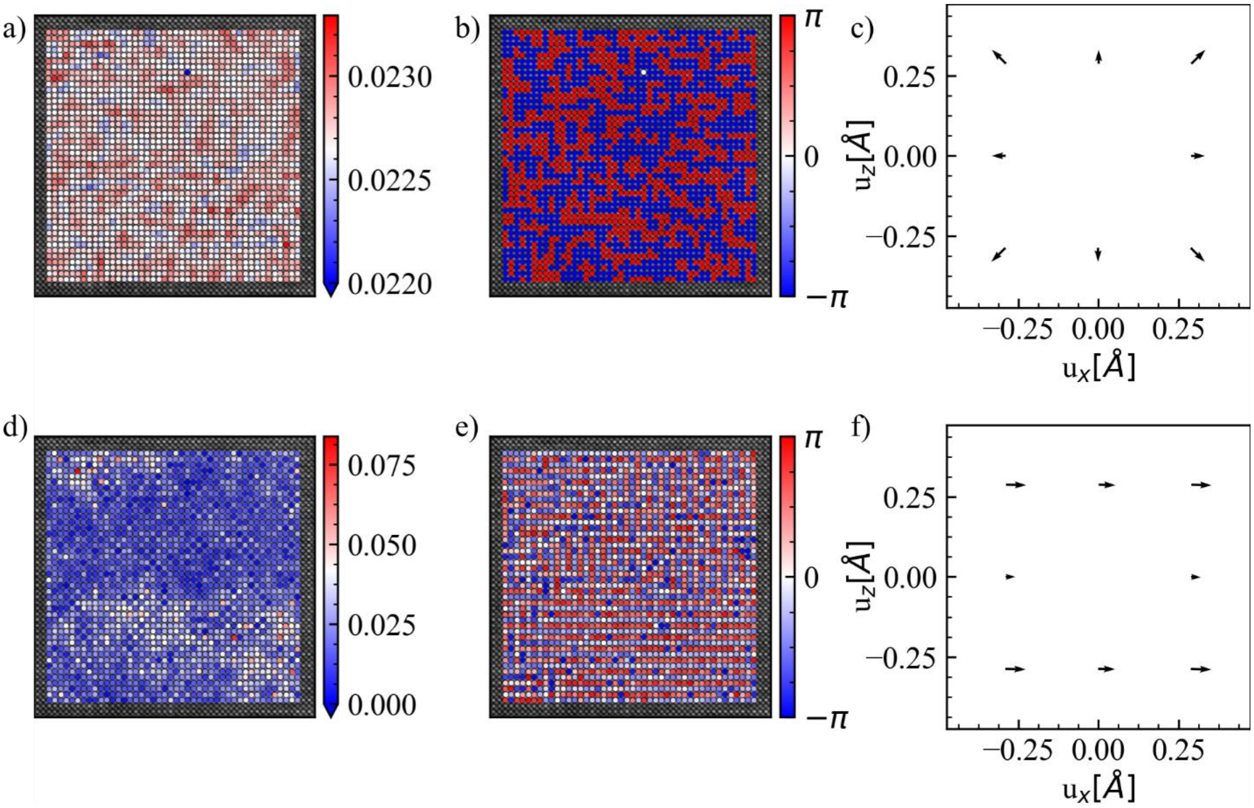

Figure 9.27. Component (a-c) 1 and (d-f) 2 of SVD performed on the complex valued n.l.n. list in the A-sublattice. The (a,d) magnitude and (b,e) phase of the complex value loading along with (c,f) eigenvector displacements showed a displacement along the pc axes for component 1 that were similar to component 1 and grains with anti-parallel displacements along $[1\bar{1}0]_{pc}$ for component 2.

The interpretation of K-means clustered n.l.n. displacements is straight forward; however, its discrete nature does not portray the diffuse nature of the modulated structure observed in Figure 9.23. Multivariate analyses, such as SVD, are non-discrete and capable of separating such features. Hence, SVD was implemented to further analyze this feature. SVD was performed on the n.l.n. data with each n.l.n. represented as a complex value relative to the central atomic column (i.e., containing relative distance and angle from an atomic column to its n.l.n.). The first two components of SVD performed on the n.l.n. displacements in the Ti-sublattice and A-sublattice are shown in Figure 9.26 and Figure 9.27, respectively. (An explanation of the SVD is found in the supplemental Section S3 along with an extension up to four components.) The loadings and eigenvector displacements were remarkably similar for the two sublattices. The eigenvector displacement of component 1 (Figure 9.26(c) and Figure 9.27(c)) showed an isotropic displacement of all eight n.l.n. along the pc axes. The angle of the loading (Figure 9.26(b) and Figure 9.27(b)) had a value of ±π. Since phase shifting a four-fold pattern 90° maintains the same pattern, component 1 does not contribute to an angular displacement. The magnitude of the loading (seen in Figure 9.26(a) and Figure 9.27(a)) did change from position to position so the main contribution of component 1 was a spatially varying dilation of the lattice along the pc axes. Component 2's eigenvector displacement (Figure 9.26(f) and Figure 9.27(f)) was one fold, indicating a linear displacement of the sublattices in a single direction. The magnitude of the loading (Figure 9.26(d) and Figure 9.27(d)) exhibited two regions with characteristic displacements similar to the observation in Figure 9.25(a, c). The regions of vertical antiparallel displacement of the Ti-sublattice in Figure 9.24(a) are the same areas with the largest magnitude of displacement in Figure 9.26(d). Likewise, the region with more random character in Figure 9.24(a) had the smallest magnitude of displacement in Figure 9.26(d). The magnitude of the displacements was largest at the center of the displace region and gradually died in intensity, as in the dark-field images. This indicates that the modulated displacement structure is continuous rather than being localized into discrete domains. The regions with the largest displacement magnitude showed alternating layers of $-\pm\pi/2$ phase shifts (as in Figure 9.26(e)) relative to the $[010]_{pc}$ eigenvector displacement, i.e., antiparallel displacements along $[100]_{pc}$. This SVD analysis therefore corroborates the displacement pattern found from K-means analysis (shown in Figure 9.25), but further indicates that the modulated structure seen in Figure 9.23(c) results from a continuous (or diffuse) modulation in displacement magnitude. Similar correlations between the displacements in the A-sublattice were seen between Figure 9.27(d) and Figure 9.24(c). Component 2 of the A-sublattice had smaller displacements relative to component 2 of the Ti-sublattice and the antiparallel displacements were approximately along $[1\bar{1}0]_{pc}$, similar to the results in Figure 9.24(c) and Figure 9.25(c,d). SVD showed that three characteristic displacement patterns existed in the one unit-cell repeat STO-CTO superlattice: 1) isotropic displacement of both Ti- and A-sublattices along the pc axes with varying magnitude, 2) modulated regions of antiparallel displacements of the Ti-sublattice parallel to $[100]_{pc}$, and 3) modulated regions of antiparallel displacements of the A-sublattice along $[1\bar{1}0]_{pc}$ in the same regions as 2. In addition, SVD emphasizes that the improper ferroelectric character of the CTO-STO superlattice was modulated with diffuse boundaries, i.e., the displacement magnitude was continuous and not isolated into discrete domains. This is different than the discrete domains and domain boundaries observed in bilayer perovskites by Huang et al.(Huang et al., 2016).

This Section demonstrates the existence of a modulated antiparallel-displacement structure within a symmetric one unit-cell STO-CTO superlattice. The wavelength of the modulation was about 15.6 nm as observed in dark-field images and determined from spot splitting in selected-area electron diffraction patterns. The modulations occurred parallel to the $[100]_{pc}$ direction, i.e., parallel to the growth direction, and are due to systematic antiparallel displacements of the Ti-sublattice along $[100]_{pc}$ and the A-sublattice along $[1\bar{1}0]_{pc}$, without any apparent variation in the chemical composition of the STO-CTO superlattice. K-means clustering and singular value decomposition analyses were used to further verify the modulations and demonstrate that the boundaries between displaced and undisplaced regions are diffuse. These results suggest that modulations may be employed to manipulate the properties of such one unit-cell superlattice structures.

10 Crystal Structure Reflected in Bonding

In Section 9 the convergence from distinct STO and CTO out-of-plane lattice parameters in SL27 to a singular value in SL4, 2, and 1. In addition octahedral tilting was present in the STO layers with SL periods less than 4 unit-cells, as shown in Section 9.2. Together this suggested a convergence in structure. In this Section core-loss EELS is presented showing that the convergence is also reflected in the electronic structure of the SL.

Core-loss EELS spectra were acquired at 100 keV using a Nion Hermes monochromated aberration-corrected dedicated STEM. To analyze the O-K and Ti-$L_{2,3}$ edges a power law background was fit 5-10 eV before each edge. The resulting O-K and Ti-$L_{2,3}$ edges are shown in Figure 10.1 and Figure 10.2, respectively.

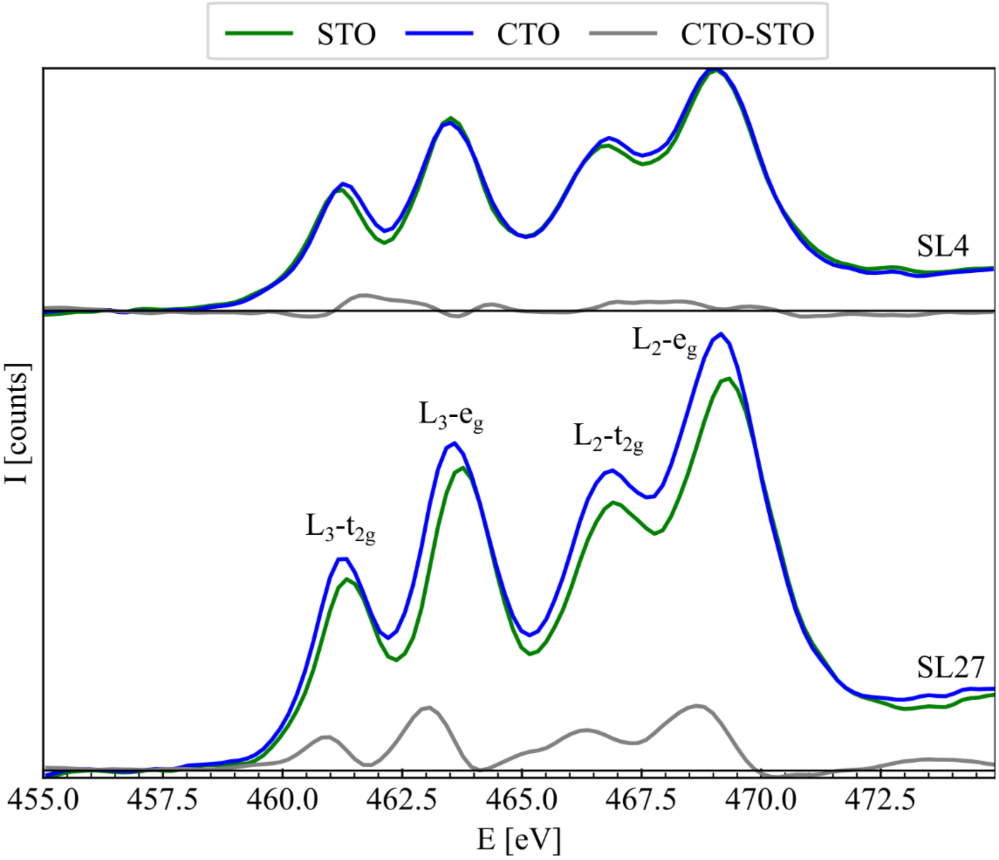

Figure 10.1. Ti-L_{23} edge from SL27 and 4. SL27 had distinct core edges in the CTO (blue) and STO (green), whereas SL4 had nearly identical edges. The difference spectra (CTO minus STO) aid in identification of these similarities and dissimilarities.

Figure 10.1 shows the Ti-L_{23} core-loss edge acquired from STO and CTO layers in SL4 and 27. The two lower energy peaks are the L_2 edge resulting from $2p_{1/2} \rightarrow 3d$ and the two higher energy peaks are the L_3 edges from $2p_{3/2} \rightarrow 3d$ transitions. The splitting of the L_2 and L_3 edges into two white lines is a result of crystal field splitting. To begin the edges in SL27 and SL4 are qualitatively compared. In SL27 the Ti-L_{23} edge showed distinct core losses with similar shape in the STO and CTO layers. The similarity of the peak shapes can be seen in the difference spectra, which appear like a Ti-L_{23} edge. The difference between the Ti-L_{23} edges is seen in the difference spectra as a shift in energy and excess intensity. The comparison spectra indicated that the Ti bonding has slightly different bonding environments in the layers. The STO and CTO phases were $Pm\overline{3}m$ and Pbnm symmetry, respectively, and have different bonding. Therefore, it is expected that the atom projected joint density of state for STO and CTO would be different, as reflected in the spectra(Sakhya et al., 2015). In SL4 the Ti-L_{23} edge from the STO and CTO layers have nearly identical shape and intensity indicating that bonding is similar in the two layers. Note that the difference spectra for SL4 does not resemble a Ti-L_{23} edge but rather has an increased intensity between the t_{2g} and e_g white lines. This is because the splitting of the CTO peaks is smaller than the STO peaks which may indicate smaller crystal field splitting.

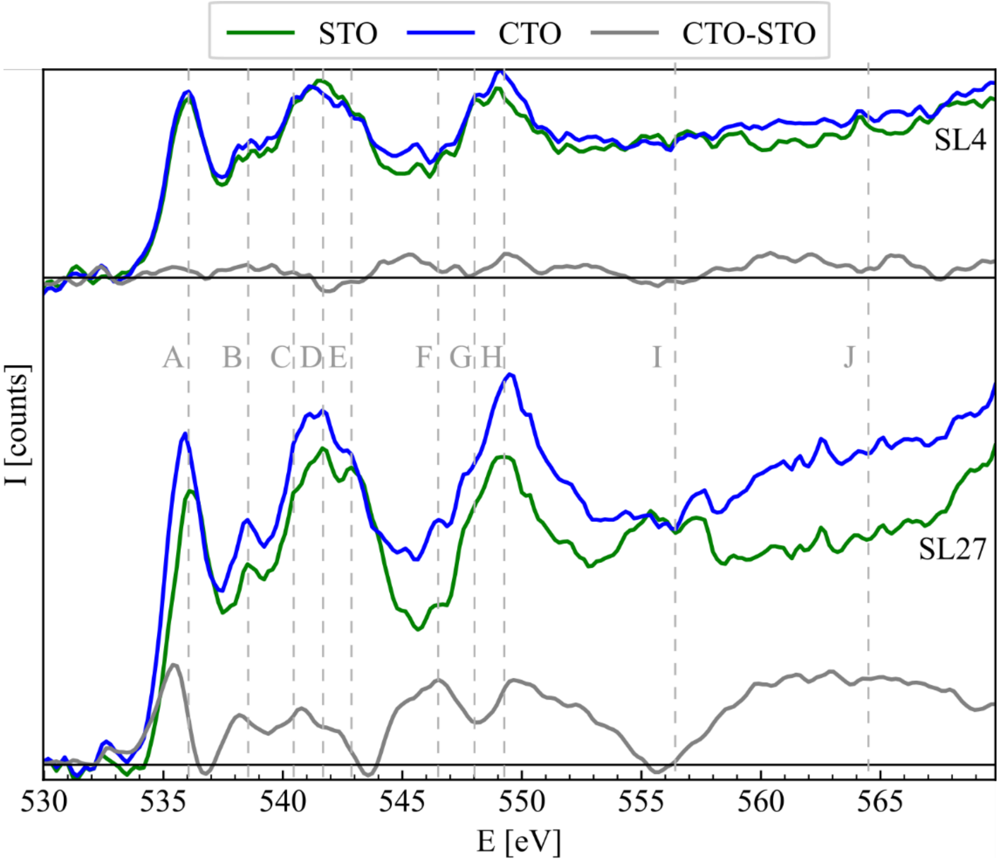

Figure 10.2. O-K edge from SL27 and 4. SL27 had distinct core edges in the CTO (blue) and STO (green), whereas SL4 had nearly identical edges. The difference spectra (CTO minus STO) aid in identification of these similarities and dissimilarities. The spectra are cascaded according to SL period with black horizontal lines indicating zero.

Figure 10.2 shows the O-K core-loss edge acquired from STO and CTO layers in SL4 and 27 that result from O2*s*→O2*p* transitions. All peaks are related to bonding of cations with O2*p* orbitals. Specifically peaks in Figure 10.2 correspond to O2*p* bonding with; A) Ti3*d*-t_{2g}, B) Ti4*d*-e_g, C-E) A*s* or A*d*-e, F-H) A*p* or or A*d*-t_2, and I-J) Ti4*sp* bonds. In SL27 two distinct STO and CTO spectra are observed. The most prominent difference is the O2*p*-Ti4*sp* bonding in STO (peak I) vs in CTO (peak J). The two phases also exhibit slightly different onset energies suggesting different binding energies. Peak E in STO is more prominent than in CTO and peak C is higher relative to D in CTO than in STO. This suggests the different O2*p*-A*s* bonding in the two layers. The Ca-O bond is slightly stronger than the Sr-O bonds because it is slightly more covalent and can result in the small difference in onset energy. This behavior supports the previous connection between stronger covalency and octahedral tilting. The shape of peaks F-H are the same in STO and CTO, but their intensities are different. In SL4 peak B is broader than in SL27. The physical origin for this change is unknown but may be a result of different Ti3*d*-e_g bonding. In SL4 peak A-H was identical in STO and CTO indicating that O-Ti and O-A bonding was identical in the two layers. Thus, the binding/onset energy imply that the covalency of the Sr-O and Ca-O bonds is now similar, and from an electronic perspective explanes the convergence in the oxygen displacement pattern. Peaks I and H are damped or broadened in STO and CTO, respectively. This is a degradation in characteristic STO and CTO O2*p*-Ti4*sp* bonding. The O-K edge spectra show the same overall trend as the Ti-L_{23} edge, a convergence in bonding from distinct O bonding in SL27 to similar bonding in SL4.

In this section it was shown using the Ti-$L_{2,3}$ and O-K edges in EELS that the A-, Ti-, and O-site bonding converged from distinct bonding in SL27 to similar bonding in SL4. This logically can be attributed to a characteristic bonding at the interface which is more prominent at smaller layer thicknesses. The convergence in O-K edge onset energy suggests that the covalency of the Sr-O and Ca-O bonds approached a singular value, in agreement with the changes in crystal structure observed in Section 9.

11 ABO_3 Dipole Simulations

The theoretical treatment of dipole scattering from interfaces was introduced in Section 6.1. In this Section the theory is implemented to simulate STO, CTO, and NGO Ph and SPhs, in addition to STO/CTO interfaces.

Dipole simulations for STO, CTO, and NGO were performed using a factorized dielectric function, Equation 2.16, with literature values shown in Table 11.1-
Table 11.3 as inputs. First considering STO, three Reststrahlen bands exist where bulk modes will not resonate. In addition to these non-resonant frequencies, the region bound by the first and second Reststrahlen bands has $\varepsilon' < 0$ and will also not have a bulk phonon resonance. Three regions remain that contain STO Ph resonance: 1) $\omega < 11.28$, 2) $58.77 < \omega < 67.32$, and 3) $\omega > 97.70$ meV. Similarly, CTO only contains three Ph resonance regions: 1) $\omega < 13.12$, 2) $62.45 < \omega < 68.02$, and 3) $\omega > 98.58$ meV. NGO is a more IR-active material with $\varepsilon' > 0$ for ; 1) $\omega < 21.54$, 2) $23.59 < \omega < 34.12$, 3) $41.03 < \omega < 42.55$, 4) $62.79 < \omega < 64.52$, 5) $69.49 < \omega < 73.35$, and 6) $\omega > 80.09$ meV. The regions just mentioned are the ω_{LO} and ω_{TO} bounds when damping is zero, therefore the true energy windows are offset slightly according to Equation 2.17.

Table 11.1. The energy and damping for phonon modes in STO found using FT-IR by ref. (Kamarás et al., 1995). Units are in meV.

#	E_{TO}	γ_{TO}	E_{LO}	γ_{LO}
0	11.28	1.86	21.33	0.47
1	21.70	0.67	58.77	0.56
2	67.32	2.11	97.70	3.10

Table 11.2. The energy and damping for phonon modes in CTO found using FT-IR by ref. (Železný et al., 2002). Units are in meV.

#	E_{TO}	γ_{TO}	E_{LO}	γ_{LO}	#	E_{TO}	γ_{TO}	E_{LO}	γ_{LO}
0	13.12	4.00	17.26	4.55	**7**	37.44	1.05	39.17	1.70
1	17.46	2.37	19.40	0.99	**8**	39.49	1.54	45.68	1.35
2	19.71	1.02	20.53	1.33	**9**	45.73	1.36	52.92	3.99
3	21.00	1.20	22.74	2.19	**10**	54.52	3.10	59.96	2.63
4	23.43	2.07	27.75	1.44	**11**	61.41	2.85	62.45	2.11
5	27.95	1.30	32.42	1.87	**12**	68.02	3.21	79.90	6.77
6	32.62	1.74	37.31	1.02	**13**	79.96	6.98	98.58	3.36

Table 11.3. The energy and damping for phonon modes in NGO found using FT-IR by ref. (Nuzhnyy et al., 2011). Units are in meV.

#	E_{TO}	γ_{TO}	E_{LO}	γ_{LO}	#	E_{TO}	γ_{TO}	E_{LO}	γ_{LO}
0	14.56	0.69	14.72	0.56	**8**	37.44	1.13	38.40	1.53
1	16.25	6.60	16.64	7.24	**9**	38.68	1.79	41.03	1.59
2	21.54	0.74	22.86	1.79	**10**	42.55	1.60	43.85	1.13
3	22.96	1.64	23.59	0.50	**11**	44.21	1.17	52.00	1.51
4	30.00	0.87	30.36	0.82	**12**	52.63	1.56	62.79	1.29
5	31.63	0.83	31.96	0.83	**13**	64.52	1.09	69.49	2.36
6	34.12	1.15	35.32	1.05	**14**	73.35	3.01	80.09	2.80
7	35.70	1.13	36.76	1.14					

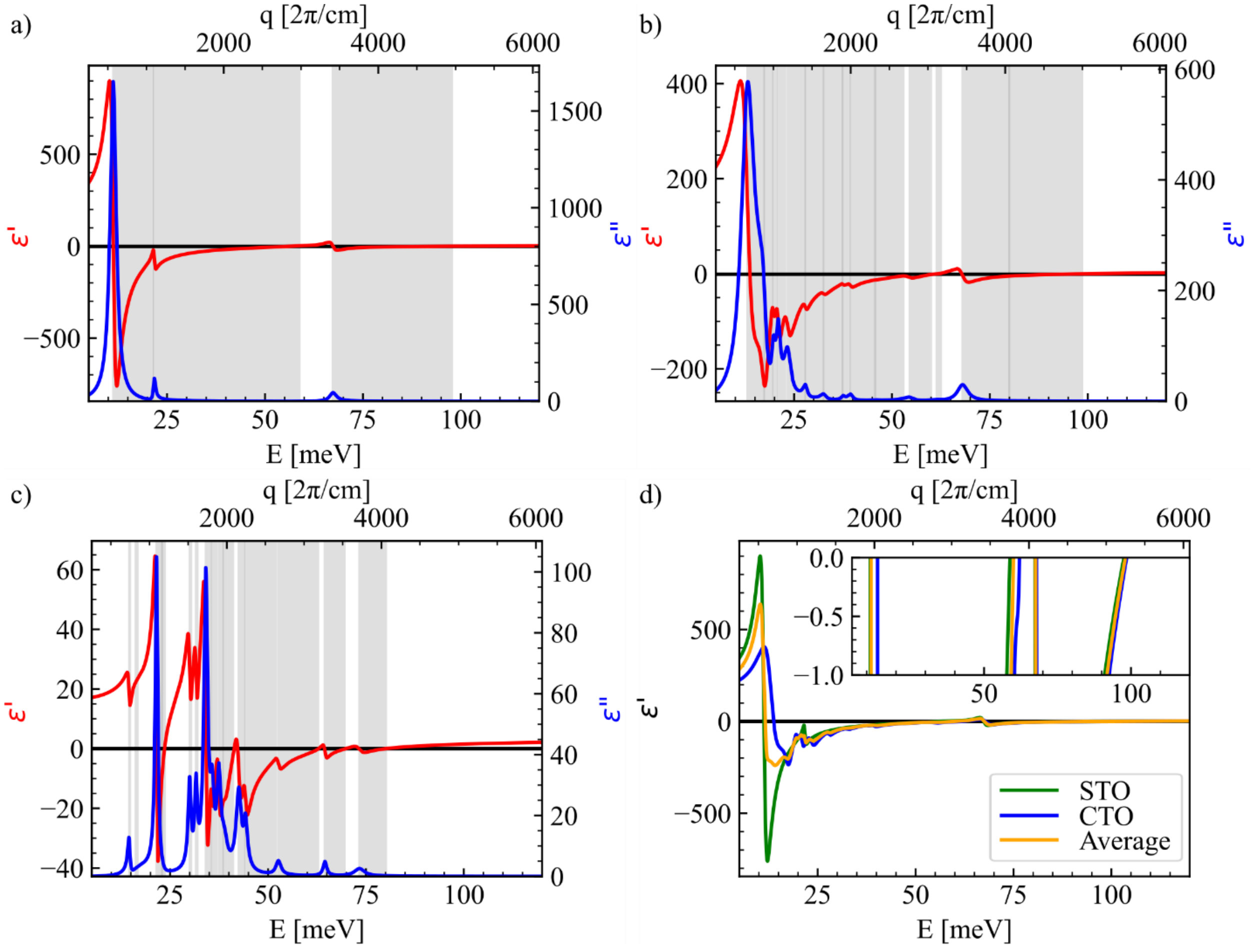

Figure 11.1. Factorize dielectric functions for (a) STO, (b) CTO, and (c) NGO. The real and imaginary components of ε are displayed on opposite y-axes and are color coordinated with the plots. Regions shaded gray are Reststrahlen bands bound by ω_{TO} and ω_{LO}. The real component of ε for STO, CTO, and the average of STO and CTO is shown in (d) along with an inset magnifying the region of ε' spanning -1 to 0, i.e. the intercepts corresponding to SPh and Ph, respectively.

The IPh, SPh, and Ph dispersions for a system of STO and CTO is shown in Figure 11.2.

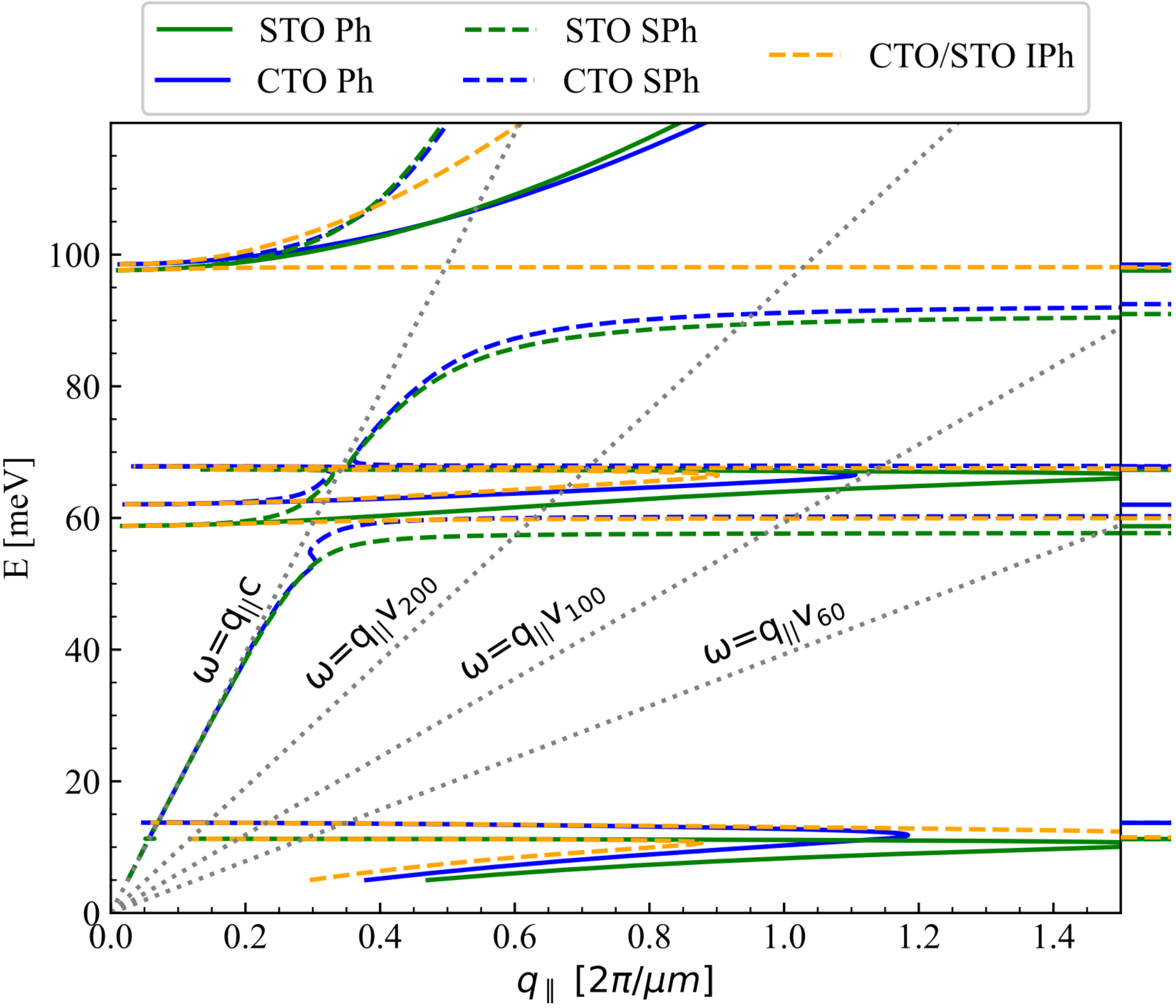

Figure 11.2. Dispersions for IPhP and SPhP (--) and PhP (-) in a system comprised of CTO and STO. The STO (green) and CTO (blue) modes have been grouped by color to aid in comparison. The frequency of light and the velocity of 60, 100, and 200 keV electrons are indicated by gray dotted lines. The dashed lines along the right axis are the non-polaritonic modes calculated in the NR approximation.

Table 11.4. Non-radiative phonon modes associated with STO-CTO slabs in meV. Values were numerically calculated by setting ε_1=0 or ε_1+ ε_2=0 for the Ph and IPh, respectively.

CTO		**STO**		**STO/CTO**
Ph	**SPh**	**Ph**	**SPh**	**IPh**
13.7	13.73	11.27	11.27	11.52
62.1	60.29	58.78	57.73	59.99
67.8	67.89	67.36	67.38	67.49
98.5	92.51	97.61	91.01	98.09

It is clear from the SPh dispersions that the surface response of STO and CTO will be nearly identical when interacting with any of the three electrons. For a 60 keV electron only the Ph modes below 15 meV are to the right of the "electron line" and contribute to radiative loss of the electron through Cherenkov radiation. At higher keV, such as 100 or 200, the probability of Cherenkov radiation increases but will be minimal. The IPh that are non-dispersive have $\varepsilon_1\varepsilon_2 < 0$ and $\varepsilon_1 + \varepsilon_2 < 0$ so have real $q_\perp$ and are non-radiative. The IPh that follow the bulk dispersions have $\varepsilon_1\varepsilon_2 > 0$ and $\varepsilon_1 + \varepsilon_2 > 0$ so have real $q_\parallel$ but imaginary $q_\perp$ and are radiative.

For all three keV shown, nearly all IPh and SPh modes are excited near their asymptotic limit and are non-polaritonic. The non-polaritonic Ph, SPh, and IPh mode energies are listed in Table 11.4. One exception is the STO and CTO SPhP ~90 meV for a 200 keV electron. These modes are slightly, but not far, from the non-polaritonic frequency so will be considered as non-polaritonic anyway. Ph and IPh between 60 and 65 meV display significant dispersion and will be considered polaritonic for a 200 keV electron. The IPh modes with 11.52 and 67.49 meV displayed negative slopes (negative v_g). These IPh are the non-radiative IPh associated with mismatch of TO phonons across the STO/CTO interface. The negative slope is like the Ph response near ω_{TO} that results from the damping present in the material. This means that energy is being dissipated at the interface as a result of decay processes like frictional forces. The IPh modes with 59.99 and 68.09 meV, associated with the mismatch of LO phonons, had a dispersion with positive slope (positive v_g). Another notable feature is that the existence of IPh and Ph from 65-70 meV that can only be excited by the 200 keV incident electrons.

This analysis of dispersions provides insight to what phonon excitations are expected, and if they are polaritonic, in addition to how radiative different keV electrons will be.

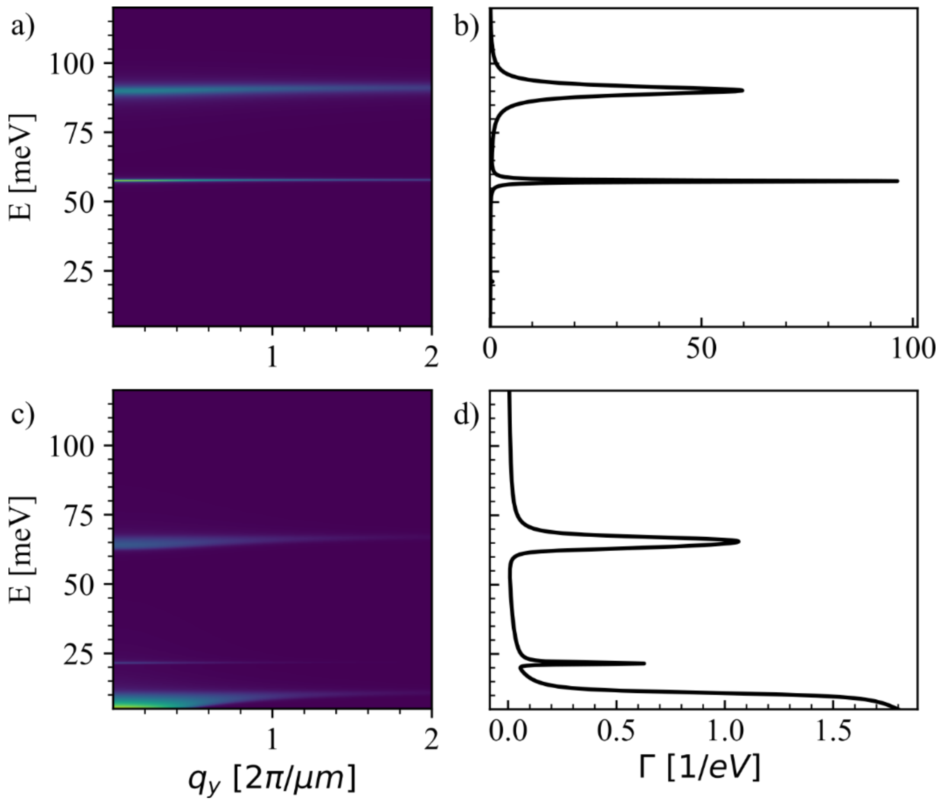

Figure 11.3. (a and c) DDCS and (b and d) DCS for an aloof electron probe 1 nm away from an STO surface. (a and b) TM and (c and d) TE components are shown separately.

Figure 11.3 shows the DDCS (a and c) and DCS (b and d) for an aloof electron probe 1 nm away from an STO surface (ie vacuum/STO interface). The TM (a and b) is one to two order of magnitude larger than the TE (c and d) and will contribute relatively little to the total energy loss of the electron, as stated in Section 6.1. Cherenkov radiation contributions are seen below 15 meV in the TE component. Loss branches at 65 meV in the TE component and 80 meV in the TM component are dispersive (although minimally) as expected from the dispersions shown in Figure 11.2.

The complementary geometry for an aloof and transmitted electron probe with *b* such that $e^{-2q_\perp b} = 1/2$ is shown in Figure 11.4. The SPh are at the same energy as the aloof geometry, but now that the electron probe is in the sample Ph (and *begrenzungs*) losses occur. Both STO and CTO show relatively low probability of loss below 50 meV and very similar loss from 90-95 meV. These higher energy modes are a result of the Ti-O stretch vibrations in the bulk and at the surface. The modes around 90-95 meV are LO modes and the ones around 60 meV are TO modes.

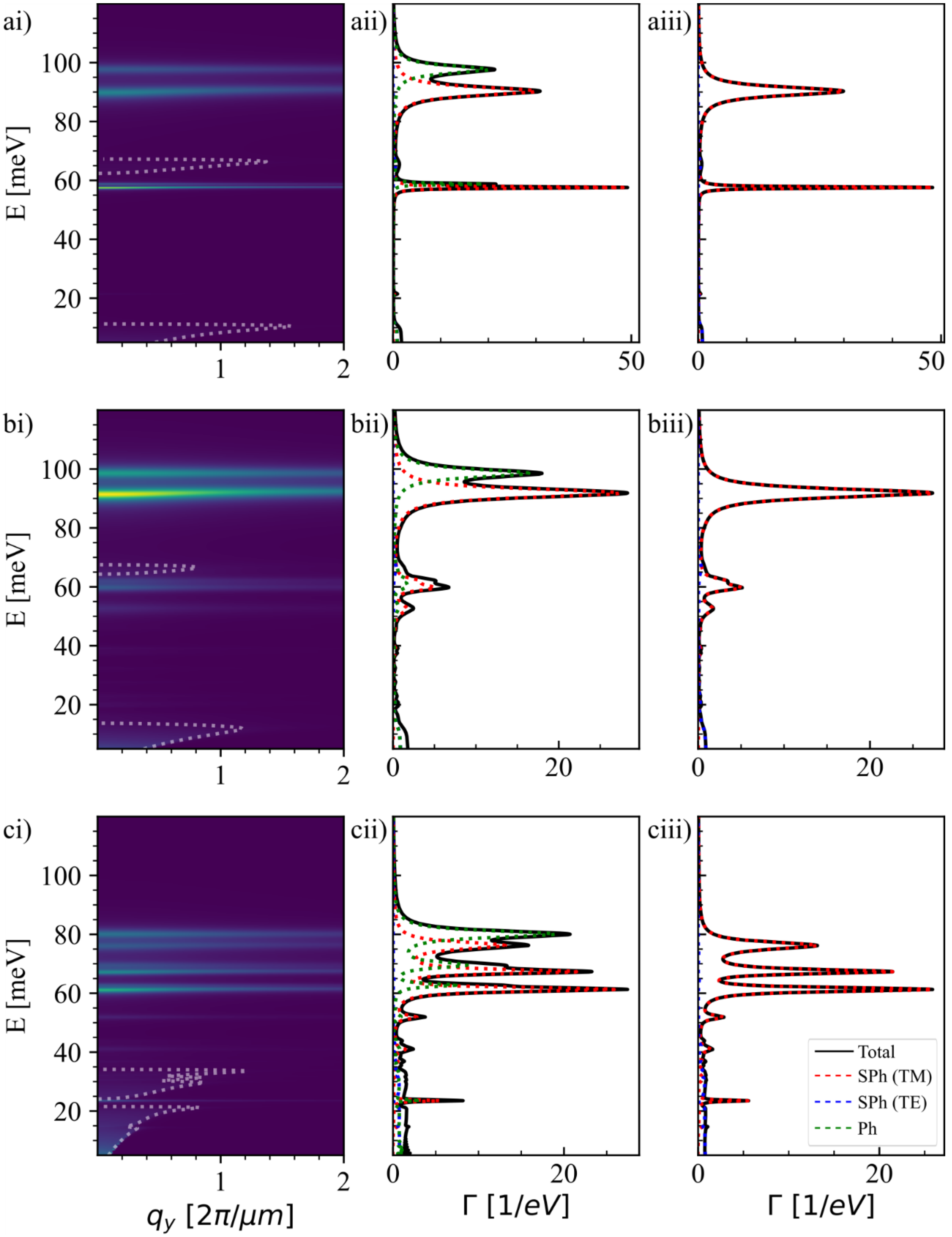

Figure 11.4. (i) DDCS and (ii) DCS in (a) STO, (b) CTO, and (c) NGO. The electron probe was positioned so $e^{-2q_\perp b} = 1/2$ The surface component of (ii) is shown in (iii) and corresponds to the aloof signal at an equal b form the surface. Dotted lines in (i) represent the dispersion of light in the material. Energy loss within the dotted lines is from Cherenkov radiation.

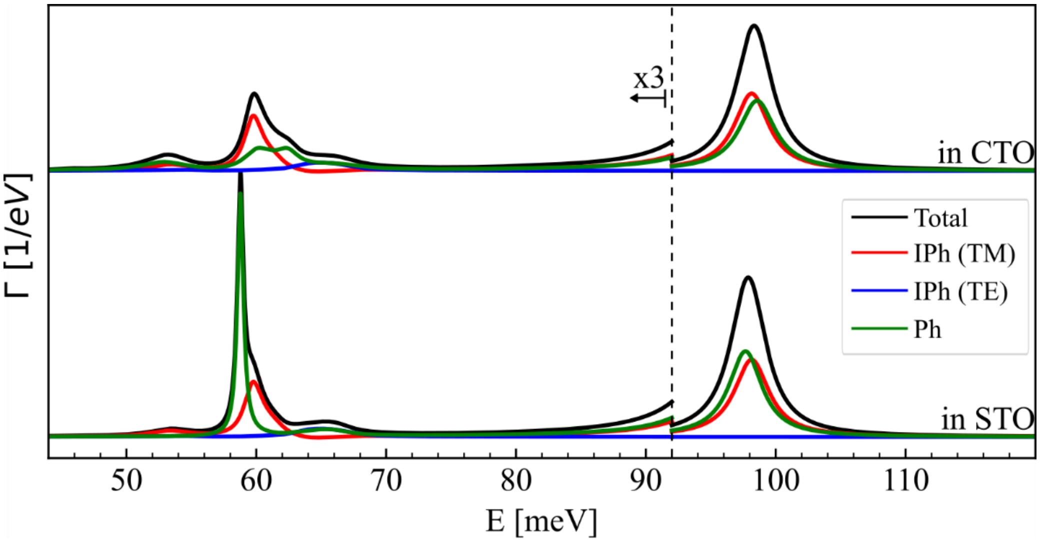

Figure 11.5. DCS for an electron probe 509 nm away from a STO/CTO interface.

Considering the similar energy of STO and CTO phonons above 45 meV it is expected that losses from an IPh, which is proportional to the inverse mean of permittivities, would be difficult to distinguish from Ph losses. To illustrate this conjecture the DCS for an STO/CTO interface with the probe positioned in STO and CTO was simulated, as shown in Figure 11.5. The probe was positioned 509 nm away from the interface so that the exponential term in Equations 6.18c and d is one half, and therefore the proximity effect of the bulk and interface probabilities are equal. Figure 11.5 shows that the IPh and Ph at 98 meV are indistinguishable when the probe is in either material. When the probe is in CTO the bulk losses at ~60 meV appear as a shoulder due to their low intensity, however in STO the bulk losses produce a sharp peak that is distinguishable from the IPhP. Neither of these plots include blurring from the finite energy resolution of the microscope, which will broaden each peak. The presented simulation was run at 509 nm so that the energy of the responses and their intensity when contributing equally could be evaluated. However, the thin films of interest are 200 nm total thickness and the largest period SL (n=27 unit-cells) has layers ~10.5 nm thick, therefore the electron probe could at most be positioned ~5 nm away from the STO/CTO interface. Given that the real probe position is 10 times smaller than the simulation shown in Figure 11.5, i.e. a factor of $e^{\pm 450} \approx 10^{\pm 196}$ in Equation 6.18, then the bulk component becomes nearly non-existent and only the interface term is present. One way to picture this scenario is that the proximity of the probe to the interface emphasizes interfacial inelastic scattering which being an average of permittivities is like an effective medium.

If the full superlattice is considered then multiple IPh^+ and IPh^- exist, as discussed in Section 6.1. In the case of a 200 nm thin film of SL27 there are approximately 258 STO/CTO interfaces. With the large number of interfaces, it is expected that distinguishable IPh^+ and IPh^- do not exist for each coupled mode but rather $SLPh^+$ and $SLPh^-$ bands. In addition the IPh modes, as shown in Figure 11.2, are relatively non-dispersive and confined to a small energy window as a result of the similarities in STO and CTO permittivities. The $SLPh^+$ and $SLPh^-$ bands would have remarkably similar energies and be non-dispersive. In a realistic experiment, damping of the phonon modes and non-finite resolution would broaden the already nearly overlapping peaks into what would appear as a singular peak with an energy equal to the IPh. For these reasons, any splitting of observed vibrational peaks are most likely not attributed to $SLPh^+$ and $SLPh^-$.

In this section theoretical predictions were made for the expected Ph, SPh(P), and IPh(P) energy losses that should be present in aloof and transmission geometries. This will aid in analysis of acquired EELS spectra. It was observed that signal form >90 meV was similar for CTO and STO. The main differences in energy loss were from 50-65 meV. For a system comprised of STO and CTO, the Ph and IPh ~98 meV were indistinguishable. In the energy range surrounding 60 meV, distinguishable bulk and IPh were observed in STO, but only the IPh would be observable given realistic impact parameters in the STO-CTO SL. Lastly, given the non-dispersive nature of the IPh, phonon damping, and finite experimental resolution, observation of $SLPh^{\pm}$ are not expected but rather a single SLPh with an energy similar to the IPh.

12 Vibrational EELS of Superlattices

So far, it has been shown that the crystal structure and electronic structure in the layers of a STO-CTO SL transition from being distinguishable, resembling monolithic STO and CTO in SL27, to indistinguishable in SL2-4. A further transition was observed when the number of unit-cells was reduced further from two to one unit-cell per layer. Given that the crystal and electronic structures change with the number of unit-cells in a SL layer, it seems reasonable to postulate that the phonon spectrum could also change. In this Section vibrational spectroscopy using EELS of STO-CTO SLs with a different number of unit-cells per SL layer will be presented. Large changes in the vibrational EELS spectra were observed. Simulations in Sections 11 aid in interpretation of the spectra but large differences between the theoretical and experimental spectra exist.

Aloof vibrational EELS spectra were acquired at 60 keV using a Nion Hermes monochromated aberration-corrected dedicated STEM. Proper removal of the ZLP is prone to error and leads to difficulties in interpreting low-energy losses in EELS spectra. Herein a power-law was used for background removal because it provided the most consistent results. It was found that improper background subtraction predominantly affected the lowest energy peaks. The background of the higher-energy peaks was low enough that improper fitting of the ZLP tail provided minimal variation in peak position after subtraction. Background subtracted vibrational EELS spectra are shown in Figure 12.1(a).

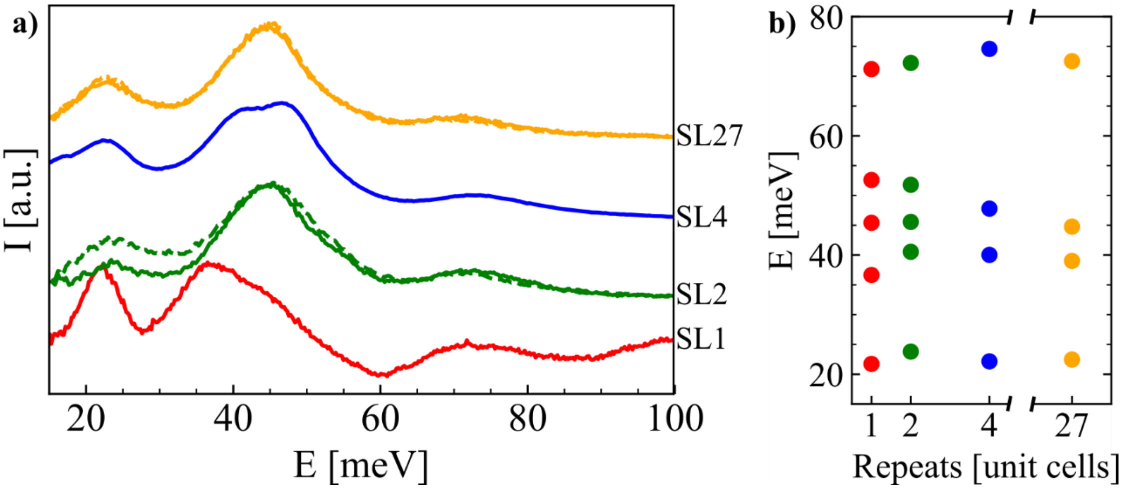

Figure 12.1. (a) Solid lines show low-loss EELS acquired perpendicular to SL27, 4, 2 and 1. Dashed lines show low-loss EELS acquired parallel to SL27 and 2. (b) Voigt peak centers from fitted perpendicular spectra show the effect of SL layer thickness on SPh energies.

The solid lines in Figure 12.1(a) show low-loss EELS acquired perpendicular to all four SLs (i.e. "above" the thin film). The EEL spectra differ markedly as a function of superlattice repeat unit. While common peaks are apparent near 22 and 71 meV for each of the superlattices, their relative strength and the emergence of modes in the 30-60 meV range indicate changes dependent upon the layered structure itself. Quantitatively, for example, Voigt fits indicate a shifting to lower energy for a mode near 71 meV with smaller SL period (See Figure 1b). Modes at 45 and 55 meV shifted to higher energy when the SL, then with further reduction in SL period the modes shifted to lower energy and split. Additionally, the mode-shape in the range of 39-55 meV evolves substantially as a function of superlattice period.

The dashed lines in Figure 12.1(a) show low-loss EELS acquired parallel to SL2 and 27 (i.e. "next to" the thin film). The peak energies and relative shape of the spectra are nearly identical to spectra acquired in a perpendicular geometry. The only divergence from the perpendicular spectra is the intensity of the 22 meV peak in SL2, which can be attributed to background subtraction errors. One may expect that the spectra would reflect the anisotropy of the SL, however it appears that this is not true. One explanation may derive from the large decay lengths of the dipole excitations being measured. The large decay lengths can be avoided by collecting impact scattered electrons via momentum-resolved EELS as discussed in Section 2.2, this however currently presents challenges for most samples larger than a few unit-cells thick and was not done here. With decay lengths on the order of 500 nm the electron probe is insensitive to individual layers. The delocalized signal therefore may lead to an "effective medium" sampling of each SL. This suggests the changes in vibrational spectra are a result of changes in the crystal structure or interface density of the material not a result of geometrical conditions in the experiment. The core-loss EELS results showed a convergence to similar bonding within the layers as the number of unit-cells was decreased. Similarly, the diffraction and imaging results showed that the crystal structure of the layers was approaching a “happy medium” characteristic of interface structural units. This would seem to imply that the SL would consist of less vibrational modes as the number unit-cells in a layer decreased since less unique phases are present, but the structural units in fact would have more vibrational modes than the bulk because of the larger basis. In the case of SL4 there are still some planes that are reminiscent of the bulk layers such that there are a larger number of modes from the number of phases and the interface. In addition, as the number of interfaces approaches the number of unit-cells in the SL the electron probe becomes more sensitive to these vibrations. Therefore, it is likely that the cause of the new vibrational modes originates from the interface structure. This not only agrees with the number of new recognizable peaks but also logically tracks with the increasing intensity of the new peaks as the number of unit-cells per layer is reduced.

Major differences are observed between the vibrational spectra of Figure 12.1 and the dipole scattering simulations shown in Figure 11.4(a-c iii) and Figure 11.5. There are effectively three sets of peaks below 80 meV spaced approximately 30 meV apart in the experimental vibrational spectra, as shown in Figure 12.1, compared to the three peaks spaced ~5meV apart observed in simulated aloof vacuum/sample spectra and STO/CTO interface spectra, as shown in Figure 11.4(a-c iii) and Figure 11.5 respectively. From another perspective, the experimental spectra had signal in the energy range from 20-55 and 65-85 meV where dipole EELS simulations predicted little-to-no inelastic dipole scattering from phonons. One explanation could derive from anisotropy in the phonon response of the crystalline lattice (not the SL). The selective polarization and sensitivity to anisotropy of vibrational EELS was recently explored in boron subphosphide (Radtke et al., 2019). For a specific perovskite example, different phonon modes are active for different orientations of NGO or have slightly shifted energies (Nuzhnyy et al., 2011). Similar variation in phonon energy was observed for STO on the NGO substrates using Fourier transform infrared spectroscopy, but to lesser extent. Given that STO and CTO exhibited non-cubic symmetry it is plausible that different phonon energies may occur with different orientations. To verify anisotropy as the origin of the variation in experimental signal, controlled tilting experiments or known sample orientation are suggested, i.e. acquiring signals for consecutive orientations to know the variation or setting a particular zone axis to eliminate orientation as the source.

Another plausible source for the origin of the experimentally observed peaks not appearing in the dipole scattering simulations is that the dipole simulations at interfaces consider only the interference effects from oscillating dipoles in the bounding layers. From an atomistic perspective, we know that the TiO_2 layer at the interface would in reality feel a different potential landscape than within the layers, because it is anisotropically surrounded by different AO planes. This would result in new phonon modes that dipole simulations cannot account for. As a result of the different bonding potentials and bounding crystal structure ,the oxygen octahedra are also expected to distort at the interfaces between layers. The existence of new symmetry from the distortions is also cause for new phonon modes to exist and the microscopic dipole simulations can not account for these atomistic effects. Comparing experiment and theory one conclusion can be drawn based on the energy range that different atoms participate. The dipole active modes for CTO and STO, identified by Železný et al. and Perry et al. (Perry et al., 1967; Železný et al., 2002), in the energy range 30-60 meV are associated with Ti and O only. A-site modes only exist below 30 meV. Therefore, the changes observed in the spectra are associated with the Ti- and O-sublattices.

To summarize the vibrational EELS results, 22 and 71 meV phonon peaks were present in the vibrational spectra of all four superlattices. An additional cluster of peaks was observed from 30-60 meV that evolved from two peaks in SL27 and SL4 to three peaks in SL2 and SL1. The origin of these additional peaks at 30-60 meV is most likely due to new Ti and O vibrational modes from Ti and O at the interface between STO and CTO layers. The atoms have environments that are different from atoms in the layers. The number of interfaces approaches the number of unit-cells in the SL as the number of unit-cells in a layer decreases and therefore the significance of these vibrations is most apparent for the two smallest periodicities . Spectra acquired parallel and perpendicular to the SL were nearly identical indicating an effective means sampling of the SL void of sensitivity to structural anisotropy. There is disagreement between the theoretically predicted spectra and experimentally acquired spectra. The origin of the disagreement is not known and could be a topic future research. Although there is disagreement, the theory in general attributes the energy of evolving peaks to vibrations within the Ti- and O-sublattices.

13 Conclusions

In this thesis, it was found that crystal and electron structures in the layers of a symmetric $SrTiO_3$-$CaTiO_3$ superlattice converged from their distinct monolithic constituents to a similar and unique structure, as the number of unit-cells in the layers was reduced from twenty-seven to one. The converged structure in the smaller-period superlattices displayed qualities reminiscent of the interface structure in the larger-period superlattices. It was also found that the vibrational response of the superlattices changed with the number of unit-cells in a layer and was not consistent with theoretical predictions using the dipole scattering approximation and dipole-active phonon values for $SrTiO_3$, $CaTiO_3$, and $NdGaO_3$ from the literature. Therefore, the vibrational response of the superlattices was also unique compared to the monolithic phases. These results demonstrate that superlattices can acquire unique structures and properties as their sizes decrease below certain values and further, that these phenomena need to be quantified at the nanoscale to obtain a complete understanding of their behavior. More specific findings of this thesis are summarized below.

1) Using electron and X-ray diffraction it was found that the out-of-plane lattice parameter converged to a single $SrTiO_3$-$CaTiO_3$ value that was approximately the average of the two unrelaxed lattice parameters of SL27. The in-plane lattice parameter was different (but nearly equivalent) to the substrate in SL4 and 27. In contrast, SL2 and SL1 had in-plane lattice parameters similar to their out-of-plane lattice parameters, which were larger than SL4 and 27, indicating that thes film in-plane lattice parameters were not determined by the substrate.
2) Splitting of $(002)_{pc}$ and $\{202\}_{pc}$ diffraction peaks and non-split ordered reflections in SL27 indicated that the thin film had relaxed to Pbnm-$CaTiO_3$ and strained $Pm\bar{3}m$-

SrTiO$_3$, much like the monolithic constituents. The presence of $\frac{1}{2}(102)_{\mathrm{pc}}$ and $\frac{1}{2}(303)_{\mathrm{pc}}$ ordered reflections and absence of $\frac{1}{2}(201)_{\mathrm{pc}}$ ordered reflections indicated two domains of CaTiO$_3$ were present with c-axes in the plane of the film and an orientation relationship of $[100]_{pc-CTO}//[010]_{pc-CTO}$.

3) The Pbnm-CaTiO$_3$ and Pm$\overline{3}$m-SrTiO$_3$ phases were further confirmed using scanning NBED. SADP from the $[010]_{\mathrm{pc}}$ showed that SL2 and 4 had ordered reflections and therefore ordered octahedral tilts. This was supported by a derivation concluding that in a symmetric superlattice with an even number of unit-cells in each layer ½ type ordered reflections do not appear as a result of the chemical ordering. Thus ½ type ordered reflections must be a result of displacements within the crystal structure. This was also supported by simulations.
4) Using iDPC images of SL27 an in-phase tilt angle was measured in the STO layer as 1.84° and 2.69° in the TiO$_2$ and AO planes, respectively, and is thought to result from either an error in the manual placement of O positions or coupling between the ATO layers of the SL. The out-of-phase tilting in the CTO layer was 10.04° and 10.32° in the TiO$_2$ and AO planes, respectively. There were three planes at the interface between STO and CTO where O column splitting was different than in the layers. This was also observed using ellipticity as a measure of out-of-phase tilting. The interface between the STO and CTO layers of the SL was characterized as chemically abrupt, structurally diffuse, and as a $(1\mathrm{x}1\mathrm{x}2)_{\mathrm{pc}}$ structural unit with out-of-phase tilting and distortions of the TiO$_6$ octahedra.
5) Unlike in SL27, the in-phase tilt axis was in the growth direction and SL normal with only one orientation of the crystal present (i.e. no domains). SADP taken from the two in-plane $\langle 110\rangle_{pc}$ ZAs further refined the possible space group of the lattice to either P2$_1$/m or Cmcm and not Pbnm, however some discrepancies were found with both P2$_1$/m and Cmcm, so the exact space group was not determined. With the $[010]_{\mathrm{pc}}$ and $\langle 110\rangle_{pc}$ ZAs it was concluded that SL4 had both ordered in- and out-of-phase tilt axes.
6) Using iDPC the out-of-phase tilt-like displacement of oxygen in TiO$_6$ octahedra was characterized. It was shown that the structure of SL4 was approaching the interface structure in SL27. SL2 was entirely composed of interface structural units observed in SL27. This showed that as the number of unit-cells in a layer decreased, the system transitioned from being composed of bulk ATO layers separated by interfaces (i.e. as in SL27), to a system predominantly consisting of interfaces (as in SL4) to a system with a single phase characteristic of the prior interface structure (as in SL2). The TiO$_6$ octahedra out-of-phase tilt-like angle converged to a value between the two bulk-like phase tilt angles as the interface structure predominated. The angle was skewed toward the tilt angle of CTO, which was concluded to result from the higher stability of tilting in CTO than STO.
7) SL1 took on an entirely unique structure compared to the other superlattices. SL1 had antiparallel displacements with a modulation in the amplitude of displacement. The wavelength of the modulation was about 15.6 nm as observed in dark-field images and determined from spot splitting in selected-area electron diffraction patterns. The

modulations occurred parallel to the $[100]_{pc}$ direction, i.e., parallel to the growth direction, and are due to systematic antiparallel displacements of the Ti-sublattice along $[100]_{pc}$ and the A-sublattice along $[1\bar{1}0]_{pc}$, without any apparent variation in the chemical composition of the $SrTiO_3$- $CaTiO_3$ superlattice. K-means clustering and singular value decomposition analyses were used to further verify the modulations and demonstrate that the boundaries between displaced and undisplaced regions are diffuse.

8) It was then shown using the Ti-$L_{2,3}$ and O-K edges in EELS that the A-, Ti-, and O-site bonding converged from distinct bonding in SL27 to similar bonding in SL4. The onset energy of the O-K edge suggested that the covalency of the A-O bonds converged, which can be tied to the concurrent changes in crystal structure. Qualitatively the splitting and intensity of white lines in the Ti-$L_{2,3}$ edge converged from different to similar values. The O-K edge also showed different peak energies and intensities in spectra from SL27 converging to similar values in spectra of SL4.
9) To summarize the vibrational EELS results, 22 and 71 meV phonon peaks were present in the vibrational spectra of all four superlattices. An additional cluster of peaks was observed from 30-60 meV that evolved from two peaks in SL27 and SL4 to three peaks in SL2 and SL1. Spectra acquired parallel and perpendicular to the SL were nearly identical, indicating an effective mean sampling of the SL void of sensitivity to structural anisotropy. There was disagreement between the theoretically predicted spectra and experimentally acquired vibrational spectra. The origin of this disagreement is not known and provides opportunity for future research. Simulations of the vibrational spectra indicate that the measured vibrations in the bulk-like phases should be non-polaritonic and non-radiative. Although there is disagreement, the theory in general attributes the energy of evolving peaks to vibrations within the Ti- and O-sublattices and new Ti and O vibrational modes from these aotms at the interface between layers. In other words, the new modes are from the interface structure. As the number of interfaces approaches the number of unit-cells in the SL, the significance of these vibrations increase and are most apparent for the two smallest SL periodicities.

14 References

Aikawa, Y., & Fujii, K. (2011). Self-Consistent anharmonic theory and its application to the soft mode of $BaTiO_3$. *Ferroelectrics* **414**, 77–85.

Albuquerque, E. L., & Cottam, M. G. (1993). Superlattice plasmon-polaritons. *Physics Reports* **233**, 67–135.

Ali, R., & Yashima, M. (2005). Space group and crystal structure of the Perovskite $CaTiO_3$ from 296 to 1720K. *Journal of Solid State Chemistry* **178**, 2867–2872.

Anderson, M. T., Poeppelmeier, K. R., Zhang, J. P., Fan, H. J., & Marks, L. D. (1992). Barium lanthanum copper tin oxide ($Ba_2La_2Cu_2Sn_2O_{11}$): a new layered perovskite with a modulated structure. *Chemistry of Materials* **4**, 1305–1313.

Anwar, S., & Lalla, N. P. (2008). Electron microscopic studies of the antiferroelectric phase in $Sr_{0.60}Ca_{0.40}TiO_3$ ceramic. *Journal of Solid State Chemistry* **181**, 997–1004.

Aschauer, U., & Spaldin, N. A. (2014). Competition and cooperation between antiferrodistortive and ferroelectric instabilities in the model perovskite $SrTiO_3$. *Journal of Physics: Condensed Matter* **26**, 122203–122208.

Aso, R., Kan, D., Shimakawa, Y., & Kurata, H. (2013). Atomic level observation of octahedral distortions at the perovskite oxide heterointerface. *Scientific Reports* **3**, 2214–2216.

Ball, C. J., Begg, B. D., Cookson, D. J., Thorogood, G. J., & Vance, E. R. (1998). Structures in the system $CaTiO_3/SrTiO_3$. *Journal of Solid State Chemistry* **139**, 238–247.

Bednorz, J. G., & Müller, K. A. (1984). $Sr_{1-x}Ca_xTiO_3$: An XY quantum ferroelectric with transition to randomness. *Physical Review Letters* **52**, 2289–2292.

Bhalla, A. S., Guo, R., & Roy, R. (2000). The perovskite structure—a review of its role in ceramic science and technology. *Materials Research Innovations* **4**, 3–26.

Biegalski, M. D., Qiao, L., Gu, Y., Mehta, A., He, Q., Takamura, Y., … Chen, L.-Q. (2015). Impact of symmetry on the ferroelectric properties of $CaTiO_3$ thin films. *Applied Physics Letters* **106**, 162904–162915.

Bolton, J. P. R., & Chen, M. (1995). Electron energy loss in multilayered slabs. *Ultramicroscopy* **60**, 247–263.

Borisevich, A. Y., Eliseev, E. A., Morozovska, A. N., Cheng, C.-J., Lin, J.-Y., Chu, Y. H., … Kalinin, S. V. (2012). Atomic-scale evolution of modulated phases at the ferroelectric–antiferroelectric morphotropic phase boundary controlled by flexoelectric interaction. *Nature Communications* **3**, 775–778.

Bousquet, E., Dawber, M., Stucki, N., Lichtensteiger, C., Hermet, P., Gariglio, S., … Ghosez, P. (2008). Improper ferroelectricity in perovskite oxide artificial superlattices. *Nature* **452**, 732–736.

Buttner, R. H., & Maslen, E. N. (1992). Electron difference density and structural parameters in $CaTiO_3$. *Acta Crystallographica Section B Structural Science* **48**, 644–649.

Cahn, J. W. (1961). On spinodal decomposition. *Acta Metallurgica* **9**, 795–801.

Cahn, J. W., & Hilliard, J. E. (1958). Free Energy of a Nonuniform System. I. Interfacial Free Energy. *The Journal of Chemical Physics* **28**, 258–267.

Caldwell, J. D., Kretinin, A. V., Chen, Y., Giannini, V., Fogler, M. M., Francescato, Y., … Novoselov, K. S. (2014). Sub-diffractional volume-confined polaritons in the natural hyperbolic material hexagonal boron nitride. *Nature Communications* **5**, 5221–5229.

Campbell, B. J., Stokes, H. T., Tanner, D. E., & Hatch, D. M. (2006). *ISODISPLACE* : a web-based tool for exploring structural distortions. *Journal of Applied Crystallography* **39**, 607–614.

Cao, Y., Park, S. Y., Liu, X., Choudhury, D., Middey, S., Meyers, D., … Chakhalian, J. (2016). Orbital configuration in $CaTiO_3$ films on $NdGaO_3$. *Applied Physics Letters* **109**, 152905–152906.

Carl W., N. (1963). *Ferroelectricity and the chemical bond in perovskite-type oxides* (pp. 1–35). Cambridge, Massachusetts: Laboratory for Insulation Research Massachusetts Institute of Technology.

Chatterjee, S., Bultinck, N., & Zaletel, M. P. (2020). Symmetry breaking and skyrmionic transport in twisted bilayer graphene. *Physical Review B* **101**, 165141–25.

Chen, D.-Z. A., Narayanaswamy, A., & Chen, G. (2005). Surface phonon-polariton mediated thermal conductivity enhancement of amorphous thin films. *Physical Review B* **72**, 155435.

Close, R., Chen, Z., Shibata, N., & Findlay, S. D. (2015). Towards quantitative, atomic-resolution reconstruction of the electrostatic potential via differential phase contrast using electrons. *Ultramicroscopy* **159**, 124–137.

Cochran, W., & Cowley, R. A. (1962). Dielectric constants and lattice vibrations. *Journal of Physics and Chemistry of Solids* **23**, 447–450.

Collins, S. M., Kepaptsoglou, D. M., Hou, J., Ashling, C. W., Radtke, G., Bennett, T. D., … Ramasse, Q. M. (2020). Functional Group Mapping by Electron Beam Vibrational Spectroscopy from Nanoscale Volumes. *Nano Letters* 1272–1279.

Colvard, C., Gant, T. A., Klein, M. V., Merlin, R., Fischer, R., Morkoc, H., & Gossard, A. C. (1985). Folded acoustic and quantized optic phonons in (GaAl)As superlattices. *Physical Review B* **31**, 2080–2091.

Crewe, A. V., Wall, J., & Langmore, J. (1970). Visibility of Single Atoms. *Science* **168**, 1338–1340.

Damodaran, A. R., Clarkson, J. D., Hong, Z., Liu, H., Yadav, A. K., Nelson, C. T., … Martin, L. W. (2017). Phase coexistence and electric-field control of toroidal order in oxide superlattices. *Nature Materials* **16**, 1003–1009.

Das, S., Tang, Y. L., Hong, Z., Gonçalves, M. A. P., McCarter, M. R., Klewe, C., … Ramesh, R. (2019). Observation of room-temperature polar skyrmions. *Nature* **568**, 368–372.

de Graaf, S., Momand, J., Mitterbauer, C., Lazar, S., & Kooi, B. J. (2020). Resolving hydrogen atoms at metal-metal hydride interfaces. *Science Advances* **6**, eaay4312.

de Groot, F. M. F., Faber, J., Michiels, J. J. M., Czyżyk, M. T., Abbate, M., & Fuggle, J. C. (1993). Oxygen 1 *s* x-ray absorption of tetravalent titanium oxides: A comparison with single-particle calculations. *Physical Review B* **48**, 2074–2080.

Dwyer, C., Aoki, T., Rez, P., Chang, S. L. Y., Lovejoy, T. C., & Krivanek, O. L. (2016). Electron-beam mapping of vibrational modes with nanometer spatial resolution. *Physical Review Letters* **117**, 256101–256105.

Egerton, R. F. (2011). *Electron Energy-Loss Spectroscopy in the Electron Microscope*. Retrieved from http://link.springer.com/10.1007/978-1-4419-9583-4

Egerton, R. F. (2014). Prospects for vibrational-mode EELS with high spatial resolution. *Microscopy and Microanalysis* **20**, 658–663.

Egoavil, R., Gauquelin, N., Martinez, G. T., Van Aert, S., Van Tendeloo, G., & Verbeeck, J. (2014). Atomic resolution mapping of phonon excitations in STEM-EELS experiments. *Ultramicroscopy* **147**, 1–7.

Fang, X. (2013). *Phase transitions in strontium titanate*. Retrieved from http://guava.physics.uiuc.edu/~nigel/courses/563/Essays_2013/PDF/fang.pdf

Forstmann, F., Gras-Marti, A., Ferrell, T. L., Warmack, R. J., & Mamola, K. C. (1991). Energy loss of low-energy electrons to nonabrupt metal surfaces. *Physical Review B* **44**, 4884.

Fultz, B., & Howe, J. (2013). *Transmission Electron Microscopy and Diffractometry of Materials*. Retrieved from http://link.springer.com/10.1007/978-3-642-29761-8

García de Abajo, F. J. (2010). Optical excitations in electron microscopy. *Reviews of Modern Physics* **82**, 209–275.

Garcia-Molina, R., Gras-Marti, A., Howie, A., & Ritchie, R. H. (1985). Retardation effects in the interaction of charged particle beams with bounded condensed media. *Journal of Physics C: Solid State Physics* **18**, 5335–5345.

Glazer, A. M. (1972). The classification of tilted octahedra in perovskites. *Acta Crystallographica Section B Structural Crystallography and Crystal Chemistry* **28**, 3384–3392.

Glazer, A. M. (1975). Simple ways of determining perovskite structures. *Acta Crystallographica Section A* **31**, 756–762.

Gleize, J., Renucci, M. A., Frandon, J., & Demangeot, F. (1999). Anisotropy effects on polar optical phonons in wurtzite GaN/AlN superlattices. *Physical Review B* **60**, 15985–15992.

Guyot, F., Richet, P., Courtial, Ph., & Gillet, Ph. (1993). High-temperature heat capacity and phase transitions of CaTiO3 perovskite. *Physics and Chemistry of Minerals* **20**. Retrieved from http://link.springer.com/10.1007/BF00200116

Hachtel, J. A., Huang, J., Popovs, I., Jansone-Popova, S., Keum, J. K., Jakowski, J., … Idrobo, J. C. (2019). Identification of site-specific isotopic labels by vibrational spectroscopy in the electron microscope. *Science* **363**, 525–528.

Haeni, J. H., Irvin, P., Chang, W., Uecker, R., Reiche, P., Li, Y. L., … Schlom, D. G. (2004). Room-temperature ferroelectricity in strained SrTiO3. *Nature* **430**, 758–761.

Hage, F. S., Radtke, G., Kepaptsoglou, D. M., Lazzeri, M., & Ramasse, Q. M. (2020). Single-atom vibrational spectroscopy in the scanning transmission electron microscope. *Science* **367**, 1124–1127.

Hage, Fredrik S., Nicholls, R. J., Yates, J. R., McCulloch, D. G., Lovejoy, T. C., Dellby, N., … Ramasse, Q. M. (2018). Nanoscale momentum-resolved vibrational spectroscopy. *Science Advances* **4**, 7495–7496.

Hage, F. S., Kepaptsoglou, D. M., Ramasse, Q. M., & Allen, L. J. (2019). Phonon Spectroscopy at Atomic Resolution. *Physical Review Letters* **122**, 016103–016105.

Haiber, D. M., & Crozier, P. A. (2018). Nanoscale Probing of Local Hydrogen Heterogeneity in Disordered Carbon Nitrides with Vibrational Electron Energy-Loss Spectroscopy. *ACS Nano* **12**, 5463–5472.

He, Q., Ishikawa, R., Lupini, A. R., Qiao, L., Moon, E. J., Ovchinnikov, O., … Borisevich, A. Y. (2015). Towards 3D Mapping of BO $_6$ Octahedron Rotations at Perovskite Heterointerfaces, Unit Cell by Unit Cell. *ACS Nano* **9**, 8412–8419.

Hessmer, R., Huber, A., Egeler, T., Haines, M., Tränkle, G., Weimann, G., & Abstreiter, G. (1992). Interface-phonon dispersion and confined-optical-mode selection rules of GaAs/AlAs superlattices studied by micro-Raman spectroscopy. *Physical Review B* **46**, 4071–4076.

Hong, Z., Damodaran, A. R., Xue, F., Hsu, S.-L., Britson, J., Yadav, A. K., … Chen, L.-Q. (2017). Stability of Polar Vortex Lattice in Ferroelectric Superlattices. *Nano Letters* **17**, 2246–2252.

Howard, C. J., & Stokes, H. T. (1998). Group-Theoretical Analysis of Octahedral Tilting in Perovskites. *Acta Crystallographica Section B Structural Science* **54**, 782–789.

Howard, C. J., Withers, R. L., & Kennedy, B. J. (2001). Space group and structure for the perovskite $Ca_{0.5}Sr_{0.5}TiO_3$. *Journal of Solid State Chemistry* **160**, 8–12.

Huang, F.-T., Gao, B., Kim, J.-W., Luo, X., Wang, Y., Chu, M.-W., … Cheong, S.-W. (2016). Topological defects at octahedral tilting plethora in bi-layered perovskites. *Npj Quantum Materials* **1**, 16017–6.

Idrobo, J. C., Konečná, A., Gazquez, J., Hachtel, J. A., Lovejoy, T. C., Dellby, N., … Krivanek, O. L. (2019). EELS in STEM: the “Swiss Army Knife” of Spectroscopy. *Microscopy and Microanalysis* **25**, 620–621.

Ishizuka, A., Oka, M., Seki, T., Shibata, N., & Ishizuka, K. (2017). Boundary-artifact-free determination of potential distribution from differential phase contrast signals. *Journal of Electron Microscopy* **66**, 397–405.

Itoh, M., Wang, R., Inaguma, Y., Yamaguchi, T., Shan, Y.-J., & Nakamura, T. (1999). Ferroelectricity Induced by Oxygen Isotope Exchange in Strontium Titanate Perovskite. *Physical Review Letters* **82**, 3540–3543.

Jokisaari, J. R., Hachtel, J. A., Hu, X., Mukherjee, A., Wang, C., Konecna, A., … Klie, R. F. (2018). Vibrational Spectroscopy of Water with High Spatial Resolution. *Advanced Materials* **30**, 1802702.

Jusserand, B., Paquet, D., & Regreny, A. (1984). “Folded” optical phonons in GaAs Ga $1 - x$ Al x As superlattices. *Physical Review B* **30**, 6245–6247.

Kamarás, K., Barth, K. -L., Keilmann, F., Henn, R., Reedyk, M., Thomsen, C., … Stehlé, J. -L. (1995). The low-temperature infrared optical functions of $SrTiO_3$ determined by reflectance spectroscopy and spectroscopic ellipsometry. *Journal of Applied Physics* **78**, 1235–1240.

Kennedy, B. J., Howard, C. J., & Chakoumakos, B. C. (1999). Phase transitions in perovskite at elevated temperatures - a powder neutron diffraction study. *Journal of Physics: Condensed Matter* **11**, 1479–1488.

Kim, J., Kim, Y., Kim, Y. S., Lee, J., Kim, L., & Jung, D. (2002). Large nonlinear dielectric properties of artificial $BaTiO_3/SrTiO_3$ superlattices. *Applied Physics Letters* **80**, 3581–3583.

King, G., & Woodward, P. M. (2010). Cation ordering in perovskites. *Journal of Materials Chemistry* **20**, 5785–12.

Kishida, K., Goto, K., & Inui, H. (2009). Electron diffraction of ABX_3 perovskites with both layered ordering of A cations and tilting of BX_6 octahedra. *Acta Crystallographica Section B Structural Science* **65**, 405–415.

Klie, R. F., Beleggia, M., Zhu, Y., Buban, J. P., & Browning, N. D. (2003). Atomic-scale model of the grain boundary potential in perovskite oxides. *Physical Review B* **68**, 214101–214110.

Klie, R. F., Walkosz, W., Yang, G., & Zhao, Y. (2009). Aberration-corrected Z-contrast imaging of $SrTiO_3$ dislocation cores. *Journal of Electron Microscopy* **58**, 185–191.

Kliewer, K. L., & Fuchs, R. (1966). Optical Modes of Vibration in an Ionic Crystal Slab Including Retardation. II. Radiative Region. *Physical Review* **150**, 573–588.

Kliewer, K. L., & Fuchs, R. (1967). Collective Electronic Motion in a Metallic Slab. *Physical Review* **153**, 498–512.

Knight, K. S. (2011). Structural and thermoelastic properties of CaTiO3 perovskite between 7K and 400K. *Journal of Alloys and Compounds* **509**, 6337–6345.

Konečná, A. (2019). *Theoretical description of low-energy excitations in nanostructures as probed by fast electrons*. CFM Auditorium.

Konečná, A., Venkatraman, K., March, K., Crozier, P. A., Hillenbrand, R., Rez, P., & Aizpurua, J. (2018). Vibrational electron energy loss spectroscopy in truncated dielectric slabs. *Physical Review B* **98**. Retrieved from https://link.aps.org/doi/10.1103/PhysRevB.98.205409

Koopmans, H. J. A., van de Velde, G. M. H., & Gellings, P. J. (1983). Powder neutron diffraction study of the perovskites $CaTiO_3$ and $CaZrO_3$. *Acta Crystallographica Section C Crystal Structure Communications* **39**, 1323–1325.

Kretschmann, E., & Raether, H. (1968). Notizen: Radiative Decay of Non Radiative Surface Plasmons Excited by Light. *Zeitschrift Für Naturforschung A* **23**, 2135–2136.

Krivanek, O. L., Lovejoy, T. C., Dellby, N., Aoki, T., Carpenter, R. W., Rez, P., … Crozier, P. A. (2014). Vibrational spectroscopy in the electron microscope. *Nature* **514**, 209–212.

Kröger, E. (1970). Transition radiation, Cerenkov radiation and energy losses of relativistic charged particles traversing thin foils at oblique incidence. *Zeitschrift Für Physik* **235**, 403–421.

Kurosawa, T. (1961). Polarization waves in solids. *Journal of the Physical Society of Japan* **16**, 1298–1308.

Lagos, M. J., & Batson, P. E. (2018). Nanoscale Temperature Measurements Using Phonon Scattering. *Microscopy and Microanalysis* **24**, 420–421.

Lagos, Maureen J., & Batson, P. E. (2018). Thermometry with Subnanometer Resolution in the Electron Microscope Using the Principle of Detailed Balancing. *Nano Letters* **18**, 4556–4563.

Lagos, Maureen J, Trügler, A., Amarasinghe, V., Feldman, L. C., Hohenester, U., & Batson, P. E. (2018). Excitation of long-wavelength surface optical vibrational modes in films, cubes and film/cube composite system using an atom-sized electron beam. *Microscopy* **67**, i3–i13.

Lagos, Maureen J., Trügler, A., Hohenester, U., & Batson, P. E. (2017). Mapping vibrational surface and bulk modes in a single nanocube. *Nature* **543**, 529–532.

Lazić, I., Bosch, E. G. T., & Lazar, S. (2016). Phase contrast STEM for thin samples: Integrated differential phase contrast. *Ultramicroscopy* **160**, 265–280.

Leapman, R. D., Grunes, L. A., & Fejes, P. L. (1982). Study of the L 23 edges in the 3 d transition metals and their oxides by electron-energy-loss spectroscopy with comparisons to theory. *Physical Review B* **26**, 614–635.

Lee, H. N., Christen, H. M., Chisholm, M. F., Rouleau, C. M., & Lowndes, D. H. (2005). Strong polarization enhancement in asymmetric three-component ferroelectric superlattices. *Nature* **433**, 395–399.

Leinenweber, K., & Parise, J. (1995). High-Pressure Synthesis and Crystal Structure of CaFeTi2O6, a New Perovskite Structure Type. *Journal of Solid State Chemistry* **114**, 277–281.

Li, Y., Qi, R., Shi, R., Li, N., & Gao, P. (2020). Manipulation of surface phonon polaritons in SiC nanorods. *Science Bulletin* **65**, 820–826.

Liao, K., Haruta, M., Masuno, A., Inoue, H., Kurata, H., & Mizoguchi, T. (2020). Real-Space Mapping of Oxygen Coordination in Phase-Separated Aluminosilicate Glass: Implication for Glass Stability. *ACS Applied Nano Materials* acsanm.0c00196.

Lu, L., Nahas, Y., Liu, M., Du, H., Jiang, Z., Ren, S., … Bellaiche, L. (2018). Topological Defects with Distinct Dipole Configurations in PbTiO 3 / SrTiO 3 Multilayer Films. *Physical Review Letters* **120**, 177601.

Marrec, F. L., Farhi, R., Marssi, M. E., Dellis, J. L., Karkut, M. G., & Ariosa, D. (n.d.). *Ferroelectric PbTiO$_3$/BaTiO$_3$ superlattices: Growth anomalies and confined modes*. 4.

Megaw, H. D. (1952). Origin of ferroelectricity in barium titanate and other perovskite-type crystals. *Acta Crystallographica* **5**, 739–749.

Middey, S., Meyers, D., Ojha, S. K., Kareev, M., Liu, X., Cao, Y., … Chakhalian, J. (2018). Epitaxial strain modulated electronic properties of interface controlled nickelate superlattices. *Physical Review B* **98**, 045115–045118.

Mishra, S. K., Ranjan, R., Pandey, D., & Stokes, H. T. (2006). Resolving the controversies about the 'nearly cubic' and other phases of $Sr_{1-x}Ca_xTiO_3$ ($0\leq x \leq 1$): I. Room temperature structures. *Journal of Physics: Condensed Matter* **18**, 1885–1898.

Moore, K. T., & Howe, J. M. (2000). Characterization of γ plate-shaped precipitates in an Al–4.2 at.% Ag alloy — growth kinetics, solute field, composition and modeling. *Acta Materialia* **48**, 4083–4098.

Moreau, P., Brun, N., Walsh, C. A., Colliex, C., & Howie, A. (1997). Relativistic effects in electron-energy-loss-spectroscopy observations of the Si/SiO_2 interface plasmon peak. *Physical Review B* **56**, 6774–6781.

Mulder, A. T., Benedek, N. A., Rondinelli, J. M., & Fennie, C. J. (2013). Turning ABO_3 Antiferroelectrics into Ferroelectrics: Design Rules for Practical Rotation-Driven Ferroelectricity in Double Perovskites and A_3B<sub>2</sub O_7 Ruddlesden-Popper Compounds. *Advanced Functional Materials* 4810–4820.

Müller, K. A., & Burkard, H. (1979). $SrTiO_3$: An intrinsic quantum paraelectric below 4 K. *Physical Review B* **19**, 3593–3602.

Müller, K. Alex, Berlinger, W., & Tosatti, E. (1991). Indication for a novel phase in the quantum paraelectric regime of $SrTiO_3$. *Zeitschrift Für Physik B Condensed Matter* **84**, 277–283.

Müller, K., Krause, F. F., Béché, A., Schowalter, M., Galioit, V., Löffler, S., … Rosenauer, A. (2014). Atomic electric fields revealed by a quantum mechanical approach to electron picodiffraction. *Nature Communications* **5**, 5653.

Nellist, P. D. (2019). Scanning Transmission Electron Microscopy. In P. W. Hawkes & J. C. H. Spence (Eds.), *Springer Handbook of Microscopy* (pp. 2–2). Retrieved from http://link.springer.com/10.1007/978-3-030-00069-1_2

Neyer, T., Schattschneider, P., Bolton, J. P. R., & Botton, G. A. (1997). Plasmon coupling and finite size effects in metallic multilayers. *Journal of Microscopy* **187**, 184–192.

Nguyen, K. X., Jiang, Y., Cao, M. C., Purohit, P., Yadav, A. K., Junquera, J., … Muller, D. A. (2018). Mapping Polarity, Toroidal Order, and the Local Energy Landscape by 4D-STEM. *Microscopy and Microanalysis* **24**, 176–177.

Nicholls, R. J., Hage, F. S., McCulloch, D. G., Ramasse, Q. M., Refson, K., & Yates, J. R. (2019). Theory of momentum-resolved phonon spectroscopy in the electron microscope. *Physical Review B* **99**, 094105–094107.

Nord, M., Ross, A., McGrouther, D., Barthel, J., Moreau, M., Hallsteinsen, I., … MacLaren, I. (2019). Three-dimensional subnanoscale imaging of unit cell doubling due to octahedral tilting and cation modulation in strained perovskite thin films. *Physical Review Materials* **3**, 063605–063607.

Nord, M., Vullum, P. E., Hallsteinsen, I., Tybell, T., & Holmestad, R. (2016). Assessing electron beam sensitivity for $SrTiO_3$ and $La_{0.7}Sr_{0.3}MnO_3$ using electron energy loss spectroscopy. *Ultramicroscopy* **169**, 98–106.

Nord, M., Vullum, P. E., MacLaren, I., Tybell, T., & Holmestad, R. (2017). Atomap: a new software tool for the automated analysis of atomic resolution images using two-dimensional Gaussian fitting. *Advanced Structural and Chemical Imaging* **3**, 9–12.

Nuzhnyy, D., Petzelt, J., Kamba, S., Martí, X., Čechal, T., Brooks, C. M., & Schlom, D. G. (2011). Infrared phonon spectroscopy of a compressively strained (001) $SrTiO_3$ film grown on a (110) $NdGaO_3$ substrate. *Journal of Physics: Condensed Matter* **23**, 045901–045909.

Ohta, T., Robinson, J. T., Feibelman, P. J., Bostwick, A., Rotenberg, E., & Beechem, T. E. (2012). Evidence for Interlayer Coupling and Moiré Periodic Potentials in Twisted Bilayer Graphene. *Physical Review Letters* **109**, 186807–6.

Ohtomo, A., Muller, D. A., Grazul, J. L., & Hwang, H. Y. (2002). Artificial charge-modulationin atomic-scale perovskite titanate superlattices. *Nature* **419**, 378–380.

Ophus, C. (2019). Four-Dimensional Scanning Transmission Electron Microscopy (4D-STEM): From Scanning Nanodiffraction to Ptychography and Beyond. *Microscopy and Microanalysis* **25**, 563–582.

Ostapchuk, T., Petzelt, J., Železný, V., Pashkin, A., Pokorný, J., Drbohlav, I., … Waser, R. (2002). Origin of soft-mode stiffening and reduced dielectric response in $SrTiO_3$ thin films. *Physical Review B* **66**, 235406–235412.

Park, J., Ahn, Y., Tilka, J. A., Lee, H. J., Pateras, A., Yusuf, M. H., … Evans, P. G. (2020). Role of temperature-dependent electron trapping dynamics in the optically driven nanodomain transformation in a $PbTiO_3/SrTiO_3$ superlattice. *Applied Physics Letters* **116**, 012901–012919.

Park, J. H., Woodward, P. M., & Parise, J. B. (1998). Predictive Modeling and High-Pressure−High-Temperature Synthesis of Perovskites Containing Monovalent Silver. *Chemistry of Materials* **10**, 3092–3100.

Parlinski, K., Kawazoe, Y., & Waseda, Y. (2001). *Ab initio* studies of phonons in $CaTiO_3$. *The Journal of Chemical Physics* **114**, 2395–2400.

Pauling, L. (1929). The principles determining the structure of complex ionic crystals. *Journal of the American Chemical Society* **51**, 1010–1026.

Pedregosa, F., Varoquaux, G., Gramfort, A., Michel, V., Thirion, B., Grisel, O., … Cournapeau, D. (n.d.). Scikit-learn: Machine learning in python. *MACHINE LEARNING IN PYTHON* 6.

Perry, C. H., Fertel, J. H., & McNelly, T. F. (1967). Temperature Dependence of the Raman Spectrum of $SrTiO_3$ and $KTaO_3$. *The Journal of Chemical Physics* **47**, 1619–1625.

Pitcher, M. J., Mandal, P., Dyer, M. S., Alaria, J., Borisov, P., Niu, H., … Rosseinsky, M. J. (n.d.). Tilt engineering of spontaneous polarization and magnetization above 300 K in a bulk layered perovskite. *Science* **347**, 420–424.

Qi, R., Wang, R., Li, Y., Sun, Y., Chen, S., Han, B., … Gao, P. (2019). Probing Far-Infrared Surface Phonon Polaritons in Semiconductor Nanostructures at Nanoscale. *Nano Letters* **19**, 5070–5076.

Radtke, G., Taverna, D., Menguy, N., Pandolfi, S., Courac, A., Le Godec, Y., … Lovejoy, T. C. (2019). Polarization Selectivity in Vibrational Electron-Energy-Loss Spectroscopy. *Physical Review Letters* **123**, 256001.

Raether, H. (1988). Surface plasmons. *Springer Tracts in Modern Physics* **111**, 1.

Ramesh, R., & Schlom, D. G. (2019). Creating emergent phenomena in oxide superlattices. *Nature Reviews Materials*. Retrieved from http://www.nature.com/articles/s41578-019-0095-2

Ranjan, R., & Pandey, D. (2001a). Antiferroelectric phase transition in $(Sr_{1-x}Ca_x)TiO_3$ $(0.12< \boldsymbol{x} \leqslant 0.40)$: I. Dielectric studies. *Journal of Physics: Condensed Matter* **13**, 4239–4249.

Ranjan, R., & Pandey, D. (2001b). Antiferroelectric phase transition in $(Sr_{1-x}Ca_x)TiO_3$: II. X-ray diffraction studies. *Journal of Physics: Condensed Matter* **13**, 4251–4266.

Ranjan, R., Pandey, D., Schuddinck, W., Richard, O., De Meulenaere, P., Van Landuyt, J., & Van Tendeloo, G. (2001). Evolution of Crystallographic Phases in $(Sr_{1-x}Ca_x)TiO_3$ with Composition (x). *Journal of Solid State Chemistry* **162**, 20–28.

Ranson, P., Ouillon, R., Pinan-Lucarre, J.-P., Pruzan, Ph., Mishra, S. K., Ranjan, R., & Pandey, D. (2005). The various phases of the system $(Sr_{1-x}Ca_x)TiO_3$—A Raman scattering study. *Journal of Raman Spectroscopy* **36**, 898–911.

Ravichandran, J., Yadav, A. K., Cheaito, R., Rossen, P. B., Soukiassian, A., Suresha, S. J., … Zurbuchen, M. A. (2014). Crossover from incoherent to coherent phonon scattering in epitaxial oxide superlattices. *Nature Materials* **13**, 168–172.

Redfern, S. A. T. (n.d.). *High-temperature structural phase transitions in perovskite (CaTiO3)*. 9.

Rez, P., Aoki, T., March, K., Gur, D., Krivanek, O. L., Dellby, N., … Cohen, H. (2016). Damage-free vibrational spectroscopy of biological materials in the electron microscope. *Nature Communications* **7**, 10945–10948.

Rez, P., & Muller, D. A. (2008). The Theory and Interpretation of Electron Energy Loss Near-Edge Fine Structure. *Annual Review of Materials Research* **38**, 535–558.

Rischau, C. W., Lin, X., Grams, C. P., Finck, D., Harms, S., Engelmayer, J., … Behnia, K. (2017). A ferroelectric quantum phase transition inside the superconducting dome of Sr1−xCaxTiO3−δ. *Nature Physics* **13**, 643–648.

Ritchie, R. H. (1957). Plasma Losses by Fast Electrons in Thin Films. *Physical Review* **106**, 874–881.

Robinson, J. T., Schmucker, S. W., Diaconescu, C. B., Long, J. P., Culbertson, J. C., Ohta, T., … Beechem, T. E. (2013). Electronic Hybridization of Large-Area Stacked Graphene Films. *ACS Nano* **7**, 637–644.

Rondinelli, J. M., & Fennie, C. J. (2012). Octahedral rotation-induced ferroelectricity in cation ordered perovskites. *Advanced Materials* **24**, 1961–1968.

Sakhya, A. P., Maibam, J., Saha, S., Chanda, S., Dutta, A., Sharma, B. I., … Sinha, T. P. (2015). Electronic structure and elastic properties of $ATiO_3$ (A = Ba, Sr, Ca) perovskites: A first principles study. *APPL PHYS* **53**, 8.

Salje, E. K. (2012). *Physical properties and thermodynamic behaviour of minerals* (Vol. 225). Springer Science & Business Media.

Senga, R., Suenaga, K., Barone, P., Morishita, S., Mauri, F., & Pichler, T. (2019). Position and momentum mapping of vibrations in graphene nanostructures. *Nature* **573**, 247–250.

Shao, R., Zheng, K., Chen, Y., Zhang, B., Deng, Q., Jiao, L., … Han, X. (2016). Direct observation of structural transitions in the phase change material Ge_2 Sb_2Te_5. *Journal of Materials Chemistry C* **4**, 9303–9309.

Shibata, N., Findlay, S. D., Kohno, Y., Sawada, H., Kondo, Y., & Ikuhara, Y. (2012). Differential phase-contrast microscopy at atomic resolution. *Nature Physics* **8**, 611–615.

Sievers, A. J., & Page, J. B. (1990). Generalized Lyddane-Sachs-Teller relation and disordered solids. *Physical Review B* **41**, 3455–3459.

Tabata, H., & Kawai, T. (1997). Dielectric properties of strained $(Sr,Ca)TiO_3/(Ba,Sr)TiO_3$ artificial lattices. *Applied Physics Letters* **70**, 321–323.

Tabata, H., Tanaka, H., & Kawai, T. (1994). Formation of artificial $BaTiO_3$ /$SrTiO_3$ superlattices using pulsed laser deposition and their dielectric properties. *Applied Physics Letters* **65**, 1970–1972.

Tang, Y. L., Zhu, Y. L., Hong, Z. J., Eliseev, E. A., Morozovska, A. N., Wang, Y. J., … Ma, X. L. (2017). 3D polarization texture of a symmetric 4-fold flux closure domain in strained ferroelectric $PbTiO_3$ films. *Journal of Materials Research* **32**, 957–967.

Tokura, Y. (2007). Multiferroics—toward strong coupling between magnetization and polarization in a solid. *Journal of Magnetism and Magnetic Materials* **310**, 1145–1150.

Tomita, K., Miyata, T., Olovsson, W., & Mizoguchi, T. (2017). Strong excitonic interactions in the oxygen K-edge of perovskite oxides. *Ultramicroscopy* **178**, 105–111.

Ueda, K., Yanagi, H., Noshiro, R., Mizoguchi, H., Omata, T., Ueda, N., … Kawazoe, H. (1998). Observation of Electronic Structure in Conduction Band of CaTiO3. *Journal of the Ceramic Society of Japan* **106**, 964–967.

Venkatraman, K., Levin, B. D. A., March, K., Rez, P., & Crozier, P. A. (2019). Vibrational spectroscopy at atomic resolution with electron impact scattering. *Nature Physics*. Retrieved from http://www.nature.com/articles/s41567-019-0675-5

Venkatraman, K., March, K., Rez, P., & Crozier, P. A. (2018a). Aloof-beam vibrational electron energy-loss spectroscopy of adsorbate/metal particle systems. *Microscopy and Microanalysis* **24**, 460–461.

Venkatraman, K., March, K., Rez, P., & Crozier, P. A. (2018b). Spatially resolved vibrational electron energy-loss spectroscopy across an abrupt SiO_2/Si interface. *Microscopy and Microanalysis* **24**, 414–415.

Venkatraman, K., Rez, P., March, K., & Crozier, P. A. (2018). The influence of surfaces and interfaces on high spatial resolution vibrational EELS from SiO_2. *Microscopy* **67**, i14–i23.

Vollmer, C., Leitner, J., Kepaptsoglou, D., Ramasse, Q. M., Busemann, H., & Hoppe, P. (2019). Isotopic compositions, nitrogen functional chemistry, and low-loss electron spectroscopy of complex organic aggregates at the nanometer scale in the carbonaceous chondrite Renazzo. *Meteoritics & Planetary Science* maps.13389.

Wang, R., & Itoh, M. (2001). Suppression of the quantum fluctuation in 18 O -enriched strontium titanate. *Physical Review B* **64**, 174104–174106.

Wang, Z. L. (1996). Valence electron excitations and plasmon oscillations in thin films, surfaces, interfaces and small particles. *Micron* **27**, 265–299.

Warusawithana, M. P., Colla, E. V., Eckstein, J. N., & Weissman, M. B. (2003). Artificial Dielectric Superlattices with Broken Inversion Symmetry. *Physical Review Letters* **90**, 036802.

Woodward, D I, Wise, P. L., Lee, W. E., & Reaney, I. M. (2006). Space group symmetry of $(Ca_xSr_{1-x})TiO_3$ determined using electron diffraction. *Journal of Physics: Condensed Matter* **18**, 2401–2408.

Woodward, David I., & Reaney, I. M. (2005). Electron diffraction of tilted perovskites. *Acta Crystallographica Section B Structural Science* **61**, 387–399.

Woodward, P. M. (1997a). Octahedral tilting in perovskites. I. Geometrical considerations. *Acta Crystallographica Section B Structural Science* **53**, 32–43.

Woodward, P. M. (1997b). Octahedral tilting in perovskites. II. Structure stabilizing forces. *Acta Crystallographica Section B Structural Science* **53**, 44–66.

Wu, Z., Langenhorst, F., Seifert, F., Paris, E., & Marcelli, A. (2001). Oxygen 1 *s* ELNES study of perovskites $(Ca,Sr,Ba)TiO_3$. *Journal of Synchrotron Radiation* **8**, 934–936.

Yadav, A. K., Nelson, C. T., Hsu, S. L., Hong, Z., Clarkson, J. D., Schlepütz, C. M., … Ramesh, R. (2016). Observation of polar vortices in oxide superlattices. *Nature* **530**, 198–201.

Yadav, Ajay K., Nguyen, K. X., Hong, Z., García-Fernández, P., Aguado-Puente, P., Nelson, C. T., … Salahuddin, S. (2019). Spatially resolved steady-state negative capacitance. *Nature* **565**, 468–471.

Yamamoto, A., Onoda, M., Takayama-Muromachi, E., Izumi, F., Ishigaki, T., & Asano, H. (1990). Rietveld analysis of the modulated structure in the superconducting oxide $Bi_2(Sr,Ca)_3Cu_2O_{8+x}$. *Physical Review B* **42**, 4228–4239.

Yamanaka, A., Kataoka, M., Inaba, Y., Inoue, K., Hehlen, B., & Courtens, E. (2000). Evidence for competing orderings in strontium titanate from hyper-Raman scattering spectroscopy. *Europhysics Letters (EPL)* **50**, 688–694.

Yan, X., Liu, C., Gadre, C. A., Wu, R., & Pan, X. (2019). Probing Thermal-induced Phonon Energy Shift of SiC in Nanoscale by *in situ* Vibrational Spectroscopy. *Microscopy and Microanalysis* **25**, 622–623.

Yankowitz, M., Xue, J., Cormode, D., Sanchez-Yamagishi, J. D., Watanabe, K., Taniguchi, T., … LeRoy, B. J. (2012). Emergence of superlattice Dirac points in graphene on hexagonal boron nitride. *Nature Physics* **8**, 382–386.

Young, J., & Rondinelli, J. M. (2013). Atomic Scale Design of Polar Perovskite Oxides without Second-Order Jahn–Teller Ions. *Chemistry of Materials* **25**, 4545–4550.

Yücelen, E., Lazić, I., & Bosch, E. G. T. (2018). Phase contrast scanning transmission electron microscopy imaging of light and heavy atoms at the limit of contrast and resolution. *Scientific Reports* **8**, 2676.

Železný, V., Cockayne, E., Petzelt, J., Limonov, M. F., Usvyat, D. E., Lemanov, V. V., & Volkov, A. A. (2002). Temperature dependence of infrared-active phonons in $CaTiO_3$: A combined spectroscopic and first-principles study. *Physical Review B* **66**, 224303.

Zubko, P., Gariglio, S., Gabay, M., Ghosez, P., & Triscone, J.-M. (2011). Interface Physics in Complex Oxide Heterostructures. *Annual Review of Condensed Matter Physics* **2**, 141–165.

S1 Experimental Methods

All TEM images and SADP were acquired using a FEI Titan operating at 300 kV. SADPs were acquired with a 10 μm selected-area aperture and a Gatan One-View™ camera operating in diffraction mode to optimize the dynamic range of the camera. Dark-field imaging was performed using a 10 μm objective aperture, with a semi-angle of 1.33 mrad (2.7 nm^{-1}). This acceptance angle was larger than the distance between fundamental Bragg reflections and ORs, so the gun tilts were set so that the imaged ½(110) OR was near the edge of the objective aperture, which was centered on the optic axis.

All HAADF and iDPC images using a Thermo Fisher Themis Z-STEM operating at 300 kV. HAADF and iDPC images were simultaneously acquired with a 30 mrad convergence angle, 200 pA probe current, 625 nm/px dwell time, and 145 mm camera length. The 145 mm camera length projected onto the HAADF detector with a 200 mrad outer radius and 40 mrad inner radius. The segmented ADF detector used for iDPC had a 38 mrad outer radius and 10 mrad inner radius.

Atomic columns were found in HRTEM, HAADF, and iDPC images using Atomap (Nord et al., 2017). The position of each atomic column was refined by first finding the center of mass then iteratively fitting 2D Gaussians until the change in peak position converged. In each refinement step the column was radially masked 15% of the first n.l.n. distance to reduce the influence from neighboring columns. Refinement steps were not performed when oxygen columns were manually located because the small distance between adjacent columns results in one manually chosen position fitting both peaks and the second position fitting a residual in an unpredictable location. Construction of n.l.n. lists, SVD, and K-Means clustering were executed using Scikit-learn (Pedregosa et al., n.d.).

Core-loss and vibrational EELS spectra were acquired at 100 keV using a Nion Hermes monochromated aberration-corrected dedicated STEM. The probe had a convergence angle of 32 mrad and the spectrometer entrance aperture collection angle was 25 mrad and the spectrometer dispersion was providing approximately a 3:2 acceptance of the probe. 0.2 meV/channel and 0.174 eV/channel dispersions were used for vibrational and core-loss EELS, respectively.

S2 K-Means

K-Means clustering is an unsupervised form of machine learning that does not require known or labeled outcomes. The purpose of K-means is to group data into *N* clusters that share similar features. The algorithm is initialized with *N* randomly position centroids, then it iteratively adjusts the centroids until they converge to positions best explaneing the data. The choice of *N* clusters is primary input parameter and is best chosen using a dendrogram, as seen in Figure S2.1 for the Ti-sublattice n.l.n.

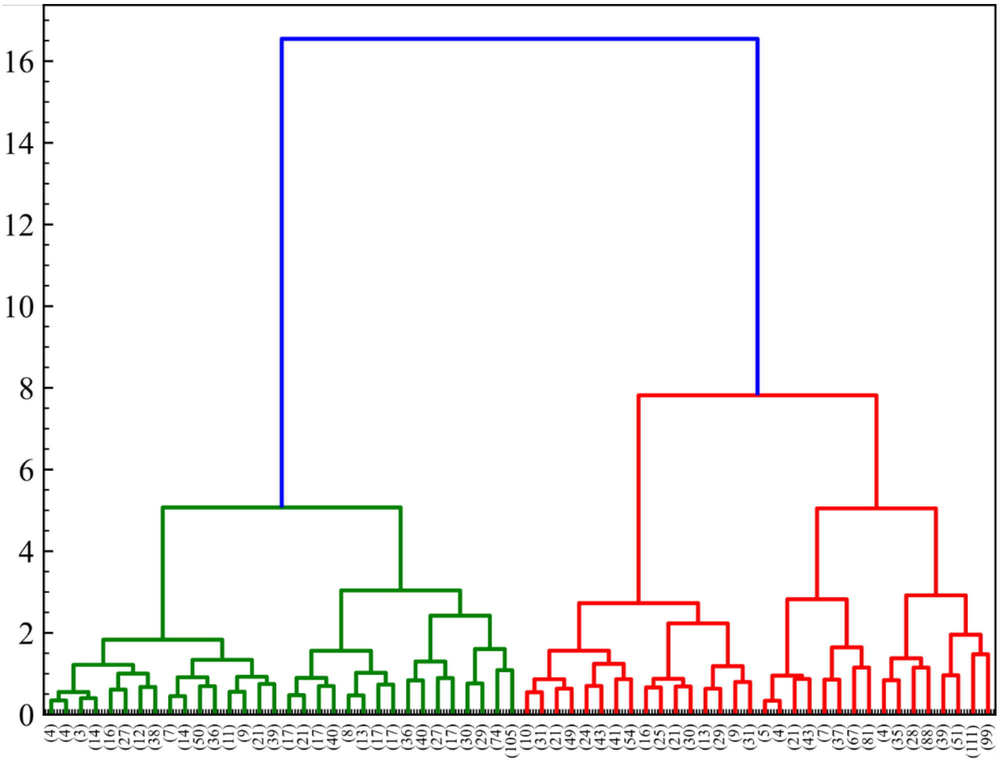

Figure S2.1. Dendrogram showing the relative contribution of adding additional clusters.

A dendrogram is a hierarchical plot that depicts the number of clusters explaneed by the vertical length of a branch. For example, in the above plot, if a horizontal line is drawn at y=12, it will intersect two branches (*N*=2), both of which explane large portions of the data. If y=6 is chosen instead, three clusters are identified. The first of these clusters explanes the same data as the first cluster with *N*=2, and the second and third clusters explane variations present in the second *N*=2 cluster. The second and third branches for *N*=3 have significant lengths and therefore, their clusters explane relevant information. Examples of two through four clusters are seen in Figure S2.2.

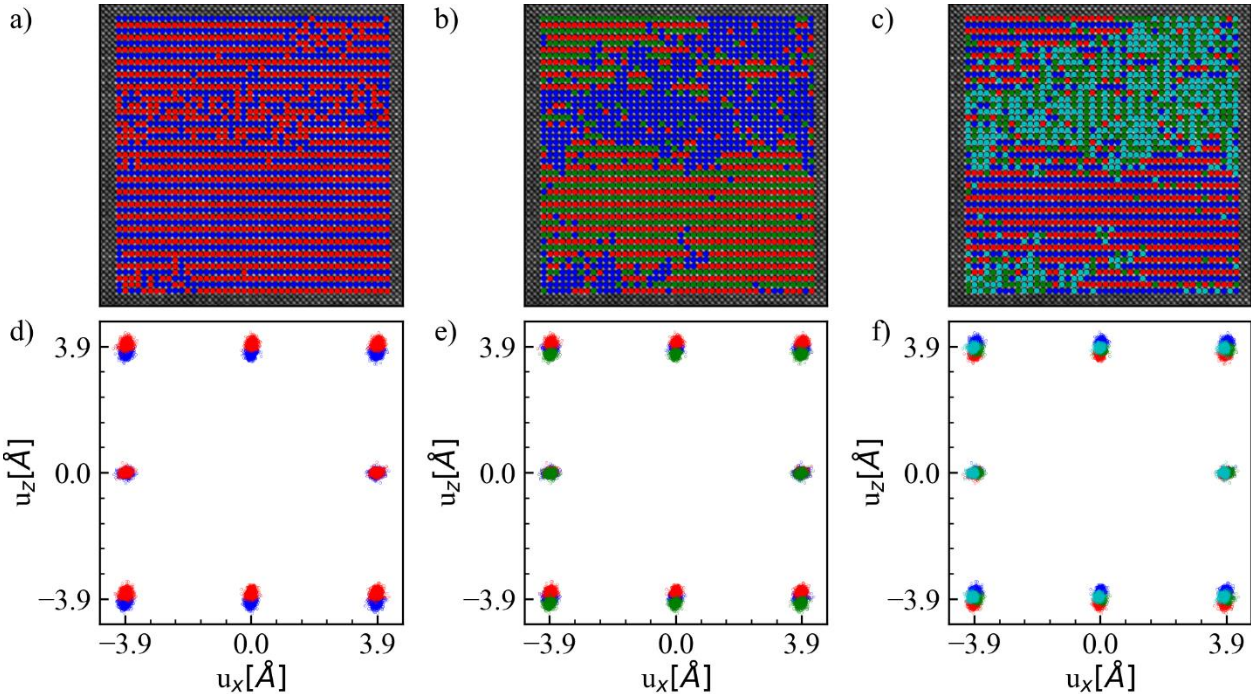

Figure S2.2. (a,d) two, (b,e) three, and (c,f) four cluster K-means showing the loss of information when two clusters are used rather than three, and the minimal gain of information when four clusters is used relative to three.

For *N*=2 clusters all n.l.n. are categorized as displaced, and although the regions with antiparallel displacements are clear, the regions with no displacement do not stand out as in *N*=3. Increasing from *N*=3 to 4 arguably adds information about $[010]_{pc}$ type displacements within the “non-displace” region of *N*=3. However, the significance of these additional displacements is minor compared to the other three clusters.

S3 Singular Value Decomposition

Singular value decomposition (SVD) is a multivariate statistical analysis technique used for dimensionality reduction. A matrix $\mathbf{A}_{mxn}$ is decamped into three matrices $\mathbf{U}_{mxm}$, $\mathbf{S}_{mxn}$, and $\mathbf{V}_{nxn}$ which represent a left eigenmatrix, a diagonal matrix containing the square root of eigenvalues (σ_i), and a right eigenmatrix, respectively, such that:

$$\mathbf{A}_{mxm} = \mathbf{U}_{\mathrm{mxm}}\mathbf{S}_{\mathrm{mxn}}\mathbf{V}_{\mathrm{nxn}}^{\mathrm{T}}$$

The left eigenmatrix is the solution of $\mathbf{AA}^{\mathrm{T}}$ and the right $\mathbf{A}^{\mathrm{T}}\mathbf{A}$. This is effectively an eigenmatrix problem that projects to new coordinate systems. **A** can be represented as the linear combination of components (c) such that:

$$\mathbf{A} = \sum_{c} \sigma_c U_c V_c$$

The value of σ_c decreases with increasing c and therefore the explanation of $\mathbf{A}$ increases with c. Thresholding the number of components therefore leads to dimensionality reduction and has a denoising characteristic. Additionally, in some situations each component can serve to categorize a set significant features within a data set. To choose the number of significant components the variance of each component is plotted relative to its index in what is known as a scree plot. Scree plots for SVD performed on the complex valued n.l.n. are shown in Figure S3.1.

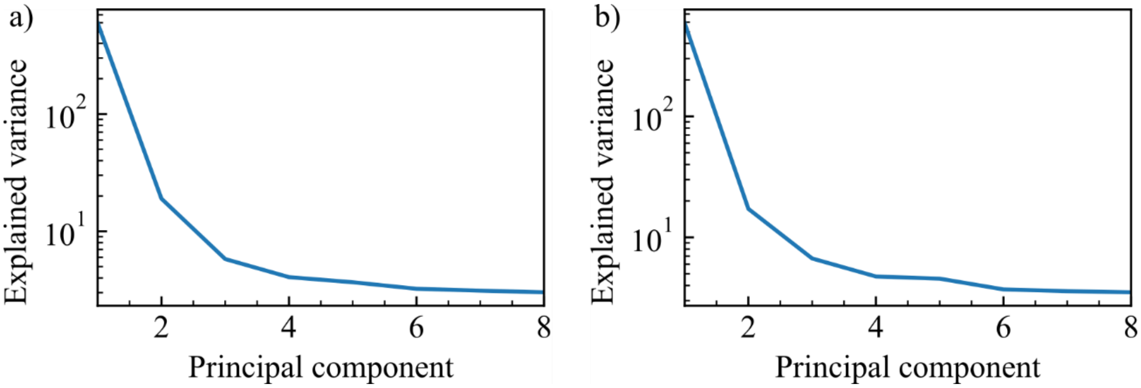

Figure S3.1. Explaneed variance of SVD performed on the Ti (a) and A-sublattice (b) n.l.n. distribution. The first two components explane the majority of the n.l.n. distribution.

When the log of the variance is plotted, the “elbow” or beginning of linearity is a conventional choice for the number of components to include. For both sublattices four components were chosen of which the first two explaneed most of the data. Figure S3.2 and Figure S3.3 show the first four components of the complex valued SVD for the Ti- and A-sublattice, respectively. The first two components of each are analyzed in the main text.

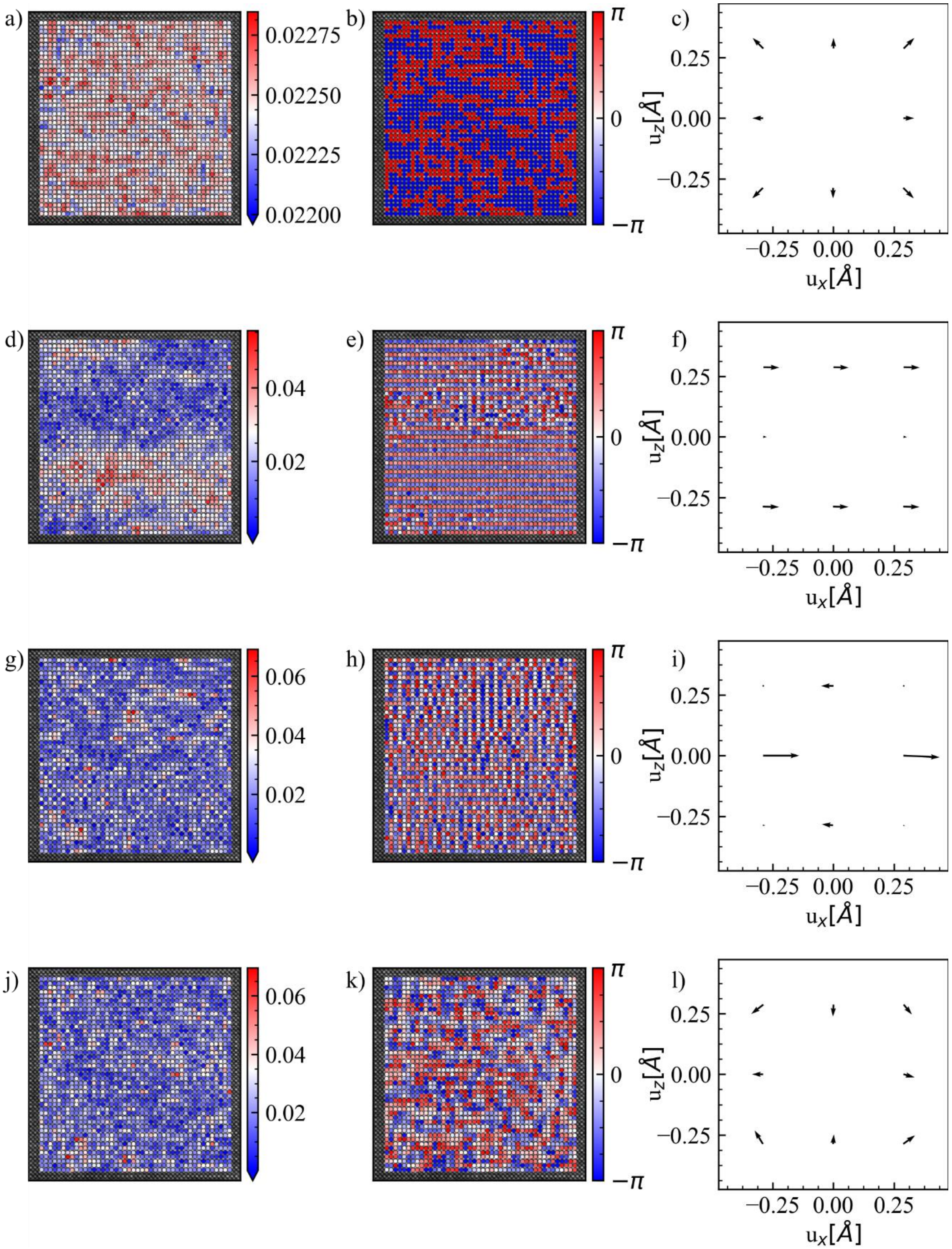

Figure S3.2. First four components of SVD performed on complex valued n.l.n. distribution in the Ti-sublattice. The (a,d,g,j) magnitude and (b,e,h,k) phase of the complex value loading along with (c,f,i,l) eigenvector displacements for component (a-c) 1, (d-f) 2, (g-i) 3, and (j-l) 4.

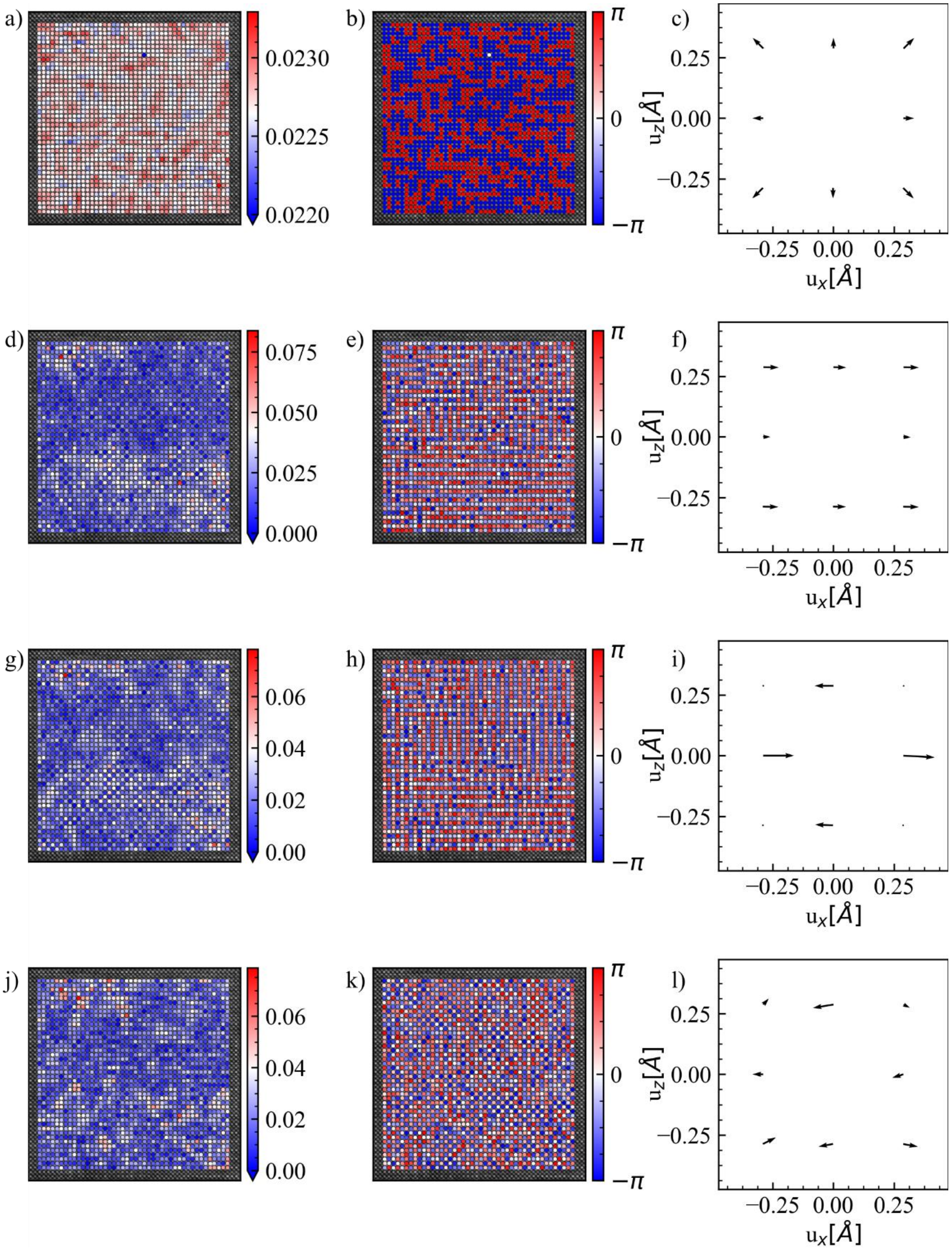

Figure S3.3. First four components of SVD performed on complex valued n.l.n. distribution in the A-sublattice. The (a,d,g,j) magnitude and (b,e,h,k) phase of the complex value loading along with (c,f,i,l) eigenvector displacements for component (a-c) 1, (d-f) 2, (g-i) 3, and (j-l) 4.

The phase of the SVD eigenvectors exhibited layers of alternating displacement patterns. The absolute value of cross-correlation with a checker, vertical, and horizontal pattern are shown in Figure S3.4.

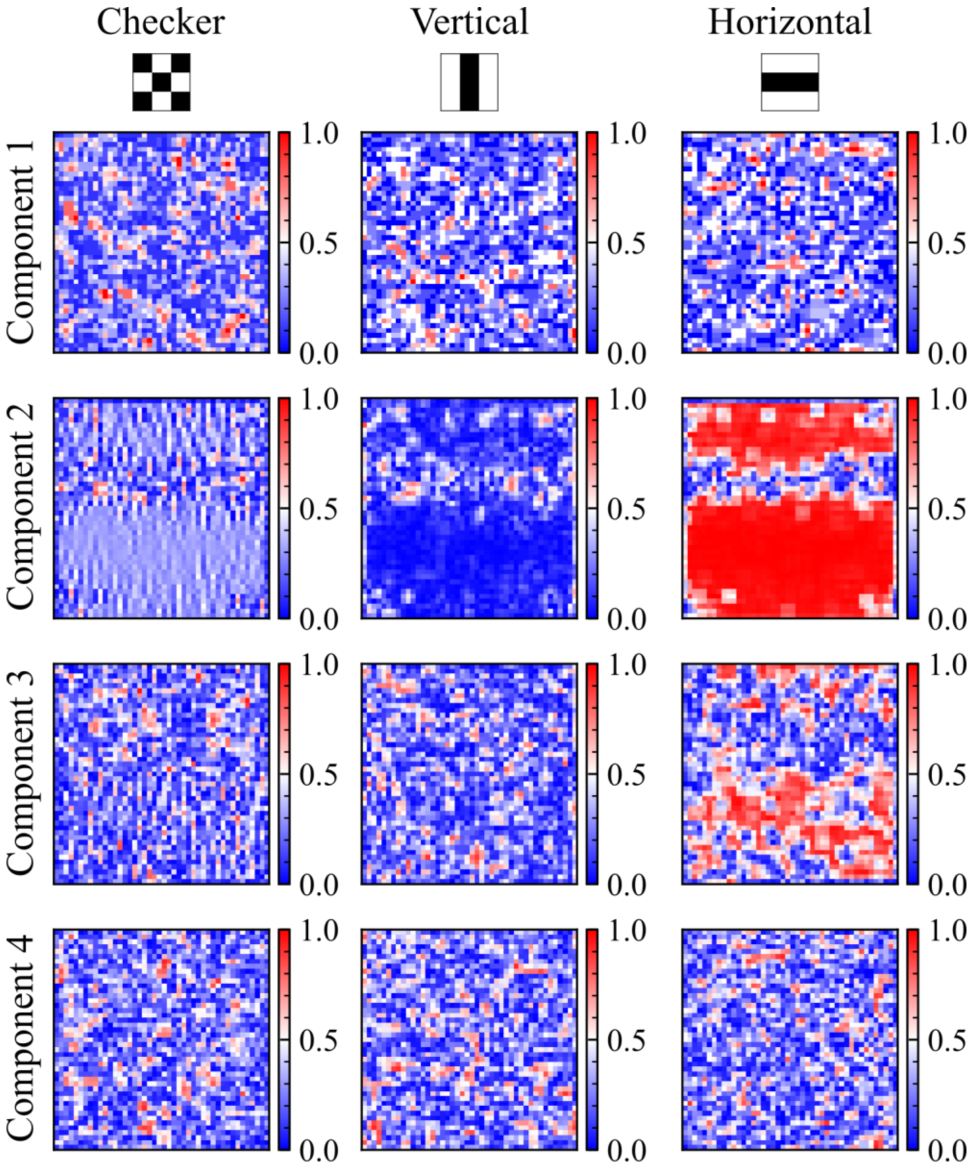

Figure S3.4. Cross-correlation of a checker, vertical, and horizontal pattern with the phase of the loading from SVD on the Ti-sublattice.

The absolute value was taken because a value of -1 and +1 both indicate that the same pattern exists, but is simply inverted relative to the template intensity, so if we are only interested in the pattern itself the sign of the cross-correlation is irrelevant. As a reminder, the phase of component 1 is meaningless, as discussed in the main text, but is included for completeness. Clear regions with horizontal layering are found in the components, like what were categorized with K-means. Additionally, vertically layered regions were found. High correlation with the checkerboard pattern resembles high correlation with the vertical pattern suggesting a possible nanometer-sized spinodal pattern.